

Magnetic and transport studies of the parent and Fe doped Hexagonal-Mn₃Ge Weyl semimetal

Venus Rai

Schlüsseltechnologien / Key Technologies

Band / Volume 268

ISBN 978-3-95806-695-3

Forschungszentrum Jülich GmbH
Jülich Centre for Neutron Science (JCNS)
Quantenmaterialien und kollektive Phänomene (JCNS-2/PGI-4)

Magnetic and transport studies of the parent and Fe doped Hexagonal-Mn₃Ge Weyl semimetal

Venus Rai

Schriften des Forschungszentrums Jülich
Reihe Schlüsseltechnologien / Key Technologies

Band / Volume 268

ISSN 1866-1807

ISBN 978-3-95806-695-3

Bibliografische Information der Deutschen Nationalbibliothek.
Die Deutsche Nationalbibliothek verzeichnet diese Publikation in der
Deutschen Nationalbibliografie; detaillierte Bibliografische Daten
sind im Internet über <http://dnb.d-nb.de> abrufbar.

Herausgeber
und Vertrieb: Forschungszentrum Jülich GmbH
 Zentralbibliothek, Verlag
 52425 Jülich
 Tel.: +49 2461 61-5368
 Fax: +49 2461 61-6103
 zb-publikation@fz-juelich.de
 www.fz-juelich.de/zb

Umschlaggestaltung: Grafische Medien, Forschungszentrum Jülich GmbH

Druck: Grafische Medien, Forschungszentrum Jülich GmbH

Copyright: Forschungszentrum Jülich 2023

Schriften des Forschungszentrums Jülich
Reihe Schlüsseltechnologien / Key Technologies, Band / Volume 268

D 82 (Diss. RWTH Aachen University, 2023)

ISSN 1866-1807
ISBN: 978-3-95806-695-3

The complete volume is freely available on the Internet on the Jülicher Open Access (JuSER) at
www.fz-juelich.de/zb/openaccess.



This is an Open Access publication distributed under the terms of the [Creative Commons Attribution License 4.0](https://creativecommons.org/licenses/by/4.0/),
which permits unrestricted use, distribution, and reproduction in any medium, provided the original work is properly cited.

Zusammenfassung

Weyl-Halbmatalle stellen vielversprechende Kandidaten für effiziente spintronische Geräte dar, und stehen aufgrund ihrer exotischen elektrischen und thermischen Transporteigenschaften im Fokus heutiger wissenschaftlicher Studien. Besonderes Augenmerk liegt aktuell auf dem Halbmetall Mn_3Ge , welches anomale Transporteffekte und Weyl-Punkte nahe der Fermi-Oberfläche zeigt.

Die magnetischen Momente des Mn in Mn_3Ge besitzen unterhalb der Néel Temperatur im Bereich von 365 K – 2 K eine planare dreieckige magnetische Struktur, mit einer geringen Neigung hin zur leichten Achse innerhalb der a - b Ebene. Die sich ergebenden kleinen ($\sim 20 \text{ m}\mu_{\text{B}}/\text{f.u.}$) ferromagnetischen (FM) Momente innerhalb der a - b Ebene resultieren in einer leichten Drehung des Mn-Spin-Dreiecks. Es bildet sich eine kleine Hysterese in den Magnetisierungs-, Nernst- und Hall-Effekt-Messungen wenn das Feld umgekehrt wird, was auf einen sehr geringen Wärmeverlust während der Umkehrung des Magnetfeldes hindeutet. Diese Eigenschaften machen Mn_3Ge zu einem hervorragenden Kandidaten für Schaltgeräte und andere spintronische Geräte. Zudem besitzt Mn_3Ge zwei weitere wichtige Eigenschaften: (i) Die Position der Weyl-Punkte und dessen resultierende Berry-Krümmung führt zu einem intrinsischen Magnetfeld von Hunderten von Tesla. (ii) Der anomale Hall-Effekt (AHE) wird im gesamten Temperaturbereich der nicht-kollinearen antiferromagnetischen Struktur (365 K - 2 K) beobachtet, wodurch sich Mn_3Ge gut für Raumtemperatur-, als auch für Niedertemperaturanwendungen eignet. Zusammengefasst sind diese Eigenschaften ideal, um in Mn_3Ge die Dynamik von Weyl-Punkten in Abhängigkeit von Temperaturveränderungen zu untersuchen.

Die Stärke der exotischen Transporteffekte wird durch die Lage der Weyl-Punkte relativ zur Fermi-Energie und dem Abstand der Weyl-Punkte zueinander bestimmt. In dieser Dissertation wird eine detaillierte Analyse der Transport- und der magnetischen Eigenschaften in Abhängigkeit verschiedener Parameter durchgeführt und die Auswirkung auf die Position der Weyl-Punkte untersucht.

Diese Arbeit ist in zwei Abschnitte eingeteilt: Erstens wurde eine detaillierte Untersuchung der Transporteigenschaften von Mn_3Ge unternommen, in Abhängigkeit der Magnetfeldorientierung entlang verschiedener kristallographischer Achsen. Zweitens wurden die magnetischen und die Transporteigenschaften des mit Fe dotierten Mn_3Ge analysiert. Im Folgenden werden beide Studien im Detail beschrieben und dessen Ergebnisse vorgestellt:

Im Rahmen der ersten Studie wurden Magnettransportstudien durchgeführt, um nach dem Vorhandensein der chiralen Anomalie zu suchen. Wir haben die positive longitudinale Magnetleitfähigkeit (LMC) und den planaren Hall-Effekt insbesondere in den Fällen analysiert, in denen das Feld in der a - b Ebene angelegt wurde. Die temperatur- und magnetfeldabhängigen Transportstudien haben gezeigt, dass die positive LMC unter 1,5 T höchstwahrscheinlich durch den Effekt der chiralen Anomalie induziert wird. Die Stärke der chiralen Anomalie nimmt mit der Temperatur ab und verschwindet fast nahezu bei Raumtemperatur. Im Gegensatz zur chiralen Anomalie bleibt der signifikant große AHE auch weit über Raumtemperatur hinaus bestehen. Daraus kann geschlossen werden, dass die Lage der Weyl-Punkte relativ zur Fermi-Oberfläche mit der Änderung der Temperatur der Probe variiert. Darüber hinaus zeigt die Entwicklung des Hall-Koeffizienten mit der Temperatur eine Änderung des dominanten Ladungsträgerkonzentrationstyps nahe 190 K. Eine Änderung in der Natur des Hochfeld-Magnetwiderstandsverhaltens wird auch nahe 200 K beobachtet, wo mit Hilfe von Widerstandsmessungen ein Metall-zu-Halbm Metall-Übergang beobachtet wurde. Diese Merkmale deuten auf einen topologischen elektronischen Phasenübergang in Mn_3Ge nahe 200 K hin, der möglicherweise durch den Metall-zu-Halbm Metall-Übergang der Probe bei 200 K angetrieben wird.

Zweitens sind Weyl-Punkte aufgrund ihrer topologischen Natur sehr robust. In dieser Arbeit werden die magnetischen und die Transporteigenschaften des mit Fe dotierten Mn_3Ge untersucht, um die Entwicklung der Weyl-Punkte in Bezug auf die Verunreinigung und die Änderung der magnetischen Eigenschaften der Verbindung zu bestimmen. Da zudem die magnetische Symmetrie des Kristallgitters eine fundamentale Rolle für die Existenz der Weyl-Punkte spielt, wurden Einkristall - Neutronenbeugungsmessungen an der mit 22% Fe dotierten Mn_3Ge -Probe durchgeführt. Unsere Neutronenbeugungsdatenanalyse in Kombination mit der Magnetisierung der verschiedenen Fe-dotierten Verbindungen hat ergeben, dass die Magnetstruktur des Typs Mn_3Ge bis zu einer Fe Dotierung von 26% bestehen bleibt. Interessanterweise werden der AHE und Signaturen des durch die chirale Anomalie induzierten Effekts auch in den Fe-dotierten Proben beobachtet, jedoch nur innerhalb des Temperaturbereichs, in dem die Probe eine Magnetstruktur des Typs Mn_3Ge besitzt. Dies bedeutet, dass die Weyl-Punkte in den Fe-dotierten Verbindungen existieren, solange die magnetische Struktur der dotierten Verbindungen die gleiche bleibt wie die der Stammverbindung. Im Fall einer mit 22% Fe dotierten Verbindung verschwindet der AHE in einem Temperaturbereich, in dem die magnetische Struktur kollinear anti-

ferromagnetisch ist. Dies impliziert, dass die Existenz der Weyl-Punkte eng mit der magnetischen Symmetrie der Verbindung verknüpft ist. Wir haben beobachtet, dass die Größe des AHE signifikant mit der Fe-Dotierung abnimmt. Die positive longitudinale Magnetleitfähigkeit (die Signatur des chiralen Anomalieeffekts) nimmt ebenfalls drastisch mit einer Zunahme der Fe-Dotierung ab. Daraus kann geschlossen werden, dass sich die Lage der Weyl-Punkte mit zunehmender Fe-Dotierung weiter von der Fermi-Oberfläche entfernt. Die Schwächung des AHE bei Fe-Dotierung legt ebenfalls nahe, dass der Abstand zwischen den Paaren der Weyl-Punkte mit zunehmender Fe-Dotierung abnimmt.

Abstract

The discovery of Weyl semimetals has shed light on the promising opportunity for the scientific community to develop very efficient spintronic devices. Weyl semimetals are widely studied because of their exotic electrical and thermal transport properties. Among different Weyl semimetals, Mn_3Ge has gained a lot of attention in recent years because of large anomalous transport effects owing to the presence of Weyl points near the Fermi surface.

In the case of Mn_3Ge , Mn moments possess an in-plane triangular magnetic structure below the Néel temperature of 365 K, down to the lowest measured temperature (2 K). The Mn moments possess slight canting towards the easy axis within the a - b plane, giving rise to small ($\sim 20 \text{ m}\mu_{\text{B}}/\text{f.u.}$) ferromagnetic (FM) moments within the a - b plane. Small FM moment helps in the easy rotation of the Mn spin triangle, leading to a very small hysteresis in the magnetization, Nernst, and Hall effect measurements when the field is reversed. This suggests very small heat loss while reversing the magnetic field direction, which makes it an excellent candidate for switching devices, and other spintronic devices. Also, the location of Weyl points in Mn_3Ge is such that the intrinsic magnetic field originated due to Berry curvature can be equivalent to the hundreds of Tesla. The anomalous Hall effect (AHE) is observed in the entire temperature regime where non-collinear antiferromagnetic structure persists (365 K - 2 K), which makes it a good candidate for room temperature and low-temperature applications. The existence of Weyl points in a large temperature regime makes Mn_3Ge an ideal candidate to study the dynamics of Weyl points relative to the change in temperature.

The strength of the exotic transport effects is determined by the location of Weyl points relative to the Fermi energy, and the separation of the Weyl points. Therefore, in this thesis, a detailed analysis of the transport and magnetic studies has been performed, under various conditions, to determine how the Weyl points evolve with the change in the various parameters.

This work is performed mainly in two parts: First, the magneto-transport properties of Mn_3Ge , with magnetic field applied along the different crystallographic axes, are studied in detail. Further, the magnetic and transport properties of the Fe doped Mn_3Ge compounds are analyzed. Both the studies are summarized below.

Initially, we performed a detailed study of the transport properties of Mn_3Ge with the magnetic field applied along several crystallographic axes. Magneto-transport

studies were performed to look for the presence of the chiral anomaly. We have observed the positive longitudinal magneto-conductivity (LMC), and planar Hall effect, particularly, in the cases when the field was applied in the a - b plane. The temperature and magnetic field dependent transport studies have shown that the positive LMC, below 1.5 T, is most likely induced by the chiral anomaly effect. The strength of the chiral anomaly decreases with temperature and almost vanishes near room temperature. Similar to the chiral anomaly, AHE also decreases significantly up to the room temperature. This suggests that the location of the Weyl points, relative to the Fermi surface, varies with the change in the temperature of the sample. Furthermore, the evolution of the Hall coefficient with temperature shows a change in the dominant carrier concentration type near 190 K. Change in the nature of high field magneto-resistance behavior is also observed near 200 K, where metal to semimetal transition is observed in the resistivity measurement. These observations suggest a topological electronic phase transition in Mn_3Ge , near 200 K, possibly driven by the metal to semimetal transition of the sample near this temperature.

Weyl points are supposed to be robust in nature because of the 3D topological protection. Therefore, we have studied the magnetic and transport properties of the Fe doped Mn_3Ge to determine the evolution of the Weyl points with respect to the impurity and change in the magnetic characteristics of the compound. Furthermore, since the magnetic symmetry of the crystal lattice plays a fundamental role in the existence of the Weyl points, single crystal neutron diffraction measurements of the 22% Fe doped Mn_3Ge sample were performed to determine the magnetic structure. Our neutron diffraction data analysis, in combination with the magnetization of the several Fe doped compounds, has revealed that the Mn_3Ge type magnetic structure persists up to the 26% Fe doped Mn_3Ge compounds. Interestingly, AHE and signatures of the chiral anomaly induced effect are also observed in the Fe doped samples, however, only within the temperature regime where the sample possesses Mn_3Ge type magnetic structure. This signifies that the Weyl points are very likely to exist in the Fe doped compounds, as long as the magnetic structure of the doped compounds remains the same as the parent compound. In the case of 22% Fe doped compound, the AHE vanishes in a temperature regime where the magnetic structure is collinear antiferromagnetic. This implies that the existence of the Weyl points is intimately linked with the magnetic symmetry of the compound. We observed that the magnitude of the AHE decreases significantly with Fe doping. The positive longitudinal magneto-conductance, which is the signature of the chiral anomaly effect, also de-

creases drastically as Fe doping increases. Therefore, it can be concluded that the location of Weyl points moves farther from the Fermi surface as Fe doping increases. The weakening of the AHE with Fe doping also suggests that the separation between the pairs of the Weyl points decreases with an increase in Fe doping.

Acknowledgements

It is an immense pleasure for me to sincerely thank my supervisor **Dr. Shibabrata Nandi** for his utmost support from the beginning of my research carrier at IIT Kanpur, India, till the end of my Ph.D. at Jülich Center for Neutron Science - II. This work would not have been possible without his support and guidance.

I express my gratitude to **Prof. Dr. Thomas Brückel**, for providing me the opportunity to pursue Ph.D. at Jülich Center for Neutron Science - II. I am very thankful to him for his valuable suggestions related to my thesis work. I am also thankful to **Prof. Dr. Georg Roth** for reviewing my Ph.D. thesis work.

I would like to thank **Jörg Perßon** for his co-operation during the synthesis of the compounds, which were used for the various experiments mentioned in this thesis. His efforts were fundamental for the successful growth of the samples.

I would like to thank **Berthold Schmitz** for his cooperation during the measurements and quick response for fixing the instruments, whenever it was required.

I am very much thankful to **Dr. Anne Stunault** and **Dr. Wolfgang Schmidt** from ILL, France for successfully performing my neutron diffraction experiments, in my absence, during the hard times of the COVID-19 pandemic in 2021. My work would not have progressed further without their support. I would also like to thank **Dr. Tobias Förster** from HZDR Dresden for performing a part of the high field experiments, in my absence, during the COVID-19 pandemic time.

I would like to thank **Dr. Martin Meven** and **Dr. Rajesh Dutta** for their support during our beamtime at FRM-II, Garching. The discussions regarding the experiment and data analysis were very helpful during my entire thesis work.

I would like to thank my colleagues **Nileena Nandakumaran**, **Dr. Mohammed Ait Haddouch**, **Subhadip Jana**, and **Dr. Annika Stelhorn** for their support, especially during the first few months of my entry to Germany. I would also like to thank them for the discussions and support regarding my thesis work.

I would like to thank **Micha Hölzle** for his technical support whenever required.

I would like to thank **Mrs. Barbara Daegener**, for her active support during my

entire stay at the JCNS-2.

I would like to thank **Andrear Eich**, **Henrik Thoma**, and **Prof. Dr. Karen Friese** for their support and suggestions regarding the various diffraction analysis.

I am very thankful to **Sneha**, **Anmol**, **Sheetal**, **Archit** and other friends for their all time support and discussions over various topics, which were helpful for my thesis work.

Last but foremost, I express my gratitude to thank my mother and father, for their belief in me, and for keeping me motivated all the time. They have been my constant support since the beginning of my life. I would not have achieved this day without their support. I would also like to express my special thank to my brothers, sisters, and family members, who kept me smiling for nearly three decades.

Contents

1	Introduction and motivation	2
2	Scientific background	5
2.1	Topology	6
2.2	Topological materials	7
2.2.1	Topological insulators	7
2.2.2	Nodal line semimetal	8
2.2.3	Dirac semimetal	9
2.2.4	Weyl semimetals	10
2.2.4.1	Topological protection in 3D	11
2.2.4.2	Location of the Weyl points	12
2.3	Surface states in topological materials	14
2.4	Berry phase and Berry curvature	16
2.5	Anomalous transport properties	20
2.5.1	Anomalous Hall effect	20
2.5.1.1	Extrinsic contribution	20
2.5.1.2	Intrinsic contribution	21
2.5.2	Chiral anomaly	22
2.5.2.1	Longitudinal magneto-resistance	22
2.5.2.2	Planar Hall effect	26
2.6	Magnetic Weyl semimetals - Mn_3X ($X = \text{Sn}, \text{Ge}$)	26
2.7	Scattering	28
2.7.1	Scattering cross section	28
2.7.2	Basics of diffraction	30
2.7.3	Diffraction in periodic lattice	32
2.7.3.1	Bragg's law, Ewald sphere, and Laue condition	32
2.7.3.2	Diffraction from (non - magnetic) crystal	34
2.7.4	X-ray scattering	34

2.7.5	Neutron scattering	35
2.7.5.1	Nuclear scattering	36
2.7.5.2	Magnetic scattering	38
2.7.5.3	Polarized neutron scattering	40
3	Experimental methods, instruments, and theory	42
3.1	Synthesis of single crystal	43
3.1.1	Induction melting	43
3.1.2	Single crystal growth technique	44
3.2	Inductively coupled plasma - optical emission spectrometry (ICP-OES) method	46
3.3	X-ray diffraction methods	47
3.3.1	X-ray powder diffraction	47
3.3.2	Laue diffraction	48
3.3.3	Single crystal X-ray diffraction (Supernova)	50
3.4	Physical properties measurement system (PPMS)	51
3.4.1	Magnetization (VSM)	51
3.4.2	Electrical transport measurements	52
3.5	High magnetic field measurements at HZDR Dresden	53
3.6	Single crystal neutron scattering facilities	57
3.6.1	HEiDi (FRM-II, Garching, Germany) and D23 (ILL, Grenoble, France)	57
3.6.2	Spherical neutron polarimetry using CRYOPAD (D3), ILL, France	58
4	Synthesis and characterization of Hexagonal - $[\text{Mn}_{(1-\alpha)}\text{Fe}_\alpha]_{3+\delta}\text{Ge}$	61
4.1	Sample preparation	62
4.2	Sample characterization	62
4.2.1	Chemical analysis	62
4.2.2	X-ray powder diffraction	64
4.2.3	Laue diffraction and SC X-ray diffraction	65
5	Magneto-resistance, and electronic transition in Mn_3Ge Weyl semimetal	69
5.1	Introduction	70
5.2	Experimental details	71
5.3	Magnetization	71

5.4	Electrical transport measurements	73
5.4.1	Longitudinal magneto-resistance	73
5.4.1.1	LMR along the x or y axis	76
5.4.1.2	LMC along the z axis	80
5.4.2	Angular magneto-resistance	81
5.4.3	Analysis of high field θ MR	85
5.4.4	Anomalous Hall effect	85
5.4.5	Planar Hall effect	91
5.5	Single crystal neutron diffraction	91
5.6	Conclusion	96
6	Magnetic structure of $(\text{Mn}_{0.78}\text{Fe}_{0.22})_{3.2}\text{Ge}$ using Neutron diffraction measurements	97
6.1	Introduction	98
6.2	Experimental details	99
6.2.1	Magnetization	100
6.3	Electrical transport measurements	104
6.4	Neutron diffraction	106
6.4.1	Unpolarized neutron diffraction (D23)	107
6.4.2	Polarized neutron diffraction (CRYOPAD)	112
6.5	Conclusion	115
7	Magnetic and transport properties of $(\text{Mn}_{(1-\alpha)}\text{Fe}_{\alpha})_{3.2}\text{Ge}$	117
7.1	Introduction	118
7.2	Experimental methods	119
7.3	Magnetization	120
7.4	Electrical Transport Results	123
7.4.1	Anomalous Hall effect	125
7.4.2	Chiral anomaly	129
7.4.2.1	Longitudinal magneto-conductivity	130
7.4.2.2	Angular magneto-conductivity	134
7.4.2.3	Planar Hall effect	136
7.5	Conclusion	139
8	Summary and outlook	140
8.1	Summary	141

8.2 Outlook	142
Bibliography	145

List of Figures

- 2.1 (Ref. [3, 4]) Möbius strips, made by joining them end to end, after twisting them one and two times are shown in (a) and (b), respectively. The red line illustrates a particular surface of the strip. (c-e) Different types of topologically inequivalent knots. 6
- 2.2 (Ref. [8, 9]) The overlap of conduction and valence bands inverts the electronic band, which is shown in (a). Weak or absent the spin orbit coupling (SOC) gives nodal line semimetal shown in (a). Strong SOC may lead to topological insulator (TI), Weyl semimetal, or Dirac semimetal, which are shown in (c, d). (d) shows the gapless surface state which is present in TIs. The orange circle and spins in (e, f) show spin-momentum locked surface state corresponding to the TI, and Weyl semimetal, respectively. (g) shows the splitting of the Dirac point, induced by the broken symmetry, into a pair of Weyl points shows. (h) shows Weyl semimetal of type-I. (i) Weyl semimetal of type-II, where Weyl cones are tilted towards the x axis. This modifies Weyl Hamiltonian as: $H_\chi = \hbar v_F(\chi \mathbf{k} \cdot \boldsymbol{\sigma} + \gamma_t k_x)$, where γ_t is the tilt parameter [9]. $|\gamma_t| < 1$ ($|\gamma_t| > 1$) leads to the type-I (type-II) Weyl nodes. In the case of type-II Weyl nodes, the Fermi energy crosses the lower and upper band as well, giving rise to the electron and hole pockets. 8
- 2.3 (Ref. [21]) Evolution of the band structure from normal insulator to topological insulator, determined by the strength SOC, which can be achieved by the doping of the sample [22]. The symbols ‘+’ and ‘-’ denote odd and even parity of the bands near the point where time-reversal symmetry is invariant. 9
- 2.4 (Ref. [26]) The band structure corresponding to the Hamiltonian mentioned in Eqn. (2.13). 12

- 2.5 (Ref. [28]) (a) Various surface state corresponding to the mentioned topological materials formed by a tuning the parameter m . (b) Calculated Fermi arc surface state of TaAs. (c) Path of the electron when the magnetic field is applied to a Weyl semimetal, along the z axis. Straight arrows show the path of the electron in real space. Filled and open dots show Weyl points of opposite chirality. Red and blue arcs on the surface (known as the Fermi arc surface state) demonstrate the path of electron momentum in \mathbf{k} space, forming a closed loop via the bulk of the material. (d) Surface states corresponding to the topological insulator. Here, it is clear that the electron does not travel through the bulk, The surface state forms a constant energy contour. 15
- 2.6 (Ref. [29]) (a) Blue and red points and arrow denote Weyl points of opposite chirality. The green arc shows the Fermi arc surface state. (b) Theoretically calculated location of Weyl points and corresponding Fermi arcs. $\bar{\Gamma}, \bar{X}, \bar{M}, \bar{Y}$ denote various symmetry points in the TaAs crystal. (c) Experimental determination for Fermi arc surface state (blue circles). (d) Energy scan of the TaAs, using ARPES, shows linear dispersion, and two Dirac cones separated symmetrically about $k_y = 0$, suggesting them to be a pair of Weyl points with opposite chirality. . . 16
- 2.7 (Ref. [30]) (a) shows the curvature of the earth's surface and the path of the pivot of an oscillating pendulum moving from the north pole to the equator, and then back to the north pole. (b) shows the path of the pivot moving in a circular path at a constant latitude position (θ). 17
- 2.8 (Ref. [33]) Red and blue Dirac cones in (a) representing Weyl points of opposite chirality. (b) shows a pair of Weyl fermions in phase space. The red and blue show the flux of the Berry curvature from one monopole to another, illustrating the flux of the magnetic field between two monopoles. 20

2.9	(Ref. [25]) Origin of the chiral anomaly. The dispersion of the lowest band is opposite for the Weyl points with \pm chirality. Top: figures show the equilibrium of left and right-handed Weyl points in the presence of the magnetic field and the absence of an electric field. Black and gray dots represent filled and empty states. Bottom: the same Weyl Fermions under the application of electric and magnetic field along the same direction, which results in the displacement of states by $\delta\mathbf{k} (\propto -\mathbf{E})$ along the field direction. This creates an imbalance in the electronic states, leading to additional conductivity in the material.	23
2.10	(Ref. [39, 40]) Chiral anomaly in Dirac semimetal - Na_3Bi . Na_3Bi becomes Weyl semimetal under the application of the external magnetic field, because of the broken TR symmetry. The Dirac cones split into Weyl cones in the same direction as the field is applied. When the magnetic field is applied parallel to the electric current, chiral anomaly-induced negative magneto-resistance (MR) is observed, as shown in (a), corresponding to the Na_3Bi Dirac semimetal. Angular MR and planar Hall effect for the Na_3Bi is shown in (b, c), respectively. Sample contacts and measurement setup for (b, c) are shown in the (b) inset.	24
2.11	(Ref. [51]) Crystal structure of Mn_3X and its symmetry planes are shown in (a). The mirror reflection in x, y, z planes and time reversal symmetry can be denoted by M_x, M_y, M_z and T , respectively. Magnetic structure of Mn_3Ge in a - b plane is shown in (b). The symmetry axes are labeled and shown as dotted lines. The symmetry planes and location of Weyl points are shown in the 3D lattice structure in (c). The location of Weyl points and corresponding Fermi arcs are shown in (d).	27
2.12	(Ref. [58]) Scattering geometry for the derivation of diffraction cross section. Here, \mathbf{k}, \mathbf{k}' denote the incident and scattered wave vector. ϕ is the arbitrary azimuthal angle corresponding to the scattering cross section. $2\theta_s$ denotes the scattering angle with respect to the incident wave vector.	29
2.13	(Ref. [59]) Scattering geometry for far field condition: $ \mathbf{r} - \mathbf{r}' \approx \mathbf{r} $	30
2.14	Illustration of the interplanar path difference observed by the incident wave is shown in different ways in (a, b). \mathbf{k} and \mathbf{k}' denote incident and diffracted wave.	32

2.15 (Ref. [61]) Ewald construction in reciprocal space for elastic scattering.	33
2.16 (Ref. [58]) Normalized scattering form factor of Cr corresponding to the different sources of scattering is shown with respect to the change in scattering vector (or scattering angle (2θ)).	35
2.17 Illustration of the magnetic scattering where only the magnetization component perpendicular to the Q is relevant. \mathbf{M}_\perp lies in the plane defined by $\mathbf{Q} - \mathbf{M}$;	39
3.1 (a) Induction melting device. The sample is sealed into a quartz tube, under a high vacuum. (b) Schematic diagram of induction melting, showing various components of the instrument. (Taken from Ref. [65])	43
3.2 (Taken from Refs. [66, 67]) (a) Illustration of the vertical gradient method. Where, the sealed quartz tube is kept in the furnace, having a vertical temperature gradient such that it is coolest at the bottom and hottest at the top. The temperature is controlled by the controller. (b) Schematic diagram of the vertical Bridgeman furnace in which sample (sealed inside the crucible) is kept under a temperature gradient. The crucible is pulled down very slowly, leading to the formation of a single crystal starting from the bottom, which cools first.	44
3.3 (Ref. [68]) Various parts of the instrument were used to analyze the elements of the compound under study, using the ICP-OES method. The diagram in the inset illustrates optics, which shows how the characteristic light is filtered out to the detector.	46
3.4 (a) shows the Guinier geometry (taken from [69]) which is used in the powder diffractometer to collect the data. (b) shows an X-ray powder diffractometer instrument with various components.	48
3.5 (Ref. [69]) X-ray Laue camera, and illustration of the single crystal scattering leading to the formation of a Laue pattern.	49
3.6 SuperNova (6- circle) single crystal diffractometer which operates on the transmission geometry. The source of X-ray is Molybdenum (Mo). .	50
3.7 (Ref. [70]) Illustration of the working principle of the VSM setup. . . .	51

3.8	(a) shows the sample contact made on the resistivity puck, which is used in the PPMS for resistivity measurements. (b) shows the Hall and longitudinal resistivity contacts. The electric current along the length of the sample (I_{\pm}). For longitudinal resistivity, the voltage is measured along the direction of the current, denoted as V_{\pm} . However, Hall voltage contacts (shown as $V_{H\pm}$) are made in the transverse direction, to measure the transverse resistivity. Usually, Hall resistivity and longitudinal resistivity are measured separately, except in a few cases when necessary. (c) shows the rotator option available in the ppms, which can rotate the sample with respect to the external magnetic field.	53
3.9	(Taken and modified from Ref. [71, 72]) (a) Time-dependent magnitude of the various pulsed magnetic fields. Magnets A, and D correspond to the 8.5 MJ and 1.5 MJ, respectively, which lie within the 24 mm bore region. Magnet B has a double coil with 9.5 MJ energy, leading to 91.4 T of the maximum magnetic field, for short time, in a 16 mm bore. Magnets C and E correspond to the 1 MJ and 43 MJ energy, respectively, in the 20 mm and 40 mm bore regime. (b) Experimental setup for the high field resistivity measurements. (c) Illustration of the various components of the high field resistivity setup.	54
3.10	(a) Different parts of the D23 instrument (modified from Ref. [73]). (b) Few parts of the HeiDi instrument are shown (modified from Ref. [74]). (c) The illustration of scattering geometry corresponding to both the instruments.	56

- 3.11 (a) Scattering geometry for the spherical neutron polarimetry measurement. P_i, P_i' denote i^{th} component ($i = x, y, z$) of the polarization of incident and diffracted beam, respectively. \mathbf{Q} is the scattering vector, which defines the x axis. (b) Pictorial representation of the different components of the CRYOPAD instrument (modified from Ref. [76]). 1: Incident beam nutator (magnetic path containing longitudinal static guide field). 2: Outer superconducting shield (Niobium) 3: Precession coil (rotates the incident beam polarization around a horizontal axis perpendicular to the incident beam). 4: Precession coil for diffracted beam (aligns the chosen polarization component to the axis of the diffracted beam). 5: Inner superconducting shield (protects magnetic field due to precession coils, and maintains a zero-field environment in the sample chamber). 6: Nutator of the diffracted beam (c) A picture of the CRYOPAD setup installed with the D3 setup. A few parts are also shown (taken from [77]). 60
- 4.1 (a) Binary phase diagram of Mn - Ge[79]. (b) Binary phase diagram of Fe - Ge [81]. In both cases, ε and ε_1 phases (encircled by red) denote hexagonal and tetragonal phases. 63
- 4.2 The table on the top shows the position of atoms corresponding to space group $P6_3/mmc$. The figure below shows nuclear structure of $(\text{Mn}_{1-\alpha}\text{Fe}_\alpha)_3\text{Ge}$ in two different orientations. 65
- 4.3 (a - f) X-ray powder diffraction of $(\text{Mn}_{1-\alpha}\text{Fe}_\alpha)_{3.2}\text{Ge}$. ‘Hex.’ and ‘Tet.’ refer to the hexagonal and tetragonal phases of the compound, respectively. χ^2 denotes the goodness of the fitting parameter. 66
- 4.4 Change in the a and c lattice parameters of Hexagonal - $(\text{Mn}_{1-\alpha}\text{Fe}_\alpha)_{3.2}\text{Ge}$ with increase in Fe doping fraction (α) in place of Mn. Inset: change in lattice volume with α 67
- 4.5 Laue diffraction of Mn_3Ge with $P6_3/mmc$ symmetry. (a-c) denote Laue pattern when X-ray beam parallel to x $[2\bar{1}\bar{1}0]$, y $[01\bar{1}0]$, z $[0001]$ axes, respectively. 67
- 4.6 SC-XRD corresponding to the $(hk0)$ and $(h0l)$ planes for Mn_3Ge and $(\text{Mn}_{(0.78)}\text{Fe}_{0.22})_{3.2}\text{Ge}$ with $P6_3/mmc$ symmetry. 68

5.1	Magnetization of the S2 and S3 samples, denoted by $\delta = 0.2$ and $\delta = 0.5$, respectively. The direction of the applied magnetic is mentioned in the plot. The measurement was performed in field cooling (FC) condition under 100 Oe of the applied magnetic field.	72
5.2	Field dependent magnetization of the S2 and S3 samples along various axes mentioned in each plot.	72
5.3	Longitudinal resistivity of the Mn_3Ge corresponding to S2 and S3 samples, which are denoted by $\delta = 0.2$ and $\delta = 0.5$, respectively.	73
5.4	(a) shows LMR along the x axis, corresponding to the Mn_3Ge . Here, $\Delta\rho = \rho(B) - \rho(0)$. At high field ($B > 5$ T), the data is fitted with $\rho_{[\text{high } B]} = \alpha(B/\rho_0)$, and fitting is denoted as ‘Fit’. I, II, and III denote three different field regimes where the nature of LMR is different. (b) Temperature dependence of α (high field slope) corresponding to different samples. (c), and (d) show LMC along the x axis, for S2 and S3 samples, respectively. Here, $\Delta\sigma_{ii} = \sigma_{ii}(B) - \sigma_{ii}(0)$. In the case of S2 and S3 samples, LMC below 0.8 T and 0.4 T, respectively, is fitted with $\sigma_{[\text{low } B]} = c_{w2}B$. The evolution of c_{w2} with temperature is shown in (d) inset.	74
5.5	LMR corresponding to the S1 sample. Here, ‘Center’ and ‘Side’ denote the voltage measured at the center and side of the sample as shown in the picture. 0° , and 5° denote the mutual angle between the magnetic field and electric current.	75
5.6	MR of Mn_3Ge (S2) at 4 K and 300 K in various combinations of the current and magnetic field as mentioned in the plot.	76
5.7	(a-c) High magnetic field LMR and transverse MR (TMR) for with current measured along the y axis, and field applied along the x and y axis for LMR and TMR measurement.	78
5.8	(a) LMC along the z axis. The data at high field ($B > 3$ T) is fitted (fit) with $a_0 + a_1 B^2$, where a_0 and a_1 are the fitting parameters. (b, c) LMC corresponding to the S2 and S3 samples, with the magnetic field applied along the z axis.	80
5.9	(a-c) θMR corresponding to the $\text{I}\parallel B\parallel x$; B rotated from z to x axis. The experimental setup is illustrated in (c).	81

- 5.10 (a-f) denote θ MR corresponding for $I\|B\|z$; B rotated from x to the z axis. The experimental setup is illustrated in (c). (f) Inset: θ MR at 370 K, which is above the T_N 82
- 5.11 (a-c) denote θ MR corresponding to the $I\|B\|y$; B rotated from y to the x axis. The experimental setup is illustrated in (a). 83
- 5.12 (a-f) denote θ MR corresponding to the $I\|B\|x$; B rotated from x to y axis, for Mn_3Ge (S2) sample. (g, h) show temperature and magnetic field dependence of θ MR oscillations. $\Delta\rho_{xx} = \rho(\theta_{max.}) - \rho(0)$, where $\theta_{max.}$ means θ at which the maximum magnitude of oscillation is observed. 84
- 5.13 (a-d) denote field dependence of Hall resistivity with the magnetic field applied along the different axis mentioned in each plot. The straight line in (a) shows the linear fitting of the Hall resistivity in the field range of -9 T to -3 T, and the y axis intercept (ρ_{xz}^A) is known as the anomalous Hall resistivity. (e), (f) show the temperature dependence of anomalous Hall conductivity (σ_{ij}^A) for S1 and S2 samples, respectively. 86
- 5.14 (a) denote magnetic structure when $B\|y$ is applied, or $B = 0$. (b) correspond to the magnetic structure when $B\|x$ is applied. [87, 88]. Green dashed lines illustrates symmetry planes, where M_x, M_y implies mirror-plane in x - z and y - z planes, respectively. T corresponds to the time-reversal symmetry. $\tau = \frac{c}{2}$ means the translation along the c axis (or z axis) by $\frac{c}{2}$. (c) shows lattice structure of Hexagonal - Mn_3Ge 87
- 5.15 Temperature dependence of Hall coefficient (R_H) for different samples, under different conditions. 89
- 5.16 (a, c - f) corresponds to the PHE for Mn_3Ge (S2) sample. The measurement setup is illustrated in (b). (g, h) show temperature and magnetic field dependence of PHE oscillations. $\rho_{xy}^{Planar-max.} = \rho_{xy}^{Planar}(-45^\circ) - \rho_{xy}^{Planar}(0)$ 90
- 5.17 Various possible magnetic models of Mn_3Ge , based on the magnetization of the sample. In the case of (I, III) models, moments lie towards the $[01\bar{1}0]$, and in (II, IV) moments are along the $[2\bar{1}\bar{1}0]$ axis. 92
- 5.18 Calculated vs. observed intensity corresponding to model I, at different temperatures. F_c^2 , and F_o^2 denote calculated and observed intensities, respectively. 93

5.19	Evolution of the magnetic moment with temperature. Black dots represent the magnetic moment determined by the data fitting at 4 K, 175 K, and 300 K. The data (red dots) follows the blue curve (Fit), which corresponds to the equation: $\mu(T) = \mu_0(1 - T/T_N)^\beta$, where $\beta = 0.16(1)$.	94
5.20	Temperature dependence of the lattice parameters determined by the X-ray powder diffraction analysis. Inset: Evolution of the lattice volume with temperature.	95
6.1	(a) Crystallographic axes in the hexagonal and Cartesian coordinate. (b) Picture of the crystal used during the neutron diffraction. (c) Illustration of the diffraction geometry of the CRYOPAD setup. The sample is rotated in the x - y plane. P' and P denote scattered and incident neutron beam.	100
6.2	Temperature dependent magnetization (M) of the sample along (a) x axis, (b) y axis and (c) z axis. ZFC, FCC, and FCW denote zero field cooling, field cool cooling, and field cool warming conditions. The measurements were performed with 100 Oe of applied magnetic field. (d-f) shows the field dependent magnetization ($M(H)$) along three different axes (x , y , z). Low field (magnified) $M(H)$ along the x , y , z axes are shown in the inset of (d, e, f), respectively.	101
6.3	Temperature dependent magnetic susceptibility of the sample at 10 Hz, 5 kHz, 10 kHz frequency. The samples oscillates along the x axis. χ' show real part of the AC magnetic susceptibility. Inset: χ'' shows imaginary part of the AC magnetic susceptibility of the sample along the x axis. Dashed line show the onset temperature of the tiny FM in the sample.	103

- 6.4 (a) Resistivity of the sample along the different axes mentioned in the plot. A magnified version of resistivity near 120 K is shown in the inset. The legends showing (W) and (C) imply that the data were collected while warming, and cooling the sample, respectively. (b) Hall resistivity of the compound with the magnetic field applied along the z axis. (c) Hall resistivity of the sample with current is applied along the z axis, and the magnetic field is applied along the x axis. The data were anti-symmetrized to extract the pure Hall contribution and deduct the magneto-resistance contribution. Non-zero Hall resistivity was observed, at a few temperatures, as the field approaches zero. The residual Hall resistivity is marked as ρ_{zy}^A , which is known as anomalous Hall resistivity (AHR). (d) shows the temperature dependence of the AHR and anomalous Hall conductivity (AHC) corresponding to the $B \parallel x$ 105
- 6.5 (a-d) Calculated (cal.) vs. observed (obs.) intensity at 300 K, 130 K, 85 K, and 4 K, respectively. Except at 300 K, the intensities at 4 K, 85 K, and 130 K correspond to the magnetic and nuclear contributions. The fitted models are mentioned in each plot and shown in the Fig. 6.6. 107
- 6.6 (I-IV) shows various magnetic models used for the neutron diffraction data analysis in the AF-I regime. In this case, the a and b axes are along the $[2\bar{1}\bar{1}0]$, and $[\bar{1}2\bar{1}0]$ crystallographic directions. (V-VI) denote the magnetic model with the moments lying along the z axis ($[0001]$). . 108
- 6.7 (a, b) shows variation of (110) and (101) reflections, respectively, with temperature. The reflections were measured using the D23 instrument while warming the sample. Obs. and Cal. denote observed and calculated intensity. (n) and (m) imply the nuclear and magnetic intensity contributions, respectively. The arrow pointed at 4 K, 85 K, and 130 K nuclear data means that the nuclear contribution is calculated using the D23 data analysis at these temperatures. Beyond 242 K, the sample is non-magnetic, therefore observed intensity is the same as the nuclear intensity. The dashed (yellow) line in (b) is a guide to the eye and represents the order parameter in the AF-II regime. 111

6.8	(a, b) Measured and calculated polarization, at 130 K, corresponding to the P_{ij} matrix elements, determined for the different (hkl) planes mentioned on the top. The reflection which is followed by # suggests that the incident polarization was reversed.	113
6.9	(a, b) Measured and calculated polarization at 4 K, corresponding to the different crystallographic planes mentioned on the top. Same as previous, the reflections followed by # suggest the reversed incident polarization.	114
7.1	Magnetic and nuclear structure of $(\text{Mn}_{0.78}\text{Fe}_{0.22})_3\text{Ge}$ ($T = 130\text{K}$) as determined in the chapter 6. The crystallographic axes a , b , and c are described in the hexagonal lattice structure. a and b axes are oriented by 120° with each other. However, x , y , z axes form Cartesian coordinate system such that x and y , oriented by 90° with each other, lying within the a - b plane.	119
7.2	(a) Magnetization of the single-crystal (sc) Fe doped Mn_3Ge samples ($\alpha = 0 - 0.22$). Magnetization of polycrystalline (poly) $\alpha = 0.26$ is also shown. (b) Magnetization of the Fe doped samples ($\alpha = 0 - 0.22$) with magnetic field applied along the z axis. (c) Magnetization of the $\alpha = 0.26, 0.30$ (polycrystalline) samples.	120
7.3	(a-f) Magnetic field (B) dependent magnetization (M) of the selected samples which show different magnetization behavior. Each plot shows M - B at different temperatures denoted by different colors (online). For $\alpha = 0, 0.10, 0.22$, measurements were performed using single-crystals (sc) with $B \parallel (x, z)$. (g) $\alpha = 0.30$ sample show average behavior as it is polycrystalline (poly.) in nature.	121
7.4	Magnetic phase diagram of the Fe doped Mn_3Ge . T_{N1} and T_{N2} correspond to the magnetic transitions shown in the Fig. 7.2(a). T_c correspond to the ferromagnetic (FM) transition temperature, which is visible for $\alpha = (0.26, 0.30)$ in the Fig. 7.2(c). AF-I corresponds to the Mn_3Ge type in-plane non-collinear magnetic structure, as shown in the same region. AF-II corresponds to the collinear AFM structure along z axis, as shown within this region. The details of the magnetic structure shown in different phases can be found in the chapter 6. The ground state magnetic structure in the FM regime is not known.	122

- 7.5 Resistivity of single crystal with $\alpha = 0 - 22$ samples. (a, b) denote the zero field resistivity of the different Fe doped samples along x and z axes. 124
- 7.6 Hall resistivity corresponding to the $\alpha = 0, 0.04, 0.10, 0.18, 0.22$. (a, b) shows Hall resistivity at 4 K with the magnetic field applied along the y axis and z axis, respectively. The arrow in (b) denotes the zero field Hall resistivity, which we will refer as anomalous Hall resistivity. (c) A magnified version of the (b), showing Hall hysteresis corresponding to the mentioned compounds. (d, e) Hall resistivity at 4 K and 150 K, respectively, with the magnetic field, applied along the z axis. 126
- 7.7 (a) Temperature dependence of σ_{xz}^A for different samples. σ_{xz}^A for $\alpha = 0.22$ shown in the graph is 3 times more than the actual value. (b) Change in σ_{xz}^A with doping fraction (α), at different temperatures. At 4 K, $\sigma_{xz}^A = 0$ for $\alpha = (0.17, 0.22)$ therefore not shown here. The data at 150 K and 200 K follow exponential decay behavior. Blue lines are the guide to the eye. (c) Temperature dependence of Hall coefficient (R_H) for two Fe doped samples, which shows different magnetization nature. 127
- 7.8 Field dependence of magnetization and Hall resistivity (for $\alpha = 0.30$) plotted together at each temperature $T = 4$ K, 75 K, 150 K, 300 K. . . 128
- 7.9 Raw data of the longitudinal magneto-resistance measurements (raw data) with different locations of the voltage contacts to determined the effect of current jetting in the $\alpha = 0.10, 0.18$ samples. (a, b) show contacts used to measure the current jetting in $\alpha = 0.10$ and $\alpha = 0.18$ compounds, respectively. Sky blue circles denote contacts near the ‘center’ of the sample. Whereas, the orange rectangle encloses the voltage contacts which are at the ‘edge’ of the sample. (c, d) show LMR of the samples (along the x axis) at 4 K and 130 K, respectively. At each temperature, the LMR was measured by the voltage contact which are at the ‘edge’, and ‘center’ of the sample, as shown in (a, b). . 130
- 7.10 Longitudinal magneto-conductivity (LMC) of the parent and Fe doped samples at (a, b) 4 K, (d, e) 150 K. $\Delta\sigma_{ii} = \sigma_{ii}(B) - \sigma_{ii}(0)$, where, ii denotes the LMC along the i axes. The variation of $\Delta\sigma_{ii}$ ($i = x, z$) at 1 T, with Fe doping fraction (α) is shown in (c, f). 131
- 7.11 LMC for the $\alpha = 0.18, 0.22$ compounds at 4 K, which lies in the AF-II regime. 133
- 7.12 Longitudinal MR for the $\alpha = 0.30$ polycrystalline sample. 134

- 7.13 θ MC measurements for $\alpha = 0-0.22$ with magnetic field and electric current applied along the x axis. (a, b) θ MC measurements, at 1 T, are compared for different compounds, at 4 K and 150 K, respectively. The schematic of the measurement setup is also shown in (a). (c) Temperature dependence of the magnitude of θ MC oscillations ($\Delta\sigma_{xx}^{\text{MC}(\parallel, \perp)}$) corresponding to the different samples. Here, $\Delta\sigma_{xx}^{\text{MC}(\parallel, \perp)} = \sigma(0^\circ) - \sigma(90^\circ)$ at the mentioned temperature and magnetic field. Inset: Variation of the magnitude of the oscillations with an increase in Fe doping compared at different temperatures. (d) Magnetic field dependence of the magnitude of the θ MC oscillations corresponding to the $\alpha \leq 0.22$ compounds. 135
- 7.14 (a, b) Planar Hall effect measurement (PHE) of the Fe doped samples at 4 K and 150 K, respectively. A schematic of the experimental setup is shown in (a), where the sample is rotated such that the magnetic field makes an angle θ with the current direction. (c) Here, $\Delta\sigma_{xx}^{\text{Pl. mag.}}$ denote the magnitude of oscillations determined by the data fitting using Eqn. (7.2). Temperature dependence of the $\Delta\sigma_{xx}^{\text{Pl. mag.}}$ corresponding to different compounds mentioned in the plot. Inset: Evolution of the PHE magnitude, at different temperatures, with Fe doping fraction. (d) Magnetic field dependence of the magnitude of PHE oscillations for the $\alpha \leq 0.22$ compounds. 137

List of Tables

2.1	Conditions for the existence of Weyl nodes. TR symm. and SI symm. denote time reversal and space inversion symmetry, respectively. ‘Min. N_W ’ implies the minimum number of Weyl point allowed in the given case.	14
4.1	Stoichiometry of the compound taken before preparation is mentioned in the first column as ‘Starting stoich.’. After the synthesis, the stoichiometry of the compounds determined by the chemical analysis is mentioned in the second column as ‘Final stoich.’. 14% and 26% Fe doped samples were very small in amount, so chemical analysis could not be performed (mentioned as ‘Not done’). The samples are symbolized or mentioned in the following chapters as mentioned in the third column (‘Referred as’). The sample type is mentioned in the fourth column. SC and poly denote the single crystal and polycrystalline nature of the sample, respectively.	64
5.1	Refinement result of the neutron diffraction analysis. The goodness of the fitting parameter (χ^2) at different temperatures, corresponding to different models.	93
5.2	Refined parameters determined after the neutron diffraction data refinement, using the magnetic model I.	93
6.1	The refined parameters of the D23 data analysis, at different temperatures, corresponding to the best fitted magnetic models.	109
6.2	Goodness of fitting parameters for the D23 data, at 130 K, fitted with different possible magnetic models.	110
6.3	Goodness of fitting parameters for the D23 data. The data at 85 K and 4 K were fitted with different possible magnetic models.	110

- 6.4 The reduced χ^2 (χ_r^2) - the goodness of fit statistical parameter for the CRYOPAD experiment data. The data were fitted with the various possible magnetic models at the mentioned temperatures. 112
- 6.5 Refined parameters at 4 K and 130 K, corresponding to the magnetic models which fit best with the CRYOPAD experiment data. Here, $(hk0)$ and $(h0l)$ denote the experimental configuration where c and b crystallographic axis, respectively, of single crystal was kept along the z axis (vertical position) of the instrument. 114

1 Introduction and motivation

The fusion between topology - a mathematical concept - with quantum mechanics gives rise to the new phases of materials in condensed matter physics, known as topological materials. The physics behind the topological materials helps us understand the origin of the underlying exotic transport phenomena. In search of exciting emergent phenomena with exceptional transport properties, the scientific community started looking for materials with strong electronic correlation blended with the robust topology of the electronic bands. The discovery of a large anomalous Hall effect in a chiral antiferromagnetic system (Mn_3Sn) has triggered enormous experimental and theoretical research in the field of topological materials and spintronics [1, 2].

Weyl semimetals are the special type of topological materials in which the 3D Dirac points split into a pair of Weyl points with opposite chirality because of the broken time-reversal symmetry, or/and broken space inversion symmetry. The unique topological electronic bands near the Fermi surface results in a non-vanishing Berry curvature in the system. In the case of Weyl semimetals, a pair of Weyl points act as a source and sink of Berry curvature. The topological materials which possess large Berry curvature in phase space act as if an intrinsic magnetic field is present inside the system. However, unlike ferromagnetic systems, the magnetic field in phase space cannot be measured using direct methods like magnetization measurements. Experimental signatures of the Weyl semimetals include the observation of Fermi arc surface state, and several exotic transport effects, like chiral anomaly, and anomalous Hall effect, magneto-optical Kerr effect.

Among all the topological materials, special attention has been given to the non-collinear antiferromagnetic Weyl semimetals because of several reasons. Most importantly, because the antiferromagnetic Weyl semimetals do not generate a stray magnetic field (like ferromagnetic materials), still, they give rise to anomalous transport effects due to the presence of the intrinsic magnetic field. Such an intrinsic magnetic field is generated by the pairs of Weyl points acting as a pair of magnetic monopoles.

This thesis focuses on the microscopic and macroscopic measurements and analysis of the parent and Fe doped Mn_3Ge compound. Our primary goal is to look for the evolution of various electrical transport effects (along the different crystallographic axes) with the change in the magnetic field, temperature, and concentration of Fe doping. We predict the qualitative nature of the dynamics of the Weyl points. With the help of detailed analysis, we interpret the change in the location of Weyl points relative to the Fermi surface and the evolution of the separation between a pair of

Weyl nodes. The existence of Weyl points in the centrosymmetric systems relies on broken time-reversal symmetry (TRS) or magnetic symmetry of the system. Therefore, different neutron diffraction techniques were used to determine the magnetic structure of the parent and doped sample in all the different magnetic regimes.

Outline

The details of the scientific background of the research work are discussed in the **chapter 2**. In the beginning, the theoretical understanding of topological materials, the Berry phase has been discussed. After that, the origin of the anomalous Hall effect is discussed. Subsequently, chiral anomaly and its experimental signatures are discussed. In the end, the details of the scattering theory are discussed.

The details of the experimental methods and instruments used during our research work are mentioned in **chapter 3**. Along with the several in-house measurements, large-scale facilities have also been used during the research, which is also discussed in this chapter.

Details of the synthesis of parent and Fe doped powder and single-crystal samples are described in the **chapter 4**. The basic characterization of synthesized compounds is also discussed here.

To look for the chiral anomaly and explore the characteristics of the Weyl point in chiral antiferromagnets, the magnetic and transport properties of the Mn_3Ge are discussed in the **chapter 5**. Here, we attempt to analyze the qualitative behavior of Weyl point and induced chiral anomaly effect with change in temperature, magnetic field, magnetization, and lattice parameters.

Further, we started our study with Fe-doped Mn_3Ge single crystals. Since the magnetic structure of the doped sample is of primary importance, neutron diffraction measurements of the Fe doped samples were performed and analysis is discussed in the **chapter 6**.

We observed that a large range of Fe doped samples show Mn_3Ge type magnetic structure, which suggests that the Weyl points might exist in the doped samples as well. With this motivation, we performed a detailed electrical transport measurement and analysis of Fe doped samples, as mentioned in the **chapter 7**.

The combined analysis of chapters 5 - 7 gives a *qualitative* pattern of the dynamics of Weyl points, which we have summarized in the **chapter 8**. The prospects of our research are also discussed in the same chapter.

2 Scientific background

2.1 Topology

Topology is the branch of mathematics, that deals with patterns of geometrical shapes. Let's begin with a simple example: Case I: a circle, square, and triangle are different in shapes, but they are topologically equivalent as they can be interchanged into one another just by reshaping. Also, they all have one thing in common- they have just one hole to pass through, which is invariant. Case II: the shape- '○' cannot be converted to the shape of '∞' by any means of twisting, folding, or bending. Therefore, '○' and '∞' are topologically different. One of the famous examples of topologically inequivalent shapes is the Möbius strips, shown in Fig 2.1(a, b). Möbius strips are made by twisting a ribbon and joining them end to end. Fig. 2.1(a, b) show Möbius strips with one and two twists, respectively. Where, it can be noted that both the strips cannot be converted into one another by any means without cutting it. Therefore, Möbius strips are considered as topologically protected. Another famous example of topological shapes is the knots in a string. Four shapes with a different number of knots are shown in Fig. 2.1(c-f). All these shapes are topologically protected as they cannot be into one another without cutting them.

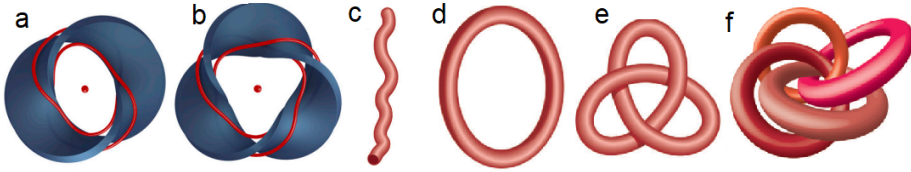


Figure 2.1: (Ref. [3, 4]) Möbius strips, made by joining them end to end, after twisting them one and two times are shown in (a) and (b), respectively. The red line illustrates a particular surface of the strip. (c-e) Different types of topologically inequivalent knots.

After generalizing the above examples, it can be said that the shapes which *cannot* be converted into each other without cutting, bending, or tearing are known as *topologically inequivalent*. However, shapes which *can* be converted to each other by cutting, bending, or tearing are known as *topologically equivalent*. The characteristic of the material which remains the same while twisting, stretching, or bending, is known as topological invariant quantity. Topological shapes are meant to be robust in nature. In the Fig. 2.1, the number of twists and knots are the topologically invariant quantity.

2.2 Topological materials

Until a few decades back, topological phases were observed in the case of 2D materials, which give rise to the integer quantum Hall effect. However, it was realized by the phenomenal work of Haldane (1988) [5] that the topological phases can exist in 3D materials, which was later verified by the discovery of topological insulators [6, 7]. Topological states are predicted by a mathematical invariant quantity, which, in the case of topological states, is the integral over the electron wave function. Similar to the real space knots shown in the Fig. 2.1(e, f), different quantities (like- integral over the electron wave function in \mathbf{k} space) of the topological materials remain topological invariant, which makes it robust in nature. In another word, it can be said that the ‘invariant quantity’ in topological materials is ‘knotted’ in the \mathbf{k} space, as long as the topology of the electronic bands does not change [4].

Valence and conduction bands show different types of dispersion relations in various materials. The presence of strong spin orbit coupling (SOC) in 3D materials can lead to the inversion of valence and conduction bands near the Fermi surface as shown in the Fig. 2.2(a). The intricate connection between the topology of the bands and various symmetries like space inversion (SI), and time reversal (TR) can give rise to various topological states of matter, which we will discuss in detail below.

2.2.1 Topological insulators

In some cases, inverted electronic bands of 3D solids create a band gap inside the bulk, leading to a non-conducting state in the bulk, as shown in Fig. 2.2(b). However, due to its topology, they possess metallic or gapless electronic states near the surface of the material. Such materials with insulating bulk but conducting surface state are known as topological insulators. Ref. [4] justifies that in the case of topological insulators, the metallic surface has to exist. The metallic surface state within the insulating bulk band gap is protected by the time-reversal symmetry. The surface states show linear dispersion (like Dirac cones), where electron momentum and spin are perpendicularly interlocked [10, 8]. The topological invariant quantity for topological insulators is given by Ref. [11]. The examples of Topological insulators are Bi_2Se_3 and family [12], HgTe [13], $\text{Bi}_x\text{Sb}_{(1-x)}$ [14, 15].

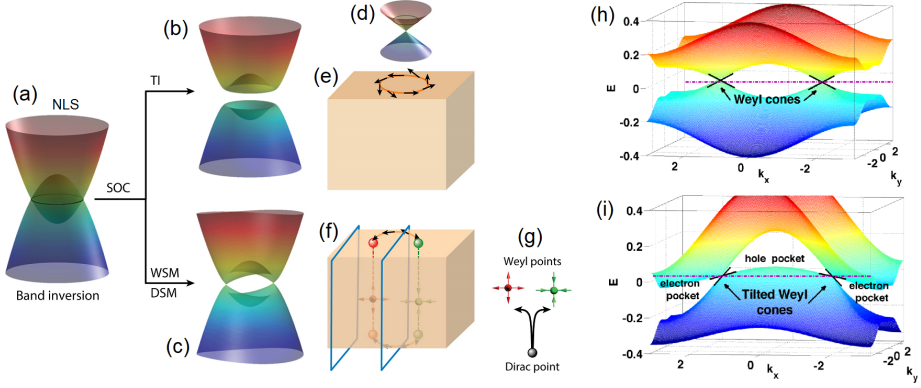


Figure 2.2: (Ref. [8, 9]) The overlap of conduction and valence bands inverts the electronic band, which is shown in (a). Weak or absent the spin orbit coupling (SOC) gives nodal line semimetal shown in (a). Strong SOC may lead to topological insulator (TI), Weyl semimetal, or Dirac semimetal, which are shown in (c, d). (d) shows the gapless surface state which is present in TIs. The orange circle and spins in (e, f) show spin-momentum locked surface state corresponding to the TI, and Weyl semimetal, respectively. (g) shows the splitting of the Dirac point, induced by the broken symmetry, into a pair of Weyl points shows. (h) shows Weyl semimetal of type-I. (i) Weyl semimetal of type-II, where Weyl cones are tilted towards the x axis. This modifies Weyl Hamiltonian as: $H_{\chi} = \hbar v_F (\chi \mathbf{k} \cdot \boldsymbol{\sigma} + \gamma_t k_x)$, where γ_t is the tilt parameter [9]. $|\gamma_t| < 1$ ($|\gamma_t| > 1$) leads to the type-I (type-II) Weyl nodes. In the case of type-II Weyl nodes, the Fermi energy crosses the lower and upper band as well, giving rise to the electron and hole pockets.

2.2.2 Nodal line semimetal

In some materials, the spin orbit coupling (SOC) is very small or small, leading to the crossing of the conduction and valence band along a line or circle, as shown in the Fig. 2.2(a) [16]. Material with such band crossing is known as nodal line semimetals (NLS). [16, 17, 18]. Such a closed loop of nodal lines forms within the 3D Brillouin zone (BZ) exist when inversion symmetry is present. The nodal line semimetal comes in several forms, depending on the band structure and underlying symmetry protection. When time reversal and space inversion symmetry is protected, the nodal line semimetals are entirely gapless only in the presence of SOC. Closed nodal lines also exist when the mirror plane is present in non-centrosymmetric materials. Ca_3P_2 [19], ZrSiS [20], and their family are the typical examples of such materials. Apart from the closed nodal

lines, different types of symmetry can lead to the straight nodal lines also, across the BZ [18]. Being a topological material, the topological invariant quantity in nodal line semimetals is the winding number (w), defined as: $w = \oint_l \mathbf{A} \cdot d\mathbf{l}$. Where, l denotes the nodal line, and \mathbf{A} denotes the Berry connection.

2.2.3 Dirac semimetal

Dirac semimetals are one of the consequences of band inversion in presence of the strong SOC. In this case, band gaps open near the crossing of the bands throughout the ring, except at a few points, where the valence and conduction band touches each other known as Dirac point. 2D Dirac semimetals are easy to visualize compared to the 3D Dirac semimetals, where energy dispersion is linear along all the three k_x, k_y, k_z axes. Dirac semimetals are assumed to host Dirac fermions as (low energy) quasiparticle excitations, which give rise to exotic transport phenomena, including metallic surface states. 2D Dirac semimetals are fragile and topologically unprotected because they can be gapped simply by introducing the magnetic field, or other perturbations. On the other hand, 3D Dirac semimetals are stabilized by a crystalline point group symmetry, and topologically protected by the space inversion and time reversal symmetry of the material. The topological Dirac semimetal phase can also be regarded as an intermediate state between the transition from normal insulators to topological states [21], as shown in the Fig. 2.3.

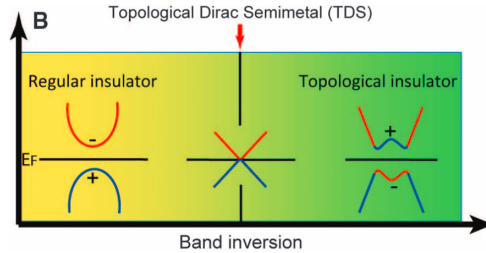


Figure 2.3: (Ref. [21]) Evolution of the band structure from normal insulator to topological insulator, determined by the strength SOC, which can be achieved by the doping of the sample [22]. The symbols '+' and '-' denote odd and even parity of the bands near the point where time-reversal symmetry is invariant.

2.2.4 Weyl semimetals

The nodal points of Dirac cones are doubly degenerate, where Weyl points of opposite chirality coincide. Therefore, often Weyl semimetals are also referred as topological Dirac semimetals. The doubly degenerate Dirac points are protected by the space inversion symmetry and time reversal symmetry. Therefore, destruction of at least one of time reversal or space inversion symmetry lifts the degeneracy, leading to the emergence of a pair of Dirac points with opposite chirality, as illustrated in the Fig. 2.2(c, g). Such a pair of Dirac points are referred as Weyl points, and the materials which host Weyl points are known as Weyl semimetals.

In 1928, P. A. M. Dirac led a foundation for the unification of special relativity with quantum mechanics using the Dirac equation:

$$(i\hbar\gamma^\mu\partial_\mu - mc)\psi = 0 \quad (2.1)$$

Where, $\mu = 0$ corresponds to the time, and $\mu = (1, 2, 3)$ denotes three spatial dimensions. Its solutions predict three relativistic particles namely Majorana, Dirac, and Weyl fermions. In 1929, Hermann Weyl suggested that the massless Dirac equation give rise to the Weyl equation:

$$\gamma^\mu\partial_\mu\psi = 0 \quad (2.2)$$

Where, $\gamma^\mu = (\gamma^0 \ \gamma^1 \ \gamma^2 \ \gamma^3) = (\mathbf{I}_2 \ \sigma_x \ \sigma_y \ \sigma_z)$, \mathbf{I}_2 denotes identity matrix. σ_i ($i = x, y, z$) denote the i^{th} component of the spin matrices. The solution for the Weyl equation can be determined by using trial wave function of form $\psi = \chi e^{-\mathbf{k}\cdot\mathbf{r}}$, where χ is a two component spinor. So, the Weyl equation can be further simplified to [23]

$$i\partial_t\psi_\pm = \mp c\mathbf{p} \cdot \boldsymbol{\sigma}\psi_\pm = H_\pm\psi_\pm \quad (2.3)$$

Here, \mathbf{p} and $\boldsymbol{\sigma}$ denote the electron momentum, and the spin matrices. c is the speed of light. H_\pm refers to the Weyl Hamiltonian. The above equation suggests that Weyl Fermions propagate antiparallel or parallel to the electron spin, which determines the chirality of the Fermions. It is important to notice that the existence of a pair of Weyl points with opposite chirality, in 3D, is natural, so an odd number of Weyl nodes cannot exist in a material. To realize Weyl fermions, they have to separate apart in \mathbf{k} space by lifting the double degeneracy of the band at the Dirac points. Double degeneracy of bands arises when space inversion (SI) and time reversal (TR) symmetry is present in the system, or the system remains invariant under the combined (SI +

TR) symmetry operation [23]. When only TR symmetry is present, the degeneracy is lifted because crystal momentum gets reversed. Similarly, when only SI is present and TR is broken, again the degeneracy is lifted. Therefore, the topological transition from Dirac to Weyl semimetal is strictly governed by the underlying symmetry of the material. Under the application of strain, external pressure, magnetic field, or any other perturbation, the Weyl points move around in the phase space, but cannot be destroyed. The only way to destroy Weyl points is to annihilate the pair of Weyl points into each other. Such robustness originates due to the non-trivial topological protection.

The form of Weyl Hamiltonian ($H_{\pm} = \mp c\mathbf{p} \cdot \boldsymbol{\sigma}$) in condensed matter physics remains the same as particle physics. However, the velocity of Weyl fermions in solid states is considered to be Fermi velocity (v_F), instead of the velocity of light (c). Therefore, Weyl Hamiltonian specific to condensed matter physics can be written as

$$\mathcal{H}_{\pm} = \pm \hbar v_F \mathbf{k} \cdot \boldsymbol{\sigma} \quad (2.4)$$

2.2.4.1 Topological protection in 3D

In a minimal form, Hamiltonian for 2D (x - y plane) Dirac points can be written as [24]

$$\pm \hbar v_F (k_x \sigma_x + k_y \sigma_y) \quad (2.5)$$

After adding a perturbation term along the z axis - $\mu \sigma_z$, the 2D dispersion relation becomes

$$\pm \hbar v_F [k_x \sigma_x + k_y \sigma_y] + \mu \sigma_z \quad (2.6)$$

Which shows a gap in Hamiltonian induced by the perturbation term. Therefore, additional term along z axis can create a band gap (along z component) in case of 2D Dirac materials.

Now, let us consider the case of 3D Dirac points. Assume that the conduction and valence band touch at a point k_0 , within the Brillouin zone (BZ). So, the Weyl Hamiltonian can be expanded (Taylor series) near the k_0 as [25]

$$H_{\chi}(\mathbf{k}) = \chi \hbar v_F (\mathbf{k} - \mathbf{k}_0) \cdot \boldsymbol{\sigma} \quad (2.7)$$

Where $\chi = \pm$ denotes the chirality of the Weyl points. In this case, the Hamiltonian

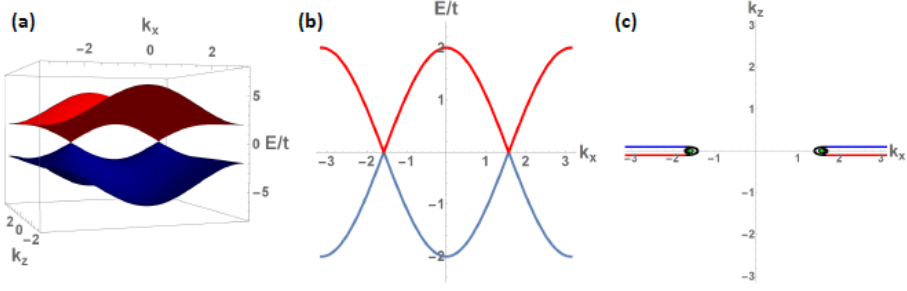


Figure 2.4: (Ref. [26]) The band structure corresponding to the Hamiltonian mentioned in Eqn. (2.13).

can be expanded as [24]

$$\chi \hbar v_F (\mathbf{k} \cdot \boldsymbol{\sigma} - [k_{0x}\sigma_x + k_{0y}\sigma_y + k_{0z}\sigma_z]) \quad (2.8)$$

Now, it is interesting to see that all the dimensions have been used up, so the addition of $\eta\sigma_z$ will only modify it as

$$\chi \hbar v_F (\mathbf{k} \cdot \boldsymbol{\sigma} - [k_{0x}\sigma_x + k_{0y}\sigma_y + (k_{0z} + \eta)\sigma_z]) \quad (2.9)$$

It is obvious to note that the features of the $H(\mathbf{k})$ have not been destroyed as long as the translation symmetry of the crystal persists. If translational symmetry is allowed, the addition of a perturbation term only translates the location of the Weyl point along z component, rather than destroying the gap. It is also worth noting that the dispersion around k_0 is still linear (near Weyl point) in all the 3 directions. Usually, the perturbation in the Hamiltonian can only change k_0 and v_F , which will change the location and slope of 3D Dirac points instead of opening a gap. Therefore, 3D Dirac points are regarded as robust in nature because of such topological protection.

2.2.4.2 Location of the Weyl points

The massless Hamiltonian with Dirac point at \mathbf{k}_0 is given as

$$\mathcal{H} = \pm v_F \boldsymbol{\sigma} \cdot (\mathbf{k} - \mathbf{k}_0) \quad (2.10)$$

Now, if space inversion (SI) symmetry is present in the system,

$$\begin{aligned} \mathbf{k} &\rightarrow -\mathbf{k}, \boldsymbol{\sigma} \rightarrow \boldsymbol{\sigma} \\ \mathcal{H} &\rightarrow \mathcal{H}' = \pm v_F \boldsymbol{\sigma} \cdot (-\mathbf{k} - \mathbf{k}_0) = \mp v_F \boldsymbol{\sigma} \cdot (\mathbf{k} + \mathbf{k}_0) \end{aligned} \quad (2.11)$$

This suggests that the Weyl point at $-\mathbf{k}_0$ has opposite chirality compared to the \mathbf{k}_0 . Therefore, systems with only broken TR symmetry have at least two Weyl points separated in the \mathbf{k} space. It can be verified by the following model. The two-band model Hamiltonian for Weyl semimetals, with *broken* TR symmetry, and *persistent* SI symmetry has been predicted (initially) by Ref. [24], which can be given as a 2×2 matrix form as

$$\begin{aligned} \mathcal{H}(\mathbf{k}) = & -[\zeta(2 - \cos(k_y a_0) - \cos(k_z a_0)) + 2t_x(\cos(k_x a_0) - \cos(k_w a_0))]\sigma_x \\ & -[2t_y \sin(k_y a_0)]\sigma_y - [2t_z \sin(k_z a_0)]\sigma_z \end{aligned} \quad (2.12)$$

Where, ζ is constant, t_i ($i = x, y, z$) denote the hopping parameter, k_i denote crystal momentum, a_0 is the lattice parameter. The band structure corresponding to the defined $\mathcal{H}(\mathbf{k})$ is shown in the Fig. 2.4. It is easy to find that the $\mathcal{H}(\mathbf{k})$ vanishes at $\mathbf{k} = (\pm k_w, 0, 0)$. The $\mathcal{H}(\mathbf{k})$ clearly shows that Weyl points exist on the k_x axis, separated by $|2k_w|$ from each other. The separation between a pair of Weyl points varies depending on the extent of the broken time reversal symmetry or the magnitude of the Zeeman splitting created by the internal magnetic field in the magnetic systems [23].

In another case, where TR symmetry exists,

$$\begin{aligned} \mathbf{k} &\rightarrow -\mathbf{k}, \boldsymbol{\sigma} \rightarrow -\boldsymbol{\sigma} \\ \mathcal{H} &\rightarrow \mathcal{H}' = \pm v_F (-\boldsymbol{\sigma}) \cdot (-\mathbf{k} - \mathbf{k}_0) = \pm v_F \boldsymbol{\sigma} \cdot (\mathbf{k} + \mathbf{k}_0) \end{aligned} \quad (2.13)$$

Interestingly, in this case, the chirality of the Weyl node at $-\mathbf{k}_0$ is the same as the chirality of the Dirac point at \mathbf{k}_0 . Therefore, in this case, to visualize Weyl points, SI symmetry has to be broken. As mentioned by Ref. [27], in the case of broken SI symmetry, Dirac points split in energy space, rather than in \mathbf{k} space, resulting in the formation of at least 2 pairs (total 4) of Weyl points. It is important to note that in both cases of broken symmetry, the Fermi level passes through both the Weyl cones to the same level. So, there is no current flowing within the opposite Weyl cone in

TR symm.	SI symm.	Consequences	Min. N_W
broken	broken	Weyl nodes exist	2
broken	exist	Weyl nodes of <i>opposite</i> chirality at $\pm k_0$	2
exist	broken	Weyl nodes of <i>same</i> chirality exist at $\pm k_0$	4
exist	exist	Weyl points do not exist	0

Table 2.1: Conditions for the existence of Weyl nodes. TR symm. and SI symm. denote time reversal and space inversion symmetry, respectively. ‘Min. N_W ’ implies the minimum number of Weyl point allowed in the given case.

ambient conditions, even if one Weyl cone lies higher than the other.

In summary, broken TR symmetry splits the Dirac nodes in \mathbf{k} space, keeping the energy constant. However, broken SI symmetry splits a Dirac point in energy space, keeping the momentum constant. The possible location and a minimum number of Weyl points determined by the protected and broken symmetries are summarized in Table 2.1.

2.3 Surface states in topological materials

As described by the [4], the topology of material is different outside (vacuum) and inside (bulk) the material, and this change occurs at the surface of the material. Therefore, metallic surface states have to exist in all types of topological materials, either insulators or semimetals. However, it is the nature of the bulk state which differentiates the Weyl, Dirac semimetals, and topological insulators. Usually, it is not easy to determine the type of material using transport measurements. Whereas, the angle resolved photoemission spectroscopy (ARPES) technique can be helpful to probe the bulk of the material (in the phase space). ARPES measurement works based on the photoelectric effect. When a photon hits the material surface at a particular angle, the momentum and energy of the emitted electrons are measured, which provides information about the energy transferred to the material, which provides information about the energy dispersion in the material. Increasing the energy of the incident photon provides the details of the bulk band structure of the sample under the ARPES study.

It is one of the important features of topological materials that show various types of open or closed loops on the metal surface in \mathbf{k} space. In the case of topological insulators, metallic surface states show a closed loop as observed as shown in the

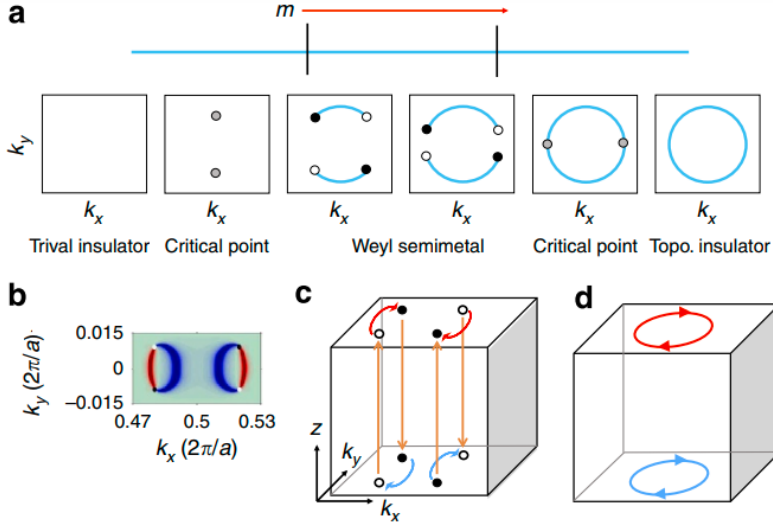


Figure 2.5: (Ref. [28]) (a) Various surface state corresponding to the mentioned topological materials formed by a tuning the parameter m . (b) Calculated Fermi arc surface state of TaAs. (c) Path of the electron when the magnetic field is applied to a Weyl semimetal, along the z axis. Straight arrows show the path of the electron in real space. Filled and open dots show Weyl points of opposite chirality. Red and blue arcs on the surface (known as the Fermi arc surface state) demonstrate the path of electron momentum in \mathbf{k} space, forming a closed loop via the bulk of the material. (d) Surface states corresponding to the topological insulator. Here, it is clear that the electron does not travel through the bulk, The surface state forms a constant energy contour.

Fig. 2.5(a). However, a change in the strength of the spin orbit coupling may close the band gap in the bulk, and the Dirac state is formed (in the bulk). In this case, also, the closed surface states are observed. However, a bulk state is observed as well, as shown by two gray dots (diametrically opposite to each other) in the Fig. 2.5(a) (second last). If the TR symmetry is broken, the bulk Dirac state show splitting and the circle is split into two arcs. These arc-shaped surface states are known as Fermi arc surface states. Fig. 2.5(a) demonstrates that Weyl and Dirac semimetallic states are intermediate stages between topological and trivial insulators.

Fermi arc is considered the unique signature owing specifically to the Weyl semimetals. TaAs is an excellent candidate for the Weyl semimetal. Being a non-magnetic system, the presence of Weyl points very near the Fermi surface makes it a very good

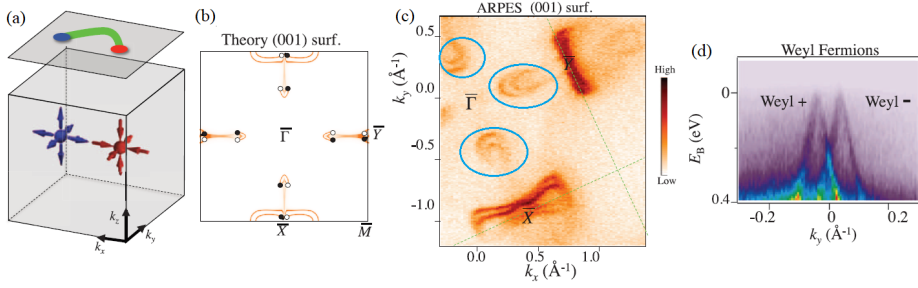


Figure 2.6: (Ref. [29]) (a) Blue and red points and arrow denote Weyl points of opposite chirality. The green arc shows the Fermi arc surface state. (b) Theoretically calculated location of Weyl points and corresponding Fermi arcs. $\bar{\Gamma}$, \bar{X} , \bar{M} , \bar{Y} denote various symmetry points in the TaAs crystal. (c) Experimental determination for Fermi arc surface state (blue circles). (d) Energy scan of the TaAs, using ARPES, shows linear dispersion, and two Dirac cones separated symmetrically about $k_y = 0$, suggesting them to be a pair of Weyl points with opposite chirality.

candidate to observe Fermi arcs. Interestingly, a clear signature of the Fermi arcs has been observed in the ARPES measurements of the TaAs by Ref. [29], as shown in the Fig. 2.6. This was the first experimental discovery of a Weyl semimetal (TaAs). Arc shaped states were observed, which originate from one point and vanishes at another point, corresponding to the Weyl point of opposite chirality. It was observed by Ref. [29] that the arc shape disappears as the energy of the incident photon is increased to look deeper in the energy space. This suggests that the Fermi arc shape exists only on the surface, verifying it to be a unique surface state observed in the Weyl semimetals. Along with the Fermi arc, Weyl cones have also been observed in the energy scan of the ARPES measurement, as shown in the Fig. 2.6(d).

2.4 Berry phase and Berry curvature

According to the adiabatic theorem, if the Hamiltonian of a system changes very slowly, the system remains in the same (time-dependent) ground state. However, the phase of the system changes. Such changes in phases can be understood by a few examples. Let us recall the famous example of an oscillating pendulum whose pivot is moving very slowly (compared to the average speed of the pendulum) on the surface of Earth in the same way as mentioned in the Fig. 2.7(a) [30]. As the pendulum

traverse from pole (P) through Q-R and back to Q, the plane of the oscillation of the pendulum changes without changing the oscillating frequency. The change in the plane of oscillation can be considered as a phase change of the pendulum caused by the slow motion of the pivot. The plane of oscillation changes by Θ compared to the starting plane. It is interesting to note that the Θ is equal to the solid angle (Ω) subtended by the total path as $\Omega = A/R^2 = [(1/2)(\Theta/2\pi)4\pi R^2]/R^2 = \Theta$, where R is the radius of the Earth. So, after a circular path, the pendulum changes its phase, keeping the frequency constant. Another famous example of adiabatic phase change is the Foucault pendulum, which goes through a similar adiabatic process. In contrast to the previous case, the pivot of the oscillating Foucault pendulum remains at a fixed place (Latitude position θ_0), but the rotation of Earth completes the cycle after 24 hr, as shown in the Fig. 2.7(b). In this case, the solid angle subtended $= \Omega = \int \sin \theta d\theta d\phi = 2\pi(1 - \cos \theta_0)$ [30]. So, after every rotation of Earth, the pendulum changes its plane of rotation by $2\pi(1 - \cos \theta_0)$. Therefore, change in the phase of the system is natural in the adiabatic process.

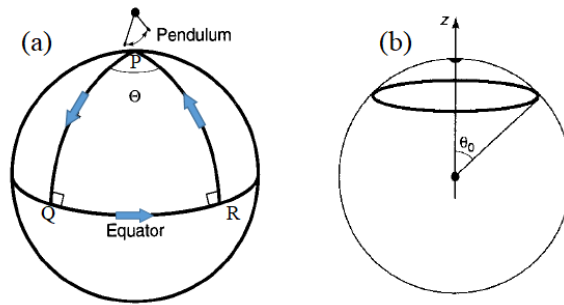


Figure 2.7: (Ref. [30]) (a) shows the curvature of the earth's surface and the path of the pivot of an oscillating pendulum moving from the north pole to the equator, and then back to the north pole. (b) shows the path of the pivot moving in a circular path at a constant latitude position (θ).

Similar to the real space example, an analogy can be made for quantum systems also. The quantum state may change the phase if one of the parameters traverses through a close path. The acquired phase change due to such adiabatic change in the parameter is known as **Berry phase**.

Let us assume a Hamiltonian $H(\mathbf{k}_0)$, constant with time, for a system starting in eigenstate - $|\Psi_n(t)\rangle$.

$$H(\mathbf{k}_0)|\Psi_n(t)\rangle = E_n|\Psi_n(t)\rangle \quad (2.14)$$

In this case,

$$|\Psi(t)\rangle = e^{-iE_n t/\hbar} |n(\mathbf{k})\rangle \quad (2.15)$$

However, if the Hamiltonian is changing adiabatically with time, through $\mathbf{k}(t)$, which can be written as

$$H(\mathbf{k}(t)) |\Psi(t)\rangle = E_n(\mathbf{k}(t)) |\Psi(t)\rangle \quad (2.16)$$

In this case, the solution for the eigenstate is

$$|\Psi_n(t)\rangle = e^{-i\phi(t)} |n(\mathbf{k})\rangle \quad (2.17)$$

$$\phi(t) = 1/\hbar \int_0^t E_n(\mathbf{k}(\tau)) d\tau - \gamma_n \quad (2.18)$$

$$\gamma_n = i \int_0^t \langle n(\mathbf{k}(\tau)) | \frac{d}{d\tau} | n(\mathbf{k}(\tau)) \rangle d\tau = \int_{\mathbf{k}(0)}^{\mathbf{k}(t)} \mathbf{A}_n(\mathbf{k}) \cdot d\mathbf{k} \quad (2.19)$$

Where, $n(\mathbf{k})$ is the Bloch wave function defined for an electronic band with wave vector \mathbf{k} . $\mathbf{A}_n(\mathbf{k})$ is called the Berry connection or Berry potential, and γ_n is known as the Berry phase [31]. In the case of a cyclic process, the system depends on the closed path. So, in the case of closed contour (\mathcal{C}),

$$\gamma_n = \oint_{\mathcal{C}} \mathbf{A}_n(\mathbf{k}) \cdot d\mathbf{k} \quad (2.20)$$

It is interesting to observe that the Berry curvature depends on the path, irrespective of the time taken.

The Berry connection mentioned above can be written in compact forms as

$$\boxed{\mathbf{A}_n(\mathbf{k}) = -i \langle n(\mathbf{k}) | \nabla_{\mathbf{k}} | n(\mathbf{k}) \rangle} \quad (2.21)$$

$\mathbf{A}(\mathbf{k})$ can be regarded as vector potential in electromagnetism. So, a quantity analogous to the magnetic field can be defined as

$$\boxed{\Omega_n(\mathbf{k}) = \nabla_{\mathbf{k}} \times \mathbf{A}_n(\mathbf{k})} \quad (2.22)$$

Where, $\Omega_n(\mathbf{k})$ is known as the **Berry curvature**, which act as to the magnetic flux density in \mathbf{k} space. Now, using Stoke's theorem, and with reference to the Eqns.

(2.20, 2.22), Berry phase can also be written as

$$\gamma_n = \int \Omega_n(\mathbf{k}) \cdot d\mathbf{S} \quad (2.23)$$

Where, $d\mathbf{S}$ denote the area enclosed by the contour \mathcal{C} .

In the case of Weyl semimetals, Weyl Hamiltonian is given by two bands, symbolized by ' \pm '. The Berry curvature corresponding to the \pm band with chirality as χ can be given as [26]

$$\Omega_{\pm}^{\chi}(\mathbf{k}) = \pm\chi \frac{\mathbf{k}}{2k^3} \quad (2.24)$$

In the case of solids, electron momentum is the parameter that determines most of the properties. The electron Wavefunction can change within the unit cell, leading to the origin of the Berry phase and Berry curvature in solid matter. The integral of the Berry curvature is a conserved quantity.

$$\frac{1}{2\pi} \int \Omega_n(\mathbf{k}) \cdot d\mathbf{S} = C_n \quad (2.25)$$

Where, C_n is an integer, known as the Chern number (for the n^{th} electronic band). The Chern number, which is a topological invariant quantity, determines the local stability of the Weyl points. It is important to mention that the Chern number is defined in the case of non-degenerate bands, where an electronic band gap exists. Therefore, $C_n > 0$ only if TR symmetry is broken. The easiest way to break TR symmetry is the application of a magnetic field. Therefore, one of the famous examples of the presence of Chern number is the quantum Hall effect, where the application of a strong magnetic field in a 2D system (electron gas), Landau level separates, leading to the quantization of Hall conductivity as:

$$\sigma_{xy}^{QHE} = \left[\int_{BZ} \Omega_z(k_x, k_y) \frac{dk_x dk_y}{(2\pi)^2} \right] \frac{e^2}{h} = C \frac{e^2}{h} \quad (2.26)$$

The quantity within [...] is an integer, equal to the Chern number (C), quantifying the non-zero topological edge state within the Landau gap created by the separation of the bands [32]. $\Omega_z(k_x, k_y)$ denote z component of the Berry curvature. The quantization of the quantum Hall effect has been verified with the accuracy of $1/10^7$. This is possible because of the non-trivial topology of the electron wave functions, which cannot be perturbed easily.

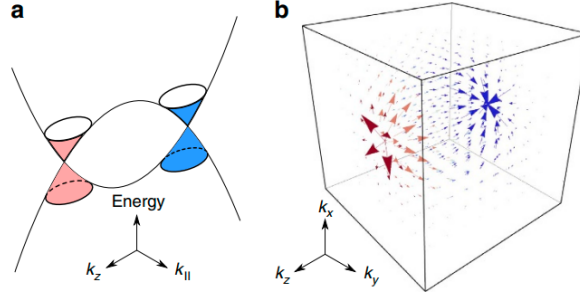


Figure 2.8: (Ref. [33]) Red and blue Dirac cones in (a) representing Weyl points of opposite chirality. (b) shows a pair of Weyl fermions in phase space. The red and blue show the flux of the Berry curvature from one monopole to another, illustrating the flux of the magnetic field between two monopoles.

2.5 Anomalous transport properties

As stated above, the presence of Berry curvature in solids is equivalent to the magnetic field in phase space. If the 'band crossing' host Weyl Fermions, each Weyl point acts as a sink or source of the Berry curvature, which is equivalent to the magnetic monopole in real space Fig. 2.8(a). The 'virtual' magnetic flux in \mathbf{k} space is illustrated in the Fig. 2.8(b).

2.5.1 Anomalous Hall effect

Hall resistance arises when an external magnetic field is applied. However, non-zero Hall resistivity can be observed even in the absence of a magnetic field. Such type of Hall resistance is known as the anomalous Hall effect. The factors leading to anomalous Hall signals can be intrinsic, and extrinsic as well.

2.5.1.1 Extrinsic contribution

Skew scattering: Originated by the asymmetric scattering of electrons due to the effective spin orbit coupling. This contribution is proportional to the lifetime of the Bloch electrons. Its contribution dominates only in very pure crystals. In this case, $\rho_H^{skew} = \sigma_H^{skew} \rho^2$ [34]. Where, ρ is the normal resistivity of the compound, σ_H^{skew} denotes the Hall conductivity due to the skew scattering.

Side jump scattering: This contribution comes as a result of the spin orbit coupling

between the electrons scattered from the impurities. The electrons are deflected in the opposite direction as they approach or leave the impurity. This contribution is independent of the transport lifetime [34].

Magnetization: Anomalous Hall effect can arise in magnetic materials because of the unequal population of the magnetic domains. Magnetization ($M(T, H)$) induced Hall resistivity is proportional to the magnetization of the sample ($\rho_H^M(T, H)$) $\propto M(T, H)$ [34]. So, if non-zero remanent magnetization is present in the compound, a corresponding anomalous Hall effect may also be observed.

2.5.1.2 Intrinsic contribution

In the case of 3D materials, the intrinsic anomalous Hall effect σ_{ij}^{Int} due to the Berry curvature can be formulated [35, 34] using the linear-response theory as:

$$\sigma_{xy}^{Int} = \frac{e^2}{\hbar} \sum_n \int_{BZ} \frac{d^3k}{(2\pi)^3} f(\epsilon_n(\mathbf{k})) \Omega_n(\mathbf{k}) \quad (2.27)$$

Where, $f(\epsilon_n(\mathbf{k}))$ is the Fermi-Dirac distribution function. The Berry curvature for n^{th} band ($\Omega_n(\mathbf{k})$) is defined as

$$\Omega_n(\mathbf{k}) = 2\text{Im} \sum_{m \neq n} \frac{\langle u_n(\mathbf{k}) | \partial_{\mathbf{k}_x} H(\mathbf{k}) | u_m(\mathbf{k}) \rangle \langle u_m(\mathbf{k}) | \partial_{\mathbf{k}_y} H(\mathbf{k}) | u_n(\mathbf{k}) \rangle}{(E_n(\mathbf{k}) - E_m(\mathbf{k}))^2} \quad (2.28)$$

The transformation of Berry curvature ($\Omega(\mathbf{k})$) under time-reversal (TR) and space-inversion (SI) symmetry is given by:

$$TR \Rightarrow \Omega(-\mathbf{k}) = -\Omega(\mathbf{k}) \quad (2.29)$$

$$SI \Rightarrow \Omega(-\mathbf{k}) = \Omega(\mathbf{k}) \quad (2.30)$$

These symmetry properties suggest that the integral over the BZ vanishes if time-reversal symmetry is present in the material. Therefore, to obtain the non-zero transverse conductivity originating from the non-trivial topology of the systems, the time reversal symmetry has to be broken. The integral of the Berry curvature can be calculated over a small gaussian surface around a Weyl point, which gives the Chern number (C) = ± 1 . Where + and - signifies whether the Weyl point acts as a source or sink of the Berry curvature.

Since the Weyl points also illustrate magnetic monopoles, the observation of non-zero Hall resistivity without any external field is expected in the Weyl semimetals

as well. Considering a simple model of a magnetic Weyl semimetal, with one pair of Weyl points near the Fermi surface, the magnitude of intrinsic Hall conductivity (σ_{xy}^{int}) can be determined by the separation of the Weyl points ($\Delta k_{W\pm}$) as [32, 36]

$$\sigma_{xy}^{int} = \frac{e^2}{h} \frac{\Delta k_{W\pm}}{2\pi} \quad (2.31)$$

It is intuitive to guess that to achieve large intrinsic Hall conductivity, Weyl points with opposite chirality have to be largely separated, which can be achieved by time reversal broken symmetry, or the application of the external magnetic field. In a few cases, the fictitious magnetic field induced by Berry curvature in Weyl semimetals is very large (up to 200 T in Mn_3Ge [37]) compared to external magnetic field. In that case, the external magnetic field has negligible effect on the separation of the Weyl points, and induced intrinsic Hall conductivity.

2.5.2 Chiral anomaly

One of the most intriguing properties of Weyl semimetal is the chiral anomaly effect. In particle physics, the chiral charge is a conserved quantity. However, in the case of solid state materials hosting Weyl Fermions, when an external magnetic field is applied in the direction of the electric field, the chiral charge is not conserved quantum mechanically, leading to the huge chiral current. This effect of non-conservation of the chiral current is known as the chiral anomaly effect, also known as Adler-Bell-Jackiw anomaly [38].

2.5.2.1 Longitudinal magneto-resistance

One of the primary pieces of evidence of the presence of chiral anomaly is a sharp decrease in magneto-resistance of the sample when the magnetic field is applied parallel to the direction of the electric current in the sample. The consequence of the magnetic field applied parallel to the electric field can be determined in a simple way using the dispersion relation. The dispersion relation corresponding to chiral Weyl points can be given as [41, 42]

$$E_n = v_F [\text{sign}(n)] \sqrt{(\hbar \mathbf{k} \cdot \mathbf{B})^2 + 2\hbar |n| e B} \quad (2.32)$$

Where, $n = 0, \pm 1, \pm 2, \dots$ denote Landau level, \pm correspond to the chirality of the Weyl cones. It can be noted that the $n = 0$ Landau level has linear dispersion with a

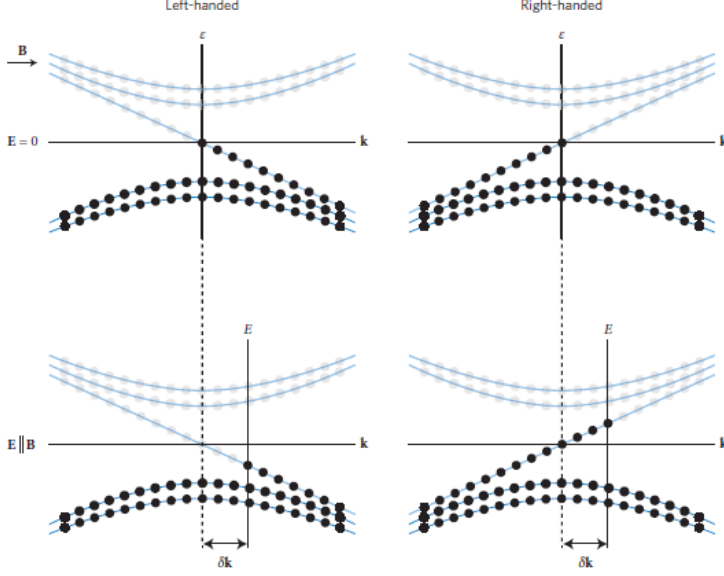


Figure 2.9: (Ref. [25]) Origin of the chiral anomaly. The dispersion of the lowest band is opposite for the Weyl points with \pm chirality. Top: figures show the equilibrium of left and right-handed Weyl points in the presence of the magnetic field and the absence of an electric field. Black and gray dots represent filled and empty states. Bottom: the same Weyl Fermions under the application of electric and magnetic field along the same direction, which results in the displacement of states by $\delta \mathbf{k}$ ($\propto -\mathbf{E}$) along the field direction. This creates an imbalance in the electronic states, leading to additional conductivity in the material.

slope determined by the chirality of the Weyl node. If the chemical potential is very small, at a very low temperature (quantum limit), only the lowest Landau level will contribute. So, in this case,

$$E_0 = v_F [\text{sign}(n)] (\hbar \mathbf{k} \cdot \mathbf{B}) \quad (2.33)$$

The chiral current density (j_χ) corresponding to zeroth Landau level has been derived by the Ref. [42], using the semiclassical approach ($\hbar \dot{\mathbf{k}} = -e\mathbf{E}$), as

$$\frac{\partial j_\chi}{\partial t} = -\chi \frac{e^3}{4\pi^2 \hbar^2} (\mathbf{E} \cdot \mathbf{B}) \quad (2.34)$$

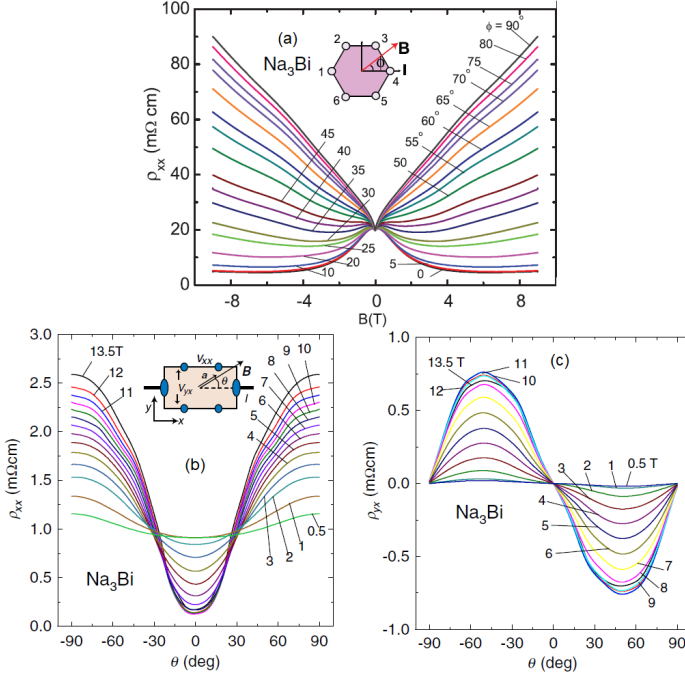


Figure 2.10: (Ref. [39, 40]) Chiral anomaly in Dirac semimetal - Na₃Bi. Na₃Bi becomes Weyl semimetal under the application of the external magnetic field, because of the broken TR symmetry. The Dirac cones split into Weyl cones in the same direction as the field is applied. When the magnetic field is applied parallel to the electric current, chiral anomaly-induced negative magneto-resistance (MR) is observed, as shown in (a), corresponding to the Na₃Bi Dirac semimetal. Angular MR and planar Hall effect for the Na₃Bi is shown in (b, c), respectively. Sample contacts and measurement setup for (b, c) are shown in the (b) inset.

This suggests additional current density in the presence of non zero $\mathbf{E} \cdot \mathbf{B}$. The above derivation is performed in the quantum regime limit ($n = 0$). However, a chiral anomaly not restricted to the quantum limit, charge pumping between chiral nodes has been expected to be in the semiclassical regime as well [43, 44]. The above equation can be further simplified and generalized, after which the field dependence of longitudinal magneto-conductivity (σ_{ii}) in type-I Weyl semimetal is given as [44, 45]:

$$\sigma_{ii} = \sigma_D + \frac{e^4 \tau_a}{4\pi^4 \hbar^4 \mu^2} B^2 \quad (2.35)$$

Where, the first term, σ_D , is the Drude conductivity, and the second term is the longitudinal magneto-conductivity (LMC) contribution due to the chiral anomaly. τ_a is the charge relaxation time due to the internode scattering of the electrons. μ is defined as the chemical potential relative to the Weyl points. The quadratic magnetic field dependence of the LMC is valid at a low magnetic field. However, at a high field (when the cyclotron frequency (ω_c) is much greater than intravalley scattering frequency), the field dependence of the LMC saturates [44]. The increase in conductivity, is experimentally observed in the form of decrease in longitudinal magneto-resistivity, as shown in the Fig. 2.10(a).

In contrast to the type-I Weyl semimetals, the Weyl points in type-II semimetals, are tilted towards a particular axis, which gives rise to linear magnetic field dependence of the LMC when measured along the tilt axis [46, 9, 27]. However, the LMC show quadratic magnetic field dependence (Eqn. 2.35) when it is measured along the axes, which are away from the tilt axis.

Since negative MR ($\rho(B)$) is observed as long as the magnetic field has a component along the electric current, clear angular dependence has been observed when the magnetic field is rotated, making an angle (θ) with respect to the electric current direction [1, 39, 40, 47]. As mentioned by the Refs. [43, 48], the angular dependence of MR should follow:

$$\rho^{-1}(B, \theta) - \rho^{-1}(B, 0) = \frac{1}{\rho_{\perp}} \frac{\chi \cos^2 \theta}{1 + \chi \sin^2 \theta} \quad (2.36)$$

Where, $\chi = (\rho_{\perp} - \rho_{\parallel})/\rho_{\parallel}$. It is interesting to note that in case $\chi \ll 1$, the above equation can be reduced to

$$\rho^{-1}(B, \theta) - \rho^{-1}(B, 0) = \frac{1}{\rho_{\perp}} (\chi \cos^2 \theta) \quad (2.37)$$

The presence of χ in angular MR is the key parameter to distinguish it from the conventional angular MR dependence. The increase in the magnitude of χ led to the sharp angular dependence of MR originating from the chiral anomaly effect. Angular narrowing plays an important role to distinguish MR contribution from the magnetization originated MR, which may also show Eqn. (2.37) type angular dependence in the case of magnetic materials [49]. For Weyl or Dirac semimetals, sharp angular dependence has been observed in some compounds experimentally [37, 50]. However, Eqn. (2.37) type behavior has also been observed in many Weyl semimetals [47, 40],

as shown in the Fig. 2.10(b).

2.5.2.2 Planar Hall effect

In addition to the giant negative longitudinal MR, the large planar Hall effect (PHE) has also been considered as a promising sign of the chiral anomaly effect in Weyl semimetals [43, 48]. Planar Hall effect is measured when transverse (Hall) voltage is measured with applied magnetic field within the sample plane. In normal metals, transverse voltage is expected to be zero as long as magnetic field lies in the sample plane. However, in Weyl semimetals, non-zero Hall voltage is obtained even when magnetic field lies in the sample plane. The PHE shows oscillation when magnetic field is rotated within the sample plane and follows [43]

$$\rho^{PHE} = -(\rho_{\perp} - \rho_{\parallel}) \sin \theta \cos \theta = \frac{(\rho_{\parallel} - \rho_{\perp})}{2} \sin 2\theta \quad (2.38)$$

Here, as mentioned previously, θ denotes the angle between magnetic field and the electric current direction. It can be noted that the magnitude of PHE is intrinsically determined by the relative magnitude of the negative longitudinal MR ($\rho_{\parallel} - \rho_{\perp}$), which is expected because the PHE is a consequence of the angular dependence of the (anisotropic) MR [48]. An example of the PHE in Na₃Bi (Weyl semimetal under magnetic field) is shown in the Fig. 2.10(c).

2.6 Magnetic Weyl semimetals - Mn₃X (X = Sn, Ge)

Most of well known Weyl semimetals where the Fermi arc is observed are non-magnetic semimetals, where broken SI symmetry play important role in the emergence of Weyl points. However, it has been predicted that the Hexagonal phase of Mn₃Ge and Mn₃Sn compounds with broken TR symmetry exhibit Weyl points [51]. Interestingly, the location of Weyl points is close to the Fermi surface, which led to the great interest in these magnetic Weyl semimetals.

Mn₃X forms a Hexagonal lattice structure with Mn atoms forming a Kagome-type lattice, as shown in the Fig. 2.11(a). Both the compounds, Mn₃Ge and Mn₃Sn, are antiferromagnetic below 365 K, and 420 K, respectively, with Mn moments oriented in an inverse triangular fashion within the *a-b* plane [52, 53]. The ground state magnetic structure of Mn₃X is chiral in nature. The magnetic chirality can be calculated as $\chi = \hat{z} \cdot [\mathbf{S}_i \times \mathbf{S}_j]$, where, *i* and *j* spins move clockwise. This suggests that the magnetic

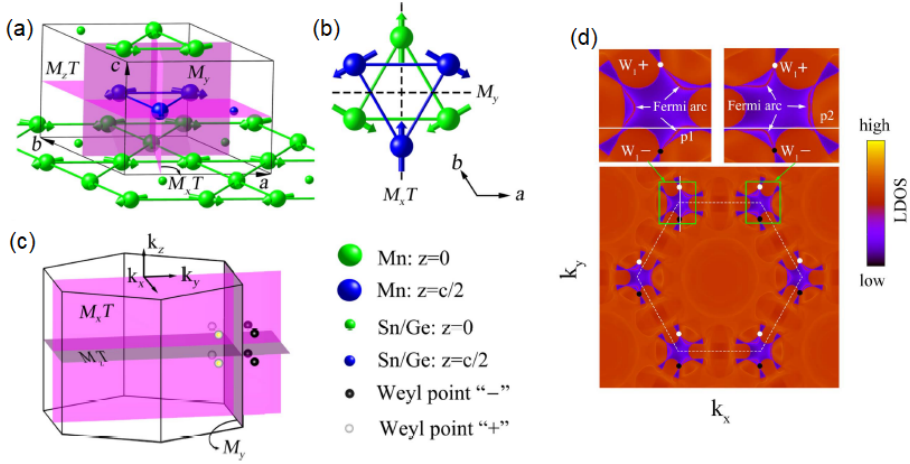


Figure 2.11: (Ref. [51]) Crystal structure of Mn_3X and its symmetry planes are shown in (a). The mirror reflection in x , y , z planes and time reversal symmetry can be denoted by M_x , M_y , M_z and T , respectively. Magnetic structure of Mn_3Ge in $a-b$ plane is shown in (b). The symmetry axes are labeled and shown as dotted lines. The symmetry planes and location of Weyl points are shown in the 3D lattice structure in (c). The location of Weyl points and corresponding Fermi arcs are shown in (d).

structure shown in Fig. 2.11(a) has positive chirality because spins rotate counter-clockwise, as we move in a clockwise direction [54]. The crystal structure, symmetry planes, and magnetic structure are shown in Fig. 2.11. It can be interpreted from the Fig. 2.11(a, b), that layered Mn structures can be transformed into each other by mirror reflection (M_y), followed by a translation (τ) of the lattice by $c/2$ towards the z axis. In total, Mn_3Ge lattice possess M_xT , M_zT , $\{M_y|\tau \rightarrow \frac{c}{2}\}$ symmetries, which suggest lack of TR symmetry (denoted by T) in $y-z$ plane [51]. Therefore, Mn_3X is allowed to host Weyl points. The presence of Weyl points and Fermi arc in Mn_3X has been theoretically observed by the Ref. [51], as shown in the Fig. 2.11(d). Interestingly, the Weyl points were observed to be tilted, which predicts a typical type-II Weyl semimetallic behavior of Mn_3X .

The magnetic structure of Mn_3Ge remains the same below Néel temperature (365 K), down to the lowest measured temperature (2 K), which is not the case for Mn_3Sn . Therefore, the Weyl semimetallic nature of Mn_3Ge is expected in these large temperature regimes. This gives us a vast temperature regime to explore the dynamics of Weyl points. As expected, anomalous Hall effect, anomalous Nernst effect, and anomalous

magneto-optical Kerr effect have been already observed in Mn_3Ge , down to the 2 K [37, 55, 56, 57]. This strongly suggests the presence of an intrinsic magnetic field originated by Weyl points in Mn_3Ge . However, a clear signature of chiral anomaly has not been reported yet. Therefore, we have explored the electrical transport properties of the Mn_3Ge (chapter 5) to determine the presence of a chiral anomaly in this magnetic Weyl semimetal. Further, Fe doped Mn_3Ge compounds were also studied to explore the characteristics of Weyl points with respect to the impurity, magnetization, and lattice parameters.

2.7 Scattering

Scattering is a process in which a particle or wave deflects from its original path upon the interaction with matter or any form of potential. In the case of elastic scattering, the energy of the incident and diffracted wave/particle remains the same. Scattering methods can be used to determine the microscopic properties of the materials. In this thesis, elastic scattering methods have been used extensively to determine the magnetic and structural parameters of the compounds.

2.7.1 Scattering cross section

Scattering experiments in materials can be analyzed in the far-field approximation or *Fraunhofer approximation* because the distance between the location of the sample and detector is much larger compared to the dimension of the sample. Under this approximation, incident and scattered waves, with wavelength λ and λ' , respectively, are assumed as plane waves propagating along \mathbf{k} and \mathbf{k}' directions, respectively. Where, \mathbf{k} and \mathbf{k}' denote incident and scattered wave vector, respectively, as shown in the Fig. 2.12. The difference between scattered and incident wavevector

$$\mathbf{k}' - \mathbf{k} = \Delta\mathbf{k} = \mathbf{Q} \quad (2.39)$$

Where, \mathbf{k} ($= 2\pi\hat{\mathbf{n}}/\lambda$), and \mathbf{k}' ($= 2\pi\hat{\mathbf{n}}'/\lambda'$) are the incident and diffracted wave vectors, respectively. In the case of elastic scattering, $|\mathbf{k}'| = |\mathbf{k}|$, because λ remains unchanged. The quantity \mathbf{Q} is known as the *scattering vector*.

In a scattering experiment, the intensity distribution is measured as a function of the scattering wave vector (\mathbf{Q}). The strength of the scattered intensity is determined by the scattering cross section (σ) of the scatterer, and the geometry of the experi-

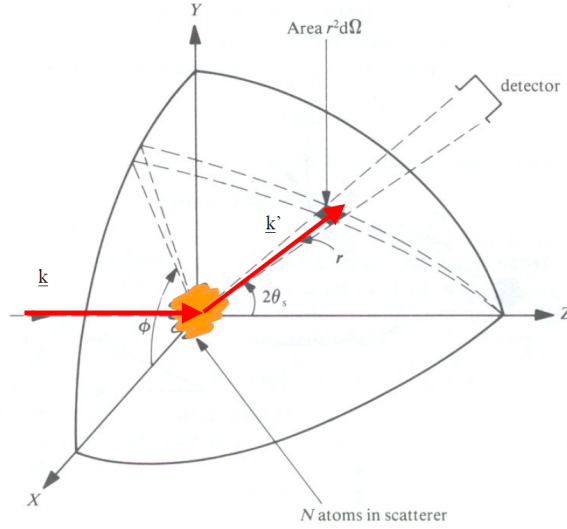


Figure 2.12: (Ref. [58]) Scattering geometry for the derivation of diffraction cross section. Here, \mathbf{k}, \mathbf{k}' denote the incident and scattered wave vector. ϕ is the arbitrary azimuthal angle corresponding to the scattering cross section. $2\theta_s$ denotes the scattering angle with respect to the incident wave vector.

mental setup. Scattering cross section can be determined for an experimental setup having geometry shown in the Fig. 2.12. Generally, *scattering intensity* ($I(\Omega)$) is determined by the *differential cross section*, defined as

$$\boxed{\frac{d\sigma}{d\Omega} = \int_0^\infty \frac{d^2\sigma}{d\Omega dE'} dE'} \quad (2.40)$$

Where, E is the energy of the incoming wave. Integrating the differential cross section over 4π solid angle gives *total scattering cross section* as

$$\sigma = \int_0^{4\pi} \left(\frac{d\sigma}{d\Omega} \right) d\Omega \quad (2.41)$$

Which is also equal to the total scattering probability within the 4π solid angle. Interestingly, the σ is independent of the energy.

2.7.2 Basics of diffraction

The interaction between wave and matter is determined by the scattering potential $V(\mathbf{r})$. The interaction can be described quantum mechanically using the Schrödinger equation as mentioned in the Refs. [58, 59, 60]

$$H\psi = \left(-\frac{\hbar^2}{2m}\nabla^2 + V(\mathbf{r}) \right) \psi = i\hbar \frac{\partial}{\partial t} \psi \quad (2.42)$$

Where, m is the rest mass of the neutrons, in the case of neutron scattering. $V = 0$ outside the sample dimension. The above equation can be solved using the method of separation of spatial and temporal variables as

$$\psi(\mathbf{r}, t) = \zeta(\mathbf{r}) e^{-iEt/\hbar} \quad (2.43)$$

In the case of scattering under the Fraunhofer approximation (source and detector

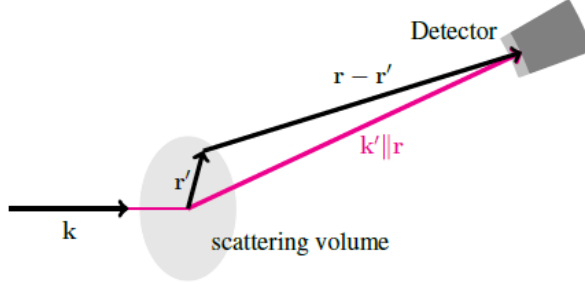


Figure 2.13: (Ref. [59]) Scattering geometry for far field condition: $|\mathbf{r} - \mathbf{r}'| \approx |\mathbf{r}|$

are far from the sample), the solution for $\zeta(\mathbf{r})$ (at a distance far from the scatterer) can be written as sum of incoming wave, with wave vector \mathbf{k} , ($e^{i\mathbf{k}\cdot\mathbf{r}}$), and scattered spherical wave. So

$$\zeta(\mathbf{r}) \approx e^{i\mathbf{k}\cdot\mathbf{r}} + \left[\frac{e^{ikr}}{r} f_{\mathbf{k}}(\theta, \phi) \right] \quad (2.44)$$

Here, $f_{\mathbf{k}}(\theta, \phi)$ denotes the scattering amplitude, which depend on the scattering geometry and scattering potential $V(\mathbf{r})$. The solution for $f_{\mathbf{k}}(\theta, \phi)$ can be obtained approximately using the Green's function $G(\mathbf{r}, \mathbf{r}')$, which is the solution corresponding to the following equation

$$\left(\frac{\hbar^2}{2m}\nabla^2 + E \right) G(\mathbf{r}, \mathbf{r}') = \delta(\mathbf{r} - \mathbf{r}') \quad (2.45)$$

$$G(\mathbf{r}, \mathbf{r}') = \frac{e^{ik|\mathbf{r}-\mathbf{r}'|}}{4\pi|\mathbf{r}-\mathbf{r}'|} \quad (2.46)$$

Where, $|\mathbf{r}-\mathbf{r}'|$ denote the magnitude of the position of detector from the source, as shown in the Fig. 2.13. $E (= \frac{\hbar^2 k^2}{2m})$ is the energy of the incident plane wave. Using Eqns. (2.42, 2.43), the Schrödinger equation can be simplified in terms of $\zeta(\mathbf{r})$ as

$$\left(\frac{\hbar^2}{2m} \nabla^2 + E \right) \zeta(\mathbf{r}) = V(\mathbf{r})\zeta(\mathbf{r}) \quad (2.47)$$

which can be solved for any $V(\mathbf{r}')$ in the form of *Lippmann - Schwinger equation* given as

$$\zeta(\mathbf{r}) \approx \zeta_0(\mathbf{r}) + \frac{2m}{\hbar^2} \int_{vol.} G(\mathbf{r}, \mathbf{r}') V(\mathbf{r}') \zeta(\mathbf{r}') d\mathbf{r}' \quad (2.48)$$

Where, $\zeta_0(\mathbf{r}) = e^{i\mathbf{k}\cdot\mathbf{r}}$ is the unscattered plane wave solution. *vol.* denotes the integration to be performed throughout the volume of sample. Using $\mathbf{R} = \mathbf{r} - \mathbf{r}' \approx \mathbf{r}$ (far field approximation), and $\mathbf{Q} = \mathbf{k}' - \mathbf{k}$, the Green's function can be approximated, which modifies the Eqn. (2.48) to

$$\zeta(\mathbf{r}) \approx \underbrace{e^{i\mathbf{k}\cdot\mathbf{r}}}_{incoming} + \underbrace{\frac{2m}{\hbar^2} \frac{e^{i\mathbf{k}\cdot\mathbf{r}}}{4\pi R} \int_{vol.} e^{i\mathbf{Q}\cdot\mathbf{r}'} V(\mathbf{r}') \zeta(\mathbf{r}') d\mathbf{r}'}_{=F(\mathbf{Q})_{scatt.}} \quad (2.49)$$

Eqn. (2.49) is the final result, which describes the spatial variation of the scattered wave in the direction of \mathbf{k}' . $F(\mathbf{Q})_{scatt.}$ is known as the scattering amplitude. The quantity that is measured during the experiment is intensity (I), which is defined as

$$I(\mathbf{Q}) \propto \frac{d\sigma}{d\Omega} = |F(\mathbf{Q})|^2 = \left| \frac{2m}{\hbar^2} \frac{e^{i\mathbf{k}\cdot\mathbf{r}}}{4\pi R} \int_{vol.} e^{i\mathbf{Q}\cdot\mathbf{r}'} V(\mathbf{r}') \zeta(\mathbf{r}') d\mathbf{r}' \right|^2 = |\mathcal{F}[V(\mathbf{r})]|^2 \quad (2.50)$$

Here, $\mathcal{F}[V(\mathbf{r})]$ denotes the Fourier transformation of the scattering potential ($V(\mathbf{r})$). Therefore, it can be concluded that the scattering intensity is the square of the magnitude of Fourier transformation of $V(\mathbf{r})$. It is important to notice that the phase ($e^{i\mathbf{k}\cdot\mathbf{r}}$) is lost in the intensity, which is also known as the *phase problem*.

2.7.3 Diffraction in periodic lattice

2.7.3.1 Bragg's law, Ewald sphere, and Laue condition

When a coherent wave with wavelength λ hits on the periodic lattice structure, the diffracted wave forms constructive interference patterns at a certain grazing angle (θ) determined by the separation of the lattice planes perpendicular to the scattering vector (\mathbf{Q}). The diffraction pattern follows the *Bragg's law*

$$2d_{hkl} \sin \theta = n\lambda \quad (2.51)$$

Where, d_{hkl} is the separation between two hkl planes, θ is the grazing angle of the incident beam as shown in the Fig. 2.14(a). In the case of Hexagonal lattice with lattice constants a and c , the distance between two consecutive planes, d_{hkl} , is defined as:

$$d_{hkl} = \left[\sqrt{\frac{4}{3} \frac{h^2 + hk + k^2}{a^2}} + \left(\frac{l}{c} \right)^2 \right]^{-1} \quad (2.52)$$

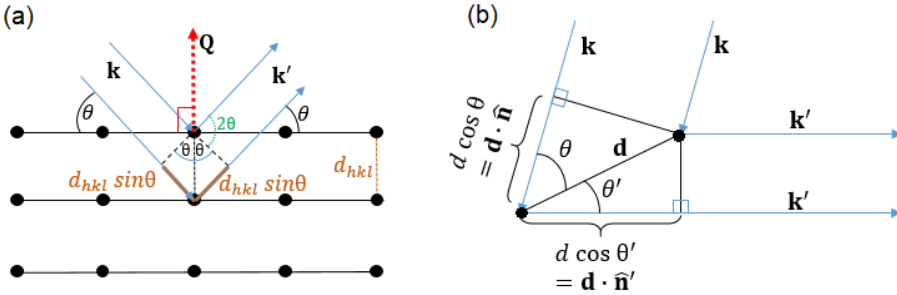


Figure 2.14: Illustration of the interplanar path difference observed by the incident wave is shown in different ways in (a, b). \mathbf{k} and \mathbf{k}' denote incident and diffracted wave.

The condition for the diffraction can be approached differently, as shown in the Fig. 2.14(b), where each atom can be considered a scatterer. In this case, the path difference created by two scatterers (with distance \mathbf{d}) has to be integral multiple of the λ to observe a constructive interference. So,

$$d \cos \theta + d \cos \theta' = \mathbf{d} \cdot (\hat{\mathbf{n}} - \hat{\mathbf{n}}') = p\lambda \quad (2.53)$$

Where, p is an integer. $\hat{\mathbf{n}}$ and $\hat{\mathbf{n}}'$ are related with \mathbf{k} , \mathbf{k}' as $\mathbf{k} = 2\pi\hat{\mathbf{n}}/\lambda$, $\mathbf{k}' = 2\pi\hat{\mathbf{n}}'/\lambda$. For constructive interference, the change in wave vector, $\mathbf{k}' - \mathbf{k} = \Delta\mathbf{k} = \mathbf{K}$. Where \mathbf{K} is the periodic reciprocal lattice vector. The condition $\Delta\mathbf{k} = \mathbf{K}$ is known as the *Laue condition* for the diffraction.

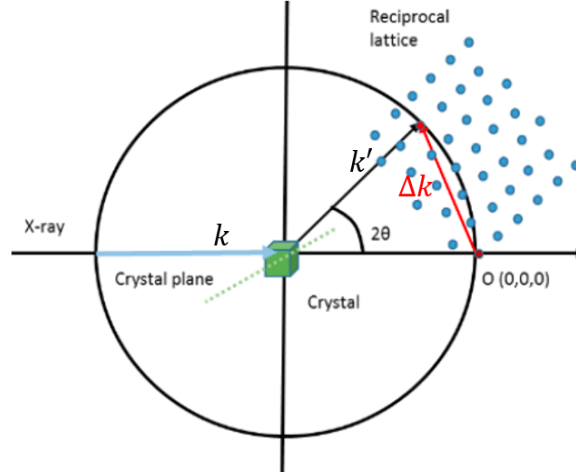


Figure 2.15: (Ref. [61]) Ewald construction in reciprocal space for elastic scattering.

In the case of elastic scattering, the scattering vector, $\mathbf{Q} = \mathbf{K}$. The scattering vector (\mathbf{Q}) can be defined in real measurable parameters as

$$|\mathbf{Q}| = \frac{4\pi \sin \theta}{\lambda} \quad (2.54)$$

Bragg's law can be alternatively understood using the Ewald sphere construction in reciprocal space, as shown in the Fig. 2.15. The Ewald sphere is a hypothetical spherical surface with a radius of \mathbf{k} , which lies on a reciprocal lattice point. In the case of elastic scattering, \mathbf{k}' (scattered wave vector) lies on the Ewald sphere as well, because $|\mathbf{k}'| = |\mathbf{k}|$. As θ varies, the constructive interference forms when \mathbf{k}' also lies on a different reciprocal lattice vector, as shown in the Fig. 2.15. This can be justified because if \mathbf{k} and \mathbf{k}' lies on the reciprocal lattice point, $\Delta\mathbf{k} = \mathbf{k}' - \mathbf{k} = \mathbf{K}$. Where, \mathbf{K} is the distance between two reciprocal lattice points. Therefore, the diffraction peak is observed at 2θ which follows the Laue condition: $\Delta\mathbf{k} = \mathbf{K}$.

2.7.3.2 Diffraction from (non - magnetic) crystal

The condition for constructive interference can be determined by Bragg's law as explained above. However, the scattering intensity depends on the position of the atom, thermal vibration of atom, and scattering form factor of the atom ($f_{scatt.}$) located at lattice points. The structure factor ($F(Q)_{crys.}$) for a crystal is given as

$$F(Q)_{crys.} = \sum_j \underbrace{f_j(Q)}_{f_{scatt.}} e^{\mathbf{Q} \cdot \mathbf{r}_j} e^{W_j(T, Q)} \quad (2.55)$$

Where r_j is the location of atoms relative to any particular lattice point. The atomic scattering factor, $f_{scatt.}$, is the magnitude of (X-ray or neutron) *scattering amplitude* corresponding to an isolated atom. $f_{scatt.}$ is unique to the particular element, and depends on the source and types of scattering. As we will see below, in the case of X-ray, nuclear, and magnetic scattering, the $f_{scatt.}$ is replaced by the atomic form factor (f_a), neutron form factor (or scattering length) (b), and magnetic form factor (f_m), respectively. The strength of different types of $f_{scatt.}$, changes with $|Q|$ ($= \frac{4\pi \sin \theta}{\lambda}$), as shown in the Fig. 2.16. The term e^{W_j} is the Debye - Waller (DW) factor given as

$$e^{W_j(T, Q)} = e^{-Q^2 \frac{\langle u(T)^2 \rangle}{3}} \quad (2.56)$$

The DW factor is mainly dependent on the $\langle u(T) \rangle$, which is defined as the average displacement of the j^{th} atom, relative to the equilibrium position, due to the thermal vibrations. It is obvious to infer that with an increase in the temperature, $\langle u^2 \rangle$ increases, leading to the smear out the scattered intensity, which appears to be diffused, far from the Bragg positions.

2.7.4 X-ray scattering

The scattering techniques using the X-ray are widely available, and very sensitive techniques to probe the structural parameters of the crystals. For scattering purposes, the wavelength of the incident wave should be comparable to the lattice constants. Therefore, the typical wavelength of X-ray that can be used for crystal diffraction experiments is order of ~ 0.1 nm. The corresponding momentum of X-rays is so small that it scatters from the electron cloud, without interacting with the nucleus. Therefore, in the case of X-ray scattering, $f_{scatt.}$ is replaced by the *atomic form factor* (f_a), also known as *X-ray form factor*. f_a corresponding to an atom depends on the atomic

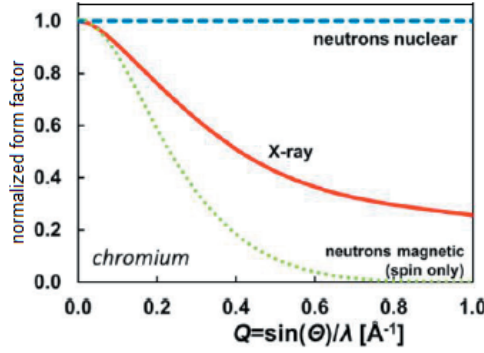


Figure 2.16: (Ref. [58]) Normalized scattering form factor of Cr corresponding to the different sources of scattering is shown with respect to the change in scattering vector (or scattering angle (2θ)).

electron density ($\rho_e(r)$) around the nucleus and is defined as

$$f_a(Q) = \int \rho_e(\mathbf{r}) e^{i\mathbf{Q} \cdot \mathbf{r}_j} d\mathbf{r} = \mathcal{F}[\rho_e(\mathbf{r})] \quad (2.57)$$

$f_a(Q)$ decreases with an increase in scattering angle (2θ) as shown in the Fig. 2.16. It is proportional to the number of electrons, which makes it difficult to differentiate between atoms with the nearly same number of electrons. Other than this, light elements are not ‘visible’ for X-ray if a heavy element is present in the crystal.

Since the typically available X-rays flux density is very high ($\sim 10^{13}$ photons/(mm²-sec.)), they provide very high resolution diffraction patterns during the experiments. X-ray diffraction is preferably used for the determination of the details of nuclear parameters (like bond angle, bond length, lattice parameters) under various conditions, like pressure, and temperature.

Also, since the magnetic form factor for X-ray is very small compared to the charged form factor, the magnetic information of the crystal is, usually, not possible to determine using normal X-ray diffraction experiments.

2.7.5 Neutron scattering

Neutron scattering is a very sensitive and non-destructive tool to determine the microscopic nature of the crystals. It has several pros and cons as follows.

Pros: Neutron with wavelength ~ 0.1 nm has an energy of nearly 100 meV, which

is large enough to penetrate the electron cloud and interact with the nucleus of the atom. Therefore, the scattering factor of an element for neutrons depends on the details of the nuclear structure, so the neutron cross section for atoms varies in a non-systematic fashion, which can be helpful in several cases. For example, unlike X-rays, neutron cross sections for Mn and Fe are very different in magnitude. Therefore, Mn and Fe can be easily differentiated using neutron diffraction experiments, which is very difficult using X-ray diffraction. Also, the neutrons are spin- $\frac{1}{2}$ particles, which makes neutron scattering a strong technique to probe the magnetic information of the sample. We have used neutron diffraction techniques extensively to resolve the fraction of Fe and Mn in the doped sample and determine the ground state magnetic structure of the parent and doped samples.

Cons: The (monochromatic) neutron flux density available for the neutron diffraction experiments is $\sim 10^4$ neutron/(mm²-sec.), which is 10^9 time smaller than X-ray flux density [59]. Therefore, neutron does not provide high resolution information of the lattice parameters, compared to X-ray diffraction. Also, because of low flux density, a large counting time of a large amount of sample is required during the neutron diffraction experiments.

Neutron scattering involves nuclear and magnetic scattering. Thankfully, both the contributions can be analyzed, almost, independently.

2.7.5.1 Nuclear scattering

Neutrons are heavy particles, which interact with the nuclei via strong nuclear force. Therefore, nuclear scattering is the major component of the scattered intensity. Since the wavelength of neutrons is orders of magnitude larger than the nuclear dimension, the nuclei can be treated as a point object, leading to the isotropic scattering independent of the scattering angle (2θ), as shown in the Fig. 2.16. Therefore, interaction potential between neutron and nucleus can be written in form of the *Fermi-pseudopotential* as

$$V(\mathbf{r}, \mathbf{r}_j) = \frac{2\pi\hbar^2}{m_n} [b_j \delta(\mathbf{r} - \mathbf{r}_j)] \quad (2.58)$$

Where, \mathbf{r} is the neutron coordinate, \mathbf{r}_j is the coordinate of the nucleus, and m_n is the mass of the neutron. The term b defined above is of phenomenal importance, describing the extent of interaction between nucleus and neutron and is known as the *neutron scattering length*. Since the nucleus is a point like a sphere, its nature is considered to be isotropic. Therefore, the total cross section can be simply written as

$\sigma = 4\pi b^2$. b depends on the nuclear spin parameters, so it can be different for different isotopes corresponding to the same element. Therefore, neutron diffraction can be a great tool to probe the different isotopes as well, which is not possible using X-ray diffraction.

The structure factor remains the same form as mentioned in the Eqn. (2.55). However, in the case of neutrons, it is *neutron scattering length* or *neutron cross-section* (b) that determines the scattering intensity. Therefore, the structure factor (Eqn. (2.55)) corresponding to the nuclear scattering can be written as

$$F(\mathbf{Q})_{crys.} = \sum_j b_j e^{i\mathbf{Q}\cdot\mathbf{r}_j} e^{W_j(T, \mathbf{Q})} \quad (2.59)$$

Where W denotes the Debye-Waller factor as described above. Since b can be significantly different for different isotopes, it gives rise to the *coherent* and *incoherent* scattering. The natural abundance of different isotopes can be very different, and nuclear spin also orients randomly in the absence of an external magnetic field. Therefore, while calculating the cross section for the neutron scattering these factors have to be averaged [58]. The averaged differential cross section can be defined as

$$\begin{aligned} \frac{d\sigma}{d\Omega} &= \left\langle \sum_j b_j e^{i\mathbf{Q}\cdot\mathbf{r}_j} \sum_{j'} b_{j'}^* e^{-i\mathbf{Q}\cdot\mathbf{r}_{j'}} \right\rangle = \sum_{j,j'} \langle b_j b_{j'} \rangle^* e^{i\mathbf{Q}\cdot(\mathbf{r}_j - \mathbf{r}_{j'})} \\ &= \underbrace{\langle b \rangle^2 \left| \sum_j e^{i\mathbf{Q}\cdot\mathbf{r}_j} \right|^2}_{coherent} + \underbrace{N \langle (b - \langle b \rangle)^2 \rangle}_{incoherent} \end{aligned} \quad (2.60)$$

As expected, the first term having phase information is square of the amplitude of $F(\mathbf{Q})$, without the DW factor. This term is responsible for the interference during the scattering, therefore known as *coherent scattering*. The effective scattering length determining the coherent scattering is the average scattering length of all the isotopes present in the sample. The second term in the Eqn. (2.60) contains the mean square scattering length for all the N atoms present in the sample, without any phase. This term simply suggests the addition of scattered neutron without any phase information. Therefore, it is known as a *incoherent scattering* contribution. The incoherent scattering corresponding to each atom is simply added, therefore, it is simply proportional to N (number of atoms), and leads to the isotropic background throughout the measured range of 2θ .

During the neutron diffraction, generally, we can neglect the incoherent contribu-

tion, and focus on the coherent contribution. The differential cross section corresponding to the coherent nuclear scattering is given as

$$\left. \frac{d\sigma}{d\Omega} \right|_{nuc.} \approx \langle b \rangle^2 \left| \sum_j e^{i\mathbf{Q}\cdot\mathbf{r}} \right|^2 \quad (2.61)$$

2.7.5.2 Magnetic scattering

Apart from nuclear scattering, magnetic scattering is also very useful in neutron diffraction experiments. It leads to the determination of the magnetic properties of the crystal to the atomic level. Since the neutrons have a magnetic moment, it interacts with unpaired electron spin and carries the information to the scattering pattern. During the scattering process, the magnetic dipole moment of the neutron interacts with the magnetic field of the unpaired electron, and orbital angular momentum.

The net magnetic field due to electron (\mathbf{B}) is the sum of the magnetic field due to its spin (\mathbf{B}_{spin}), and orbital angular momentum ($\mathbf{B}_{orbital}$). The interaction between magnetic dipole moment of neutron and net magnetic field due to electron is given as [58]

$$\mathcal{U}_m(\mathbf{r}) = -(\boldsymbol{\mu}_n) \cdot \mathbf{B}; \boldsymbol{\mu}_n = -(\gamma_n \mu_N \boldsymbol{\sigma}) \quad (2.62)$$

Where, μ_n is the magnetic moment of neutron. γ_n is the gyromagnetic ratio of neutron ($= -1.913$), and $\boldsymbol{\sigma}$ is the spin operator. The quantity μ_N is the nuclear magneton defined as $\frac{e\hbar}{2m_p} = 5.05 \times 10^{-27}$ J/T. The magnetic scattering depends on the *magnetic cross section*, defined as [58]

$$\left. \frac{d\sigma}{d\Omega} \right|_{mag.} = \left(\frac{m_n}{2\pi\hbar^2} \right)^2 |\langle \mathbf{k}' \sigma'_z | \mathcal{U}_m | \mathbf{k} \sigma_z \rangle|^2 \quad (2.63)$$

It can be further simplified in the case of elastic scattering. Without loss of the generality, consider the z axis to be the quantization axis. The net magnetic field in the sample, $\mathbf{B} = \mathbf{B}_{spin} + \mathbf{B}_{orbital}$. Since \mathbf{B}_{spin} is related with the magnetization (\mathbf{M}) of the sample, the above equation can be simplified in terms of the magnetization in \mathbf{k} space ($\mathbf{M}(\mathbf{Q})$), which can be obtained by the Fourier transformation of $\mathbf{M}(\mathbf{r})$ as

$$\mathbf{M}(\mathbf{Q}) = \int \mathbf{M}(\mathbf{r}) e^{i\mathbf{Q}\cdot\mathbf{r}} d\mathbf{r} \quad (2.64)$$

Using the definition of interaction potential (\mathcal{U}) defined above, magnetic differential

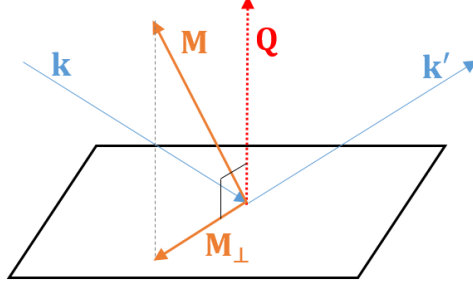


Figure 2.17: Illustration of the magnetic scattering where only the magnetization component perpendicular to the \mathbf{Q} is relevant. \mathbf{M}_\perp lies in the plane defined by $\mathbf{Q} - \mathbf{M}$;

cross section can be simplified as

$$\left. \frac{d\sigma}{d\Omega} \right|_{mag} = (\gamma_n r_0)^2 \left| -\frac{1}{2\mu_B} \underbrace{\langle \sigma'_z | \boldsymbol{\sigma} \cdot \mathbf{M}_\perp(\mathbf{Q}) | \sigma_z \rangle}_{mag. \text{ scattering amplitude}} \right|^2 \quad (2.65)$$

Where, r_0 is the Bohr's radius. \mathbf{k} and \mathbf{k}' are wave vectors corresponding to the incident and scattered neutrons, respectively. Similarly, σ_z and σ'_z denote the projection of spin moment to the quantization axis (z axis) before and after scattering, respectively. The quantity $\mathbf{M}_\perp(\mathbf{Q})$ is the magnetization component perpendicular to the scattering vector (Fig. 2.17), and defined as

$$\mathbf{M}_\perp(\mathbf{Q}) = \hat{\mathbf{e}}_Q \times \mathbf{M}(\mathbf{Q}) \times \hat{\mathbf{e}}_Q \quad (2.66)$$

Where, $\hat{\mathbf{e}}_Q = \frac{\mathbf{Q}}{|\mathbf{Q}|}$. It can be noted that the neutrons 'see' only the component of the magnetization *perpendicular* to the \mathbf{Q} . Therefore, only $\mathbf{M}_\perp(\mathbf{Q})$ contributes to the magnetic scattering, as illustrated in the Fig. 2.17.

In the case of d orbital elements, usually, orbital angular momentum (L) is quenched, so spins remain the sole source of the magnetic scattering contribution, which results in $g = 2$. Also, unlike nuclear scattering, magnetic scattering is the result of the interaction of neutrons with electron cloud. Therefore, similar to the atomic form factor in the case of X-ray scattering, the magnetic form factor also plays a fundamental role in magnetic scattering [58]. The magnetic structure factor is given as

$$\mathbf{M}(\mathbf{Q}) = -2\mu_B f_m(\mathbf{Q}) \sum_j e^{i\mathbf{Q} \cdot \mathbf{R}_j} \cdot \mathbf{S}_j \quad (2.67)$$

Where, \mathbf{R}_i denote the position of nucleus of i^{th} atom, \mathbf{S}_j denote the magnetic spin for j^{th} atom. $f_m(\mathbf{Q})$ denote the *magnetic form factor*, which can be defined relative to the spin density ($\rho_s(\mathbf{r})$) as

$$f_m(\mathbf{Q}) = \int_{Atom} \rho_s(\mathbf{r}) e^{i\mathbf{Q}\cdot\mathbf{r}} d\mathbf{r} = \mathcal{F}[\rho_s(\mathbf{r})] \quad (2.68)$$

Using Eqns. (2.65, 2.67, 2.68), magnetic differential cross section can be simplified as

$$\left. \frac{d\sigma}{d\Omega} \right|_{mag} = (\gamma_n r_0)^2 \left| f_m(\mathbf{Q}) \sum_j \langle \mathbf{S}_{j\perp} \rangle e^{i\mathbf{Q}\cdot\mathbf{R}_j} \right|^2 \quad (2.69)$$

Here, $\langle \mathbf{S}_{j\perp} \rangle$ symbolizes the expectation value of the perpendicular spin moment (\mathbf{S}_\perp) for j^{th} atom. The magnetic scattering is contributed by the unpaired electrons in the outer shell, in contrast to X-ray scattering where all the electrons contribute. Therefore, the magnetic form factor decreases with scattering angle (2θ) much faster, in comparison with the X-ray form factor, as shown in the Fig. 2.16.

In the case of Neutron diffraction, magnetic and nuclear scattering are present together. The total intensity of the scattered neutrons is determined by the combination of to nuclear scattering factor ($N(\mathbf{Q})$) and magnetic scattering factor ($\boldsymbol{\sigma} \cdot \mathbf{M}_\perp(\mathbf{Q})$). Therefore single differential cross section corresponding to the elastic neutron scattering can be given as

$$\left. \frac{d\sigma}{d\Omega} \right|_{neutron} = |N(\mathbf{Q}) + \boldsymbol{\sigma} \cdot \mathbf{M}_\perp(\mathbf{Q})|^2 \quad (2.70)$$

2.7.5.3 Polarized neutron scattering

As mentioned in the Eqn. (2.65), the magnetic scattering cross section is given as

$$\left. \frac{d\sigma}{d\Omega} \right|_{mag} \propto |\langle \sigma'_z | \boldsymbol{\sigma} \cdot \mathbf{M}_\perp(\mathbf{Q}) | \sigma_z \rangle|^2 \quad (2.71)$$

The term $\boldsymbol{\sigma} \cdot \mathbf{M}_\perp(\mathbf{Q})$ makes the neutron scattering technique very rich to determine the precise magnetic structure of the sample. Polarized neutron scattering experiment can be performed using spherical neutron polarimetry technique where incident and scattered polarization are measured. The magnetization of the sample changes the incident polarized neutron via the polarization tensor - \mathcal{P} . The relation

between polarization of the scattered neutron beam (\mathbf{P}') and incident polarization (\mathbf{P}) can be given as [62, 63, 64]

$$\mathbf{P}' = \mathcal{P}\mathbf{P} + \mathbf{P}'' \quad (2.72)$$

Which can be expanded in components as $P'_i = \mathcal{P}_{ij}P_j + P''_i$. Each term in the Eqn. (2.72) is defined as,

$$\mathbf{P}'' = \begin{bmatrix} -J_{yz}/I \\ R_{ny}/I \\ R_{nz}/I \end{bmatrix}$$

$$\mathcal{P} = \begin{bmatrix} (N^2 - M^2)/I_x & -J_{nz}/I_x & J_{ny}/I_x \\ J_{nz}/I_y & (N^2 - M^2 + R_{yy})/I_y & R_{yz}/I_y \\ -J_{ny}/I_z & R_{yz}/I_z & (N^2 - M^2 + R_{zz})/I_z \end{bmatrix}$$

$$I = M^2 + N^2 + P_x J_{yz} + P_y R_{ny} + P_z R_{nz}$$

$$I_x = M^2 + N^2 + P_x J_{yz}$$

$$I_y = M^2 + N^2 + P_y R_{ny}$$

$$I_z = M^2 + N^2 + P_z R_{nz}$$

$$N^2 = N N^* \quad M^2 = \mathbf{M}_\perp \cdot \mathbf{M}_\perp^*$$

$$R_{ni} = 2\text{Re}[N M_{\perp i}^*]; R_{ij} = 2\text{Re}[M_{\perp i} M_{\perp j}^*]$$

$$J_{ni} = 2\text{Im}[N M_{\perp i}^*]; J_{ij} = 2\text{Im}[M_{\perp i} M_{\perp j}^*]$$

Here, \mathbf{P}'' is the polarization created during the scattering process. I, I_x, I_y, I_z are the total and component-wise normalization factors, determined by the scattered intensity [53]. N and \mathbf{M}_\perp denote nuclear structure factor, and perpendicular magnetic interaction vector, respectively. $\mathbf{M}_{\perp i}$ denote the i^{th} component ($i = y, z$) of \mathbf{M}_\perp . The details of the above formalism can be found in Refs. [62, 63, 64]. During the spherical neutron polarimetry experiment, polarization analysis of the incident and scattered polarization can be performed to determine the components of \mathcal{P} , which is eventually connected with the magnetic moments of the sample. Therefore, the polarization analysis technique can determine the magnetic structure of the sample with great precision. The details of the spherical neutron polarimetry experiment will be described in the next chapter.

3 Experimental methods, instruments, and theory

3.1 Synthesis of single crystal

Single crystals are synthesized in two main steps. First, the induction melting of the elements is performed, then specific single crystal growth techniques are used. Both methods are described below in detail.

3.1.1 Induction melting

Reactants are melted in the cold crucible, which works on the basis of induction melting, which results in the homogeneous mixing of the elements. After this process, usually, the polycrystalline phase of the required compound is formed.

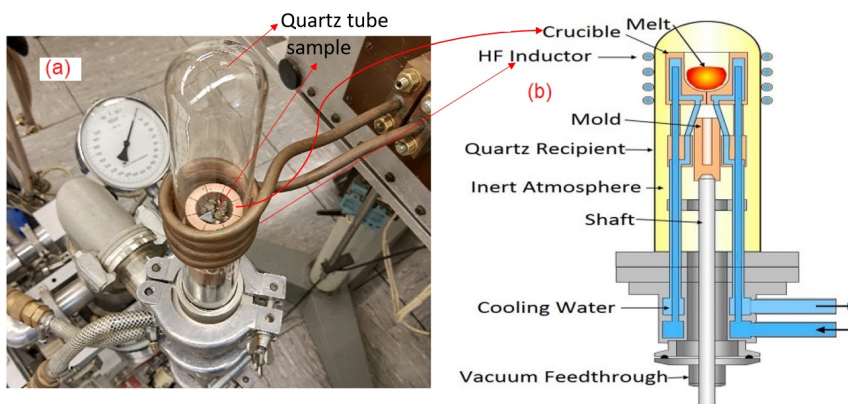


Figure 3.1: (a) Induction melting device. The sample is sealed into a quartz tube, under a high vacuum. (b) Schematic diagram of induction melting, showing various components of the instrument. (Taken from Ref. [65])

The reactants are placed in a copper crucible having a cold water supply passing through it to avoid heating. The sample chamber is closed with a quartz tube under the Ar gas atmosphere at low pressure (~ 200 mbar). The quartz tube is surrounded by the hollow copper coils (denoted as 'HF Inductor') as shown in the Fig. 3.1. Very high frequency (a few kHz) AC electric current passes through HF inductor. The high frequency change in the magnetic field generates Eddy current at the center, (where elements are kept for melting), leading to the Joule heating and melting of the elements. The instrument can efficiently melt the Mn, Fe, and Ge within a minute, which enables homogeneous mixing of all the elements. All the metals nearby the

coil, the copper crucible, and the coil itself are hollow, and cold water runs through it in order to avoid heating the coil or the copper crucible.

3.1.2 Single crystal growth technique

The fundamental principle behind a successful single crystal growth is - not allowing any other seed crystal to be formed except at the bottom tip of the crucible. Therefore, the temperature of the crucible has to be decreased very slowly to maintain thermal equilibrium and keep the temperature gradient along the crucible length (as shown in Fig. 3.2(a)) constant. This allows a single crystal to start its formation from the bottom tip to the top.

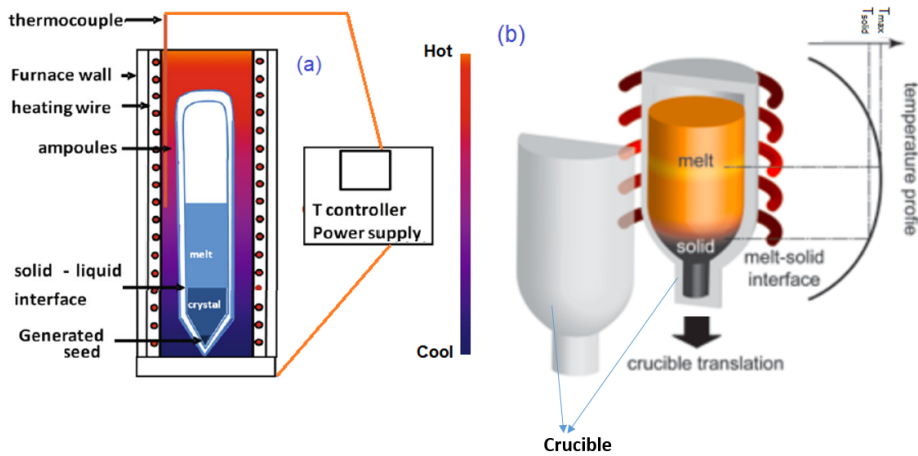


Figure 3.2: (Taken from Refs. [66, 67]) (a) Illustration of the vertical gradient method. Where, the sealed quartz tube is kept in the furnace, having a vertical temperature gradient such that it is coolest at the bottom and hottest at the top. The temperature is controlled by the controller. (b) Schematic diagram of the vertical Bridgman furnace in which sample (sealed inside the crucible) is kept under a temperature gradient. The crucible is pulled down very slowly, leading to the formation of a single crystal starting from the bottom, which cools first.

In order to synthesize the single crystals, the pre-melted alloy is sealed into the quartz tube and heated above its melting point in a high temperature furnace. After this, the primary aim is to start cooling down the crucible in such a way that there exists a temperature gradient along the crucible. One of the famous and convenient techniques for single crystal growth, which we also have used, is **vertical gradient**

method, which is illustrated in the Fig. 3.2(a). In this process, The sample is kept in a long crucible (6-7 cm) with a conical bottom tip, and sealed inside a quartz tube under an Ar gas atmosphere with 200 mbar pressure. The pressure is kept low at room temperature because it increases when the compound is heated in the furnace. The design of the furnace is such that it is hotter on the top and cooler at the bottom. The compound is heated in the furnace beyond its melting point. Further, the temperature of the furnace is decreased at a very slow rate (usually 0.5 K/hr - 2 K/hr). Since the bottom surface is cooler than other surroundings, the conical bottom tip of the crucible starts to cool down at first. As soon as the bottom tip cools below the melting point, the seed crystal is formed there. As time passes, the temperature of the whole crucible decreases, and the molten compound starts to cool from the bottom (around the seed crystal) to the top, very slowly, leading to the synthesis of a single crystal via the process of nucleation. The furnace cooled very slowly so that the temperature gradient and thermal equilibrium are maintained throughout the cooling process. Once the whole crucible is cooled below the melting point, the resultant solid material is formed as a single crystal.

Another famous technique for single crystal growth is the **Bridgman–Stockbarger technique**, which is illustrated in the Fig. 3.2(b). The physics behind this method is the same as the vertical gradient method described above, however, the mechanism is different. In this process, after the compound is heated beyond its melting point, the crucible is pulled very slowly (usually, 1-2 mm/hr) from the hot zone. The bottom of the crucible, usually having a conical shape, starts to cool down first, leading to the formation of a seed crystal at the bottom tip. Once the whole crucible is pulled out of the hot zone at a slow enough rate, the molten compound solidifies in a form of a single crystal, the same as the above.

In case, the cooling of the crucible is faster than a critical rate, or, somehow, the temperature gradient gets uncontrolled during the cooling process, the crucible won't be able to maintain the monotonic thermal gradient, leading to the formation of several seed crystals at multiple sites. This results in a multi grain crystal, or single crystal with < 0.5 mm size, which is not suitable for transport measurements. Therefore, we have used a very high quality furnace, which can stabilize the temperature within 0.1 K, and cooled down our sample very slowly (~ 1 K/hr). Using these techniques, we were able to grow large single crystals (1 - 3 mm), which were sufficient for our various measurements.

3.2 Inductively coupled plasma - optical emission spectrometry (ICP-OES) method

After the sample preparation is complete, the chemical analysis of the sample is performed to determine the ratio of elements present in the sample. The chemical analysis is performed using the Inductively coupled plasma - optical emission spectrometry (ICP-OES) method. The chemical analysis is important because the loss of any element during the process of synthesis may lead to the presence of unwanted phases. If some of the elements were found to be lesser than we expect, the extra amount of that element was added during the next preparation to ensure that the final chemical composition remains the same as we desired.

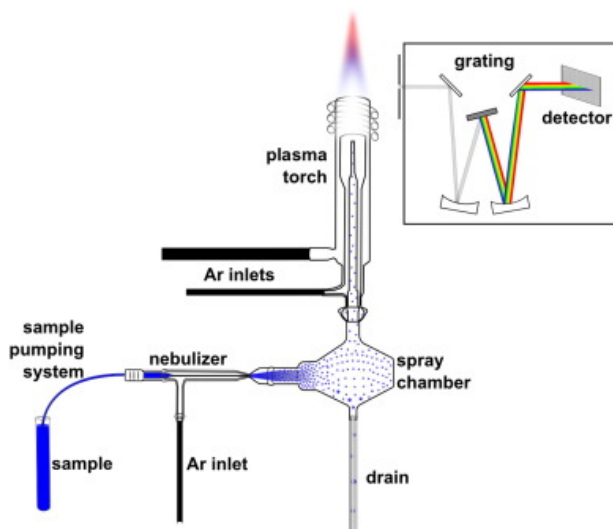


Figure 3.3: (Ref. [68]) Various parts of the instrument were used to analyze the elements of the compound under study, using the ICP-OES method. The diagram in the inset illustrates optics, which shows how the characteristic light is filtered out to the detector.

The concentration of elements in a given sample is analyzed using the ICP-OES method, using an instrument that involves various setups as shown in the Fig. 3.3. Initially, the sample is dissolved into acid or any other suitable solvent. The dissolved liquid goes to the nebulizer where it mixes with Ar gas, and further turns into the aerosol particles in the spray chamber. Further, the particles travel to the plasma

torch made with the RF (radio frequency) power supply in the presence of Ar gas. The plasma radiations excite the atoms present in the aerosol particle, which results in the emission of light with a characteristic wavelength. The components of the light are separated using the prism, and the wavelength of the light is measured. Since each element has a characteristic spectroscopic emission, the wavelength of light can be related to the elements present in the sample. The intensity of the light is also measured, which gives the concentration of the element. This way, the relative concentration of all elements can be measured in a given sample.

3.3 X-ray diffraction methods

As mentioned in the previous chapter, X-ray diffraction is a unique technique to determine the microscopic details of the compound. X-ray sources are widely available, therefore X-ray diffraction of all the samples was performed before any further study. Specific X-ray instruments were used to characterize the lattice parameter, and quality of single crystals, and to determine the crystallographic axes of a sample piece.

3.3.1 X-ray powder diffraction

X-ray powder diffraction is the most precise technique to determine the lattice parameters of the compound. It also determines if the sample is synthesized in a single desired phase, or if any other undesired phase is also present. We have used the Huber diffractometer with Cu-K $_{\alpha}$ X-ray source ($\lambda = 1.5406 \text{ \AA}$) to collect the diffraction pattern in transmission geometry. The instrument is equipped with the G670 Guinier camera, behind the sample platform, which is integrated with an imaging plate detector as shown in the Fig. 3.4. A detailed schematic diagram of the Guinier camera and underlying geometry is also shown in the Fig. 3.4. A thin layer of powder sample is prepared within two plastic films and is mounted on the sample holder. The incoming monochromatic X-ray beam diffracts with the sample as illustrated in the Fig. 3.4(a). The basic principle of X-ray diffraction has been already discussed in the last chapter. The diffracted beams fall on the imaging plate at a specific angle depending on intra-planar spacing corresponding to the various crystallographic planes present in the sample. The instrument is equipped with a closed cycle cryostat also, which can cool down the sample down to 30 K. Using this setup, temperature-dependent X-

ray diffraction was performed to determine the temperature dependence of the lattice parameters. The X-ray pattern is stored in terms of scattered intensity vs. angle of diffraction, which is further analyzed using the FullProf software to characterize the sample under study.

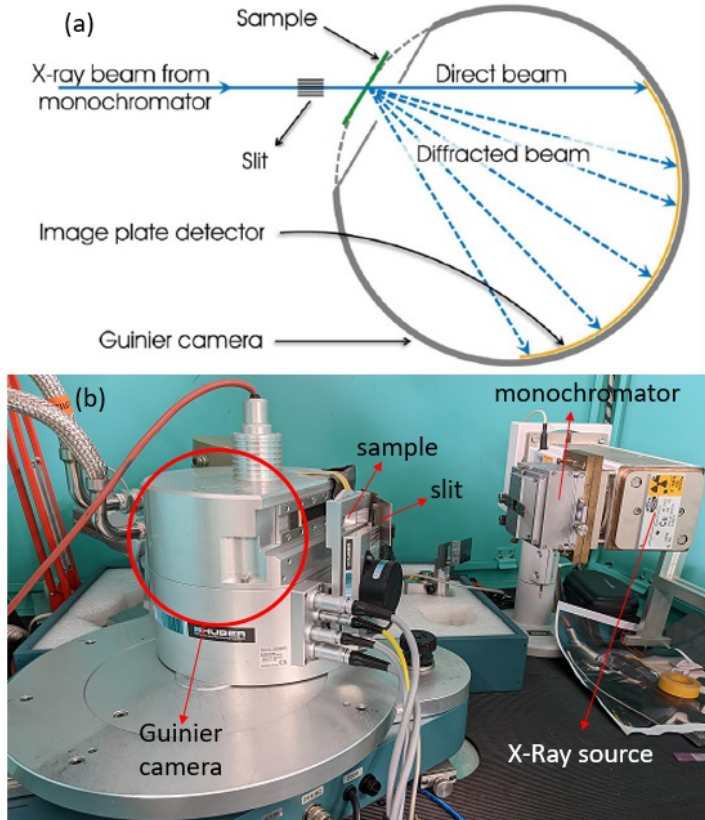


Figure 3.4: (a) shows the Guinier geometry (taken from [69]) which is used in the powder diffractometer to collect the data. (b) shows an X-ray powder diffractometer instrument with various components.

3.3.2 Laue diffraction

The Laue diffraction method is used to identify the crystallographic axis of a piece of a single crystal (bigger than 1 mm). It also determines the quality of the single crystal. If a sample piece has single grain of the single crystal, the Laue pattern does not

change when the sample is translated in any direction, while maintaining the same orientation. The MWL120 Real-Time Back-Reflection Laue Camera works on the

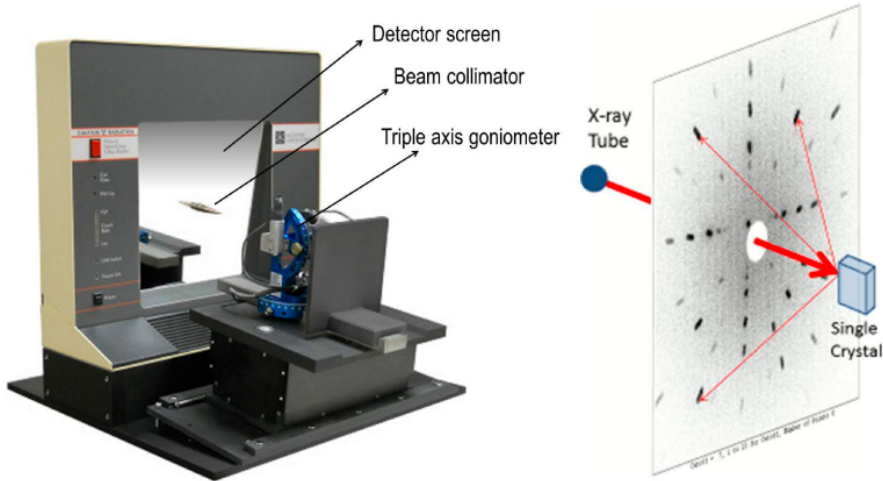


Figure 3.5: (Ref. [69]) X-ray Laue camera, and illustration of the single crystal scattering leading to the formation of a Laue pattern.

basis of the reflection geometry. The instrument and working principle are shown in the Fig. 3.5. In this instrument, a collimated X-ray beam with multiple wavelengths, with a lower cutoff determined by the voltage applied, falls on the sample which is mounted on the triple-axis goniometer (Fig. 3.5). The particular orientation of the crystal selects a wavelength (on the basis of the Laue condition) among the spectrum and diffracts it backward on the flat area detector screen as shown in the Fig. 3.5. The flat detector screen is made up of an array of high voltage wires (separated by a very small distance) inside a chamber having Ar gas inside it. The wires create a uniform electric field inside the chamber. When X-rays pass through the chamber, it ionizes the surrounding Ar atoms, and the produced ions-electrons are accelerated across the chamber due to the present electric field. The ions condense around the nearest wire, which generates a charge proportional to the amount of ionization of the (detected) particle. By measuring the pulse generated through all the wires, the location of the scattered X-ray beam can be determined. 'NorthStar 7' software is used to control the instrument. The Laue pattern for any crystal can also be simulated using the OrientExpress software, which is helpful to determine the orientation of the crystal.

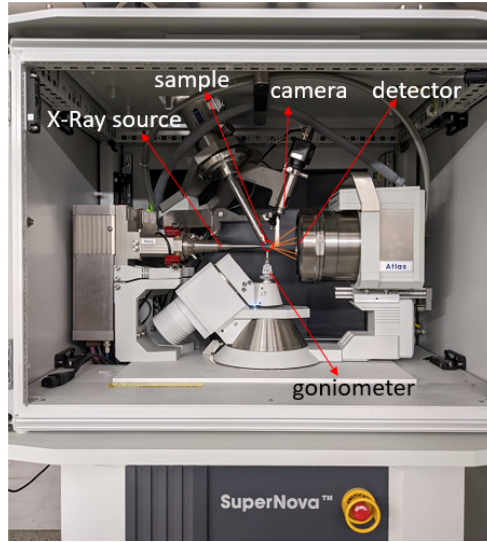


Figure 3.6: SuperNova (6- circle) single crystal diffractometer which operates on the transmission geometry. The source of X-ray is Molybdenum (Mo).

3.3.3 Single crystal X-ray diffraction (Supernova)

In order to check the microscopic crystalline nature of the crystals, 6-circle SuperNova (Agilent) single crystal diffractometer was used. The instrument can work with multiple sources, however, we have used Molybdenum (Mo) as the source of X-ray, having a wavelength, $\lambda_{\text{Mo}} = 0.709 \text{ \AA}$. The instrument works in the transmission geometry, therefore a very small size of a single crystal (~ 100 micron) with a nearly spherical shape is used during the experiment. Various components of the instrument are shown in the Fig. 3.6. The sample is glued to the tip of the goniometer and further aligned to the center with the help of a high-resolution camera attached near the sample. The diffracted beam hits the area detector, which can also move around the sample. 6 degrees of freedom of this instrument allow the scanning of a large range of scattering vectors (\mathbf{Q}).

It is often hard to find the round-shaped sample piece, which leads to the anisotropic absorption of the X-ray. Therefore, while performing the data analysis using CrysAlisPro software, absorption correction is performed depending on the shape of the crystal.

3.4 Physical properties measurement system (PPMS)

PPMS is an instrument that provides low and high-temperature range (2 K - 400 K) and high magnetic field (± 9 T) environment to the sample under study. Along with that, it also provides various options which can be used to measure the desired physical properties of the sample. Quantum-Design PPMS DynaCool is also a setup similar to the PPMS, however, it has a few advanced features not available in the PPMS. We have extensively used Quantum Design PPMS and DynaCool instruments to measure the magnetization and resistivity of the sample, using various options mentioned below.

3.4.1 Magnetization (VSM)

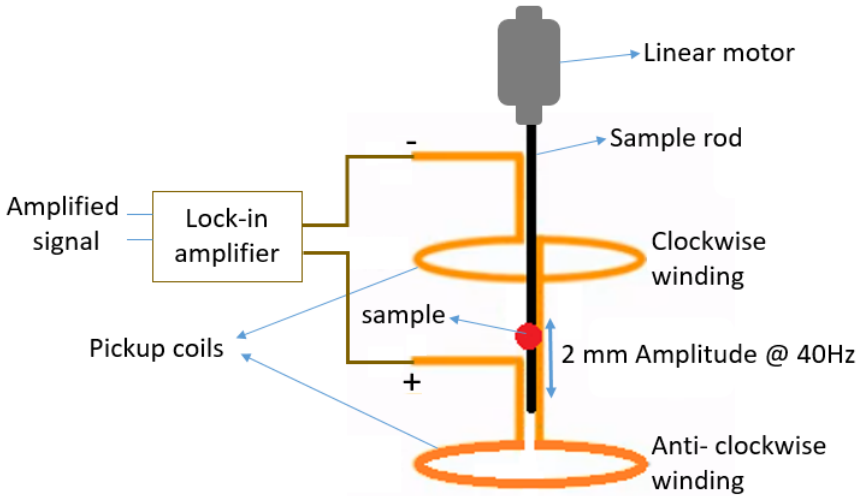


Figure 3.7: (Ref. [70]) Illustration of the working principle of the VSM setup.

The magnetization of the sample can be measured using the vibrating sample magnetometer (VSM) installed at the PPMS. It is a very fast and sensitive technique to measure the DC magnetization of the sample within the accuracy of 7×10^{-7} emu. As illustrated in the Fig. 3.7, the sample oscillates between two coils at 40 Hz frequency, with an amplitude of 2 mm, which changes the magnetic flux through the pickup coils. The change in magnetic flux in the coils generates electric potential at the ends. One end of both the coils is connected, however, the coils are wound in

opposite directions, so that the voltage induced due to the sample oscillations does not cancel out. The induced voltage is given by

$$V_{coil} = -\frac{d\phi}{dz} \frac{dz}{dt} = C[A\omega \sin(\omega t)]m \quad (3.1)$$

Where, C = coupling constant, A = oscillation amplitude (usually, 2 mm), and ω is the frequency of the vibrating sample. Once the voltage is measured, using this relation, magnetic moment (m) of the sample can be calculated.

Using the ACMS-II setup installed over the DynaCool, the AC susceptibility of the sample can be determined by applying the AC magnetic field. In AC measurement, the magnetic field oscillates with a high frequency. The sample, which remains stationary, generates a magnetic moment in response to the AC magnetic field. This helps in the study of the magnetization dynamics of the sample. The relation between AC susceptibility ($\chi_{AC} = \frac{dM}{dH}$) and induced AC magnetization (M_{AC}) is given as

$$M_{AC} = \chi_{AC}(H_{AC} \sin(\Omega t)); \chi_{AC} = \sqrt{(\chi')^2 + (\chi'')^2} \quad (3.2)$$

Where, χ' and χ'' denote real and imaginary part, respectively, of the χ_{AC} . Ω is frequency of the magnetic field. χ_{AC} gives information about the relaxation time of the magnetic sample.

3.4.2 Electrical transport measurements

Electrical transport measurements of the samples were performed using the *resistivity* and *electrical transport* options available in the PPMS and DynaCool, respectively. Different types of resistivity puck were chosen depending on the required measurement, as shown in the Fig. 3.8. 4-probe contacts were used to determine the electrical resistivity or Hall resistivity of the sample. Fig. 3.8(b) shows the contacts corresponding to the Hall resistivity, and longitudinal resistivity measurements, simultaneously. The direction of the magnetic field is fixed inside the PPMS. However, the sample can be installed in different orientations relative to the external magnetic field. For rotational measurements, the rotator option (3.8(c)) can also be used in the PPMS setup to measure the planar Hall resistivity and anisotropies in the magneto-resistivity.

To avoid any extrinsic effects due to an inhomogeneous electric field, cuboid-shaped long (1 mm - 2.5 mm), and thin (0.1 mm - 0.25 mm) samples were prepared for all the electrical transport measurements. Since the sample we used for the measurements is

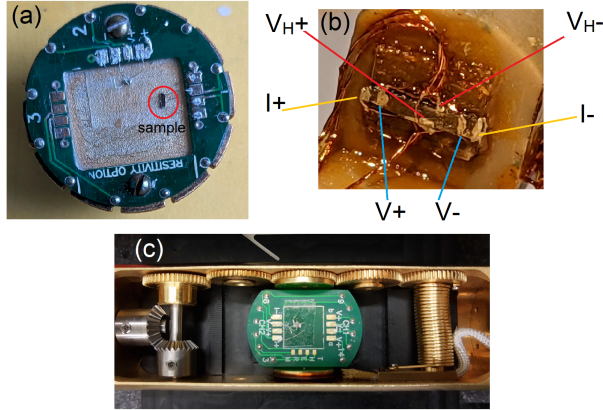


Figure 3.8: (a) shows the sample contact made on the resistivity puck, which is used in the PPMS for resistivity measurements. (b) shows the Hall and longitudinal resistivity contacts. The electric current along the length of the sample (I_{\pm}). For longitudinal resistivity, the voltage is measured along the direction of the current, denoted as V_{\pm} . However, Hall voltage contacts (shown as $V_{H\pm}$) are made in the transverse direction, to measure the transverse resistivity. Usually, Hall resistivity and longitudinal resistivity are measured separately, except in a few cases when necessary. (c) shows the rotator option available in the ppms, which can rotate the sample with respect to the external magnetic field.

semi-metallic, low amplitude of electric current (5 mA - 10 mA) in AC (15 - 20 Hz) or DC current was applied in the I_{\pm} terminal of the sample as shown in the (3.8(b)). Most often, AC current was preferred during the resistivity as it gives a more precise and intrinsic value of the sample resistance. For Hall and longitudinal and resistivity, the voltage was measured along longitudinal (V_{\pm}) and transverse ($V_{H\pm}$) directions, respectively. Each measurement was recorded with 2-3 seconds of waiting time. While performing the rotational measurements, the sample platform was rotated very slowly at the speed of $\sim 0.7^{\circ}/s$.

3.5 High magnetic field measurements at HZDR Dresden

High field magneto-resistivity and Hall resistivity measurements were performed at Hochfeld-Magnetlabor, Helmholtz-Zentrum Dresden-Rossendorf (HZDR). The facility

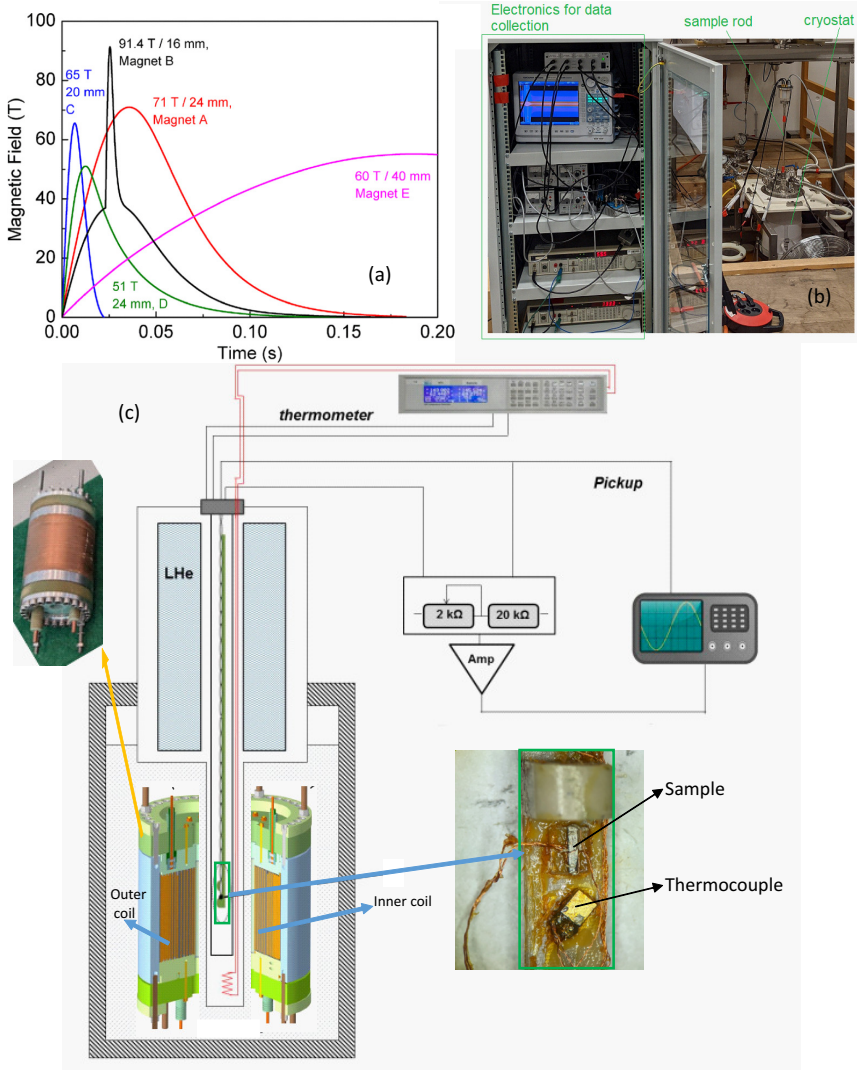


Figure 3.9: (Taken and modified from Ref. [71, 72]) (a) Time-dependent magnitude of the various pulsed magnetic fields. Magnets A, and D correspond to the 8.5 MJ and 1.5 MJ, respectively, which lie within the 24 mm bore region. Magnet B has a double coil with 9.5 MJ energy, leading to 91.4 T of the maximum magnetic field, for short time, in a 16 mm bore. Magnets C and E correspond to the 1 MJ and 43 MJ energy, respectively, in the 20 mm and 40 mm bore regime. (b) Experimental setup for the high field resistivity measurements. (c) Illustration of the various components of the high field resistivity setup.

provides a high magnetic field (up to 90 T) along with a low temperature environment using the He cryostat setup.

The generation of a high magnetic field works on the basic principle of electromagnetic induction defined as

$$V_{ind} \propto \frac{d\Phi}{dt} = A \frac{dB(t)}{dt} \quad (3.3)$$

Where V_{ind} is the induced voltage. The magnetic field is produced inside an inductor when current flows through it. The magnetic energy corresponding to a high field greater than 40 T is too high and risky to store safely for a long time. Therefore, to achieve a high magnetic field (>40 T), it is generated in a pulsed form for less than 0.15 seconds to avoid heating and melting of the coil. At HZDR, the process begins with the capacitors bank having the capacity to store ~50 Mega Joule (MJ) of energy, and can generate a maximum power of ~5 GW. The capacitors are charged using a high voltage (25 kV) electric current, and ~50 MJ of energy is stored. The pulsed magnetic field is generated in a different chamber, which is separated from the capacitor bank, where a pick-up coil with a particular bore diameter is placed inside a liquid nitrogen tank below 77 K to cool it down and keep the Ohmic resistance low. When the capacitor is discharged through the pickup coil, the current in the coil increases, which generates the magnetic field at the core of the coil. The time constant of the capacitor bank is kept small, so that the magnetic pulse dies, usually, within 0.15 seconds (s). The maximum magnitude of the magnetic field generated due to discharging of the capacitor also depends on the time constant of the capacitor. Lower the time constant, the higher the magnetic field which will be generated.

Before starting the high field measurement, 4 probe contacts were made on the sample under study, and inserted 1.5 m deep, within the bore of the pick-up coil, as illustrated in the Fig. 3.9(c). All the electrical wiring and materials used during the measurement are made from special materials to minimize the eddy current. Most often, we performed measurements using the magnet A, where 8.5 MJ of capacitor energy is discharged through the pickup coil with a 24 mm bore diameter, to produce 71 T of the maximum magnetic field. When the capacitor is discharged through the pickup coil, the electric flux increases in the coil, leading to an increase in the magnetic field. The magnetic field reaches a maximum within 40 ms, then starts to decrease with current exponentially, and vanishes nearly after 150 ms. The voltage signal from the sample is amplified and measured using YOKOGAWA (DL850 ScopeCoder) oscilloscope, which collects nearly 10^6 voltage points per second. After every pulse,

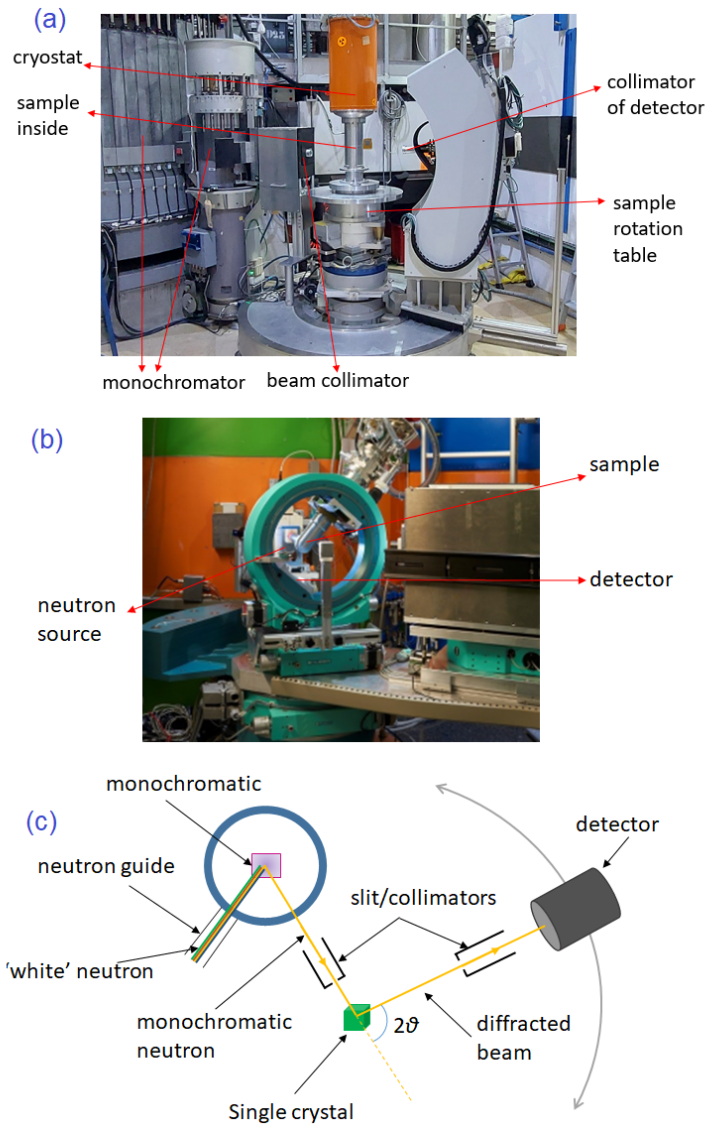


Figure 3.10: (a) Different parts of the D23 instrument (modified from Ref. [73]). (b) Few parts of the HeiDi instrument are shown (modified from Ref. [74]). (c) The illustration of scattering geometry corresponding to both the instruments.

with the 62 T highest magnetic field, the coil heats due to the enormous energy released due to the Ohmic resistance of the coil. Therefore, a minimum of 3 hrs of waiting time is required between two magnetic pulses with a 62 T magnetic field. For lower energy discharge, the waiting time is also lower. The temperature inside the bore (sample chamber) also rises by 5-10 K.

3.6 Single crystal neutron scattering facilities

As mentioned in the previous chapter, neutron diffraction can reveal the microscopic details of the sample. We have employed neutron diffraction techniques using the single crystals for two main reasons: (i) to determine the ground state magnetic structure of the parent and doped samples. (ii) to find out the occupancy of Mn, Fe, and Ge at various lattice sites.

3.6.1 HEiDi (FRM-II, Garching, Germany) and D23 (ILL, Grenoble, France)

Unpolarized neutron diffraction of the samples was performed using the HEiDi instrument available at FRM - II, Garching, Germany, and the D23 instrument at ILL, France. The working principle of both instruments is almost the same. Both instruments provide a powerful and versatile technique to determine the magnetic structure of the single crystal under measurement. HEiDi and D23 instruments are 4-circle and 2-circle diffractometers, respectively. For the experiment, the monochromatic wavelength is selected from the achromatic (or white) neutron beam, using a suitable monochromator. During our experiment with HEiDi, Cu(220) monochromator was used to select the neutron beam with 0.87 Å wavelength. Whereas Cu(200) monochromator was used in D23, ILL to select a wavelength of 1.27 Å.

Before starting the measurement, the single crystal with a roughly known orientation of the crystallographic axes is mounted on the platform. Afterward, the sample is centered, and the lattice parameters and crystal symmetry information (pre-determined using X-ray diffraction) is provided to the instrument, which enables the instrument to calibrate and find the location of various (h k l) planes. Since the sample holder, detector, and other movable parts have limitations for their movement, reflections only up to a certain scattering angle can be collected. The range of scat-

tering angles depends on the possible axes available for rotation, and the wavelength of the neutron beam used for the experiment.

3.6.2 Spherical neutron polarimetry using CRYOPAD (D3), ILL, France

As described in the previous chapter, polarized neutrons can provide the microscopic details of the magnetic structure of the sample with more accuracy and less ambiguity, when compared to unpolarized neutron diffraction. However, it is a difficult task to perform such an experiment because any stray magnetic field can depolarize the neutrons, leading to the wrong information. The efficient way to perform a generalized polarization experiment is to keep everything (sample, polarized incident beam, and diffracted polarized neutron) within a superconducting shield, which makes the interior free of any magnetic field due to the Meissner effect. Such a superconducting shield is known as Meissner superconducting shield. The experiment can be performed using the CRYOgenic Polarization Analysis Device (CRYOPAD), installed at the D3 setup (Fig. 3.11(c)), ILL, France. The CRYOPAD device enhances the capability of the instrument to perform the polarization analysis of the incident and diffracted neutron beam [75]. As mentioned in the previous chapter (section 2.7.5.3), scattered and incident polarization is related to the magnetic structure of the sample. Therefore, the precise magnetic structure can be calculated by analyzing the polarization matrix elements.

The diffraction geometry for SNP measurement is illustrated in the Fig. 3.11(a). Various components of the CRYOPAD instrument and their usage is mentioned in the Fig. 3.11(b). During the experiment, the sample is oriented with a particular crystallographic axis in the vertical position, referred as the z axis. The scattering vector (\mathbf{Q}), which is perpendicular to the z , is referred as x axis. Once x and z is defined, y is chosen perpendicular to x , z axes both, to complete x , y , z directions as a Cartesian coordinate system. The initial polarization of the incident beam is 0.935. Cu_2MnAl monochromator is used to select a monochromatic neutron beam with 0.832 Å wavelength. Before starting the experiment, our sample was cooled down, below room temperature (300 K), under the application of 1 T magnetic field along the b axis of the crystal. Since the sample was installed with the c axis, and b axis along the vertical direction, horizontal and vertical magnetic field setups were used to apply magnetic field along the b axis in both cases. The field cooling of the

sample populates most of the magnetic domains along a particular axis.

The path of the incident neutron beam is fixed by the D3 instrument. The incident beam nutator polarizes the beam in a plane which is perpendicular to the beam direction. The polarization of the incident beam changes as it scatters from the magnetic moment present in the sample. All three components of the diffracted beam are measured using the nutator of the diffracted beam. This experiment is repeated for three different axes (x, y, z) of incident polarization, and in each case, all the three polarization components (x, y, z) of the diffracted beam is measured. One set of an experiment for a particular (hkl) plane of the sample gives 3×3 polarization matrix elements (\mathbf{P}), which can be written as

$$\mathbf{P} = \begin{bmatrix} P_{xx} & P_{xy} & P_{xz} \\ P_{yx} & P_{yy} & P_{yz} \\ P_{zx} & P_{zy} & P_{zz} \end{bmatrix}$$

Where, for any given term P_{ij} , i denotes the incident polarization and j denotes the measured polarization component after the diffraction. The polarization matrix \mathbf{P} is the normalized version of the \mathbf{P}' (scattered polarization). So, the relation between \mathbf{P} , \mathbf{P} (incident polarization) and \mathbf{P}' is given (on the basis of section 2.7.5.3) as

$$\mathbf{P} = \left\langle \frac{\mathbf{P}'}{|\mathbf{P}|} \right\rangle_{Dom} = \left\langle \frac{\mathcal{P}\mathbf{P} + \mathbf{P}''}{|\mathbf{P}|} \right\rangle_{Dom}; \text{ in components: } P_{ij} = \left\langle \frac{(\mathcal{P}_{ij}P_i + P''_j)}{|\mathbf{P}|} \right\rangle_{Dom} \quad (3.4)$$

Where, $\langle \dots \rangle_{Dom}$ defines that the polarization is averaged over all the possible magnetic domains. The meaning of various terms is given in the section 2.7.5.3. Since the polarization of the scattered beam depends on the direction of the magnetic moments present in the sample, a set of polarization matrix \mathbf{P} , corresponding to the different planes, are experimentally determined, and analyzed using the MAG2POL software [78]. Before the analysis, different possible magnetic models are selected, using the representation analysis corresponding to the observed propagation vector (\mathbf{k}), and magnetization of the sample. All the models are fitted using the MAG2POL, and the best fitted model is chosen to be the correct magnetic structure of the sample. We have exploited the polarization analysis technique to determine the ground state magnetic structure of the doped sample, which was not possible solely based on unpolarized single-crystal neutron diffraction. The specific details of the experiment will be discussed in the chapter 6.

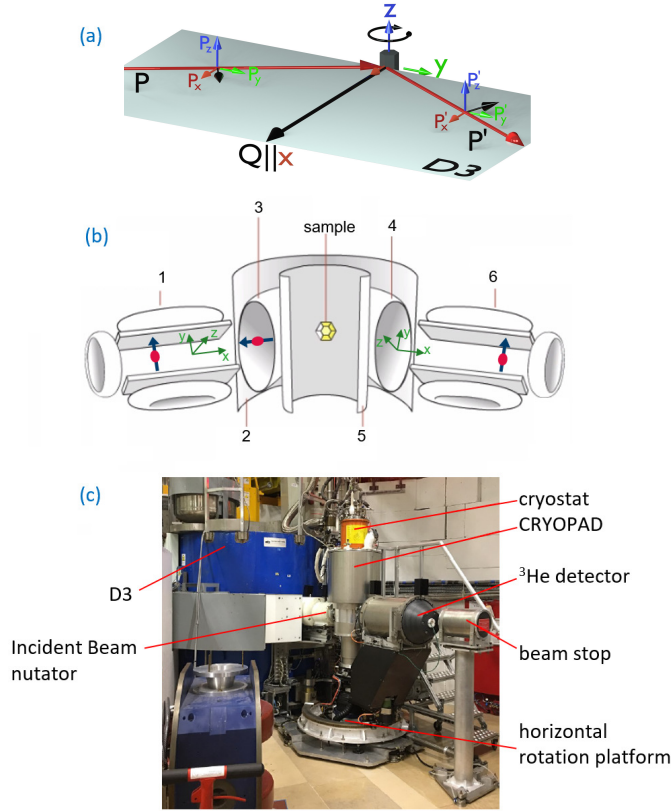


Figure 3.11: (a) Scattering geometry for the spherical neutron polarimetry measurement. P_i , P'_i denote i^{th} component ($i = x, y, z$) of the polarization of incident and diffracted beam, respectively. \mathbf{Q} is the scattering vector, which defines the x axis. (b) Pictorial representation of the different components of the CRYOPAD instrument (modified from Ref. [76]). 1: Incident beam nutator (magnetic path containing longitudinal static guide field). 2: Outer superconducting shield (Niobium) 3: Precession coil (rotates the incident beam polarization around a horizontal axis perpendicular to the incident beam). 4: Precession coil for diffracted beam (aligns the chosen polarization component to the axis of the diffracted beam). 5: Inner superconducting shield (protects magnetic field due to precession coils, and maintains a zero-field environment in the sample chamber). 6: Nutator of the diffracted beam (c) A picture of the CRYOPAD setup installed with the D3 setup. A few parts are also shown (taken from [77]).

4 Synthesis and characterization of Hexagonal - $[\text{Mn}_{(1-\alpha)}\text{Fe}_{\alpha}]_{3+\delta}\text{Ge}$

4.1 Sample preparation

With reference to the Mn-Ge binary phase diagram (Fig. 4.1), it can be guessed that Mn_3Ge phase has to be synthesized as $Mn_{3+\alpha}Ge_{1-\alpha}$, where $\alpha \approx 0.03 - 0.11$ [79]. $Mn_{3+\alpha}Ge_{1-\alpha}$ can also be written as $Mn_{3+\delta}Ge$, with $\delta = 0.1 - 0.5$. It has been well established using neutron diffraction measurements that the excess Mn occupies Ge site [52, 80]. We also observed in the neutron diffraction analysis that the Ge sites are being occupied by the excess Mn atoms. The details of the neutron diffraction analysis will be discussed in the chapters (5, 6). It is also important to note from the binary phase diagram that the $Mn_{3+\delta}Ge$ forms in hexagonal (ϵ) and tetragonal (ϵ_1) phases, which remain stable above and below 630 °C, respectively.

In order to study the evolution of Fe doping in Weyl semimetal Mn_3Ge , we synthesized $[Mn_{(1-\alpha)}Fe_{\alpha}]_{3+\delta}Ge$ single crystal (SC). Several Fe doped samples were synthesized as mentioned in Table 4.1. Starting from 26% Fe doping, the samples show magnetization completely different from the parent sample, which suggests a vanishing Mn_3Ge type magnetic structure. Since we are interested in the compounds with Mn_3Ge type magnetic structure, only one sample was synthesized beyond $\alpha = 0.26$, to estimate the evolution of magnetism with Fe doping.

High quality hexagonal - $[Mn_{(1-\alpha)}Fe_{\alpha}]_{3+\delta}Ge$ compounds with different α (mentioned in the Table 4.1) were synthesized using the vertical temperature gradient method mentioned in the chapter 3. First of all, stoichiometric amounts of the high purity Mn, Fe, and Ge elements (>99.99%) were mixed and melted using the induction melting method mentioned in the last chapter. Further, the alloy was crushed and sealed into the quartz tube under Argon atmosphere under 300 mbar pressure. The sealed tube was kept in the furnace and heated to 1000 °C, followed by slow cooling (1 °C/hr) down to 850 °C. Further, the quartz tube was quenched into the water so that the compound retains the high temperature hexagonal phase.

4.2 Sample characterization

4.2.1 Chemical analysis

Once the sample is ready, chemical analysis of the compounds was performed using the ICP-OES method. The results of the chemical analysis are mentioned in the second column of Table 4.1. The measured doping concentration was observed to be

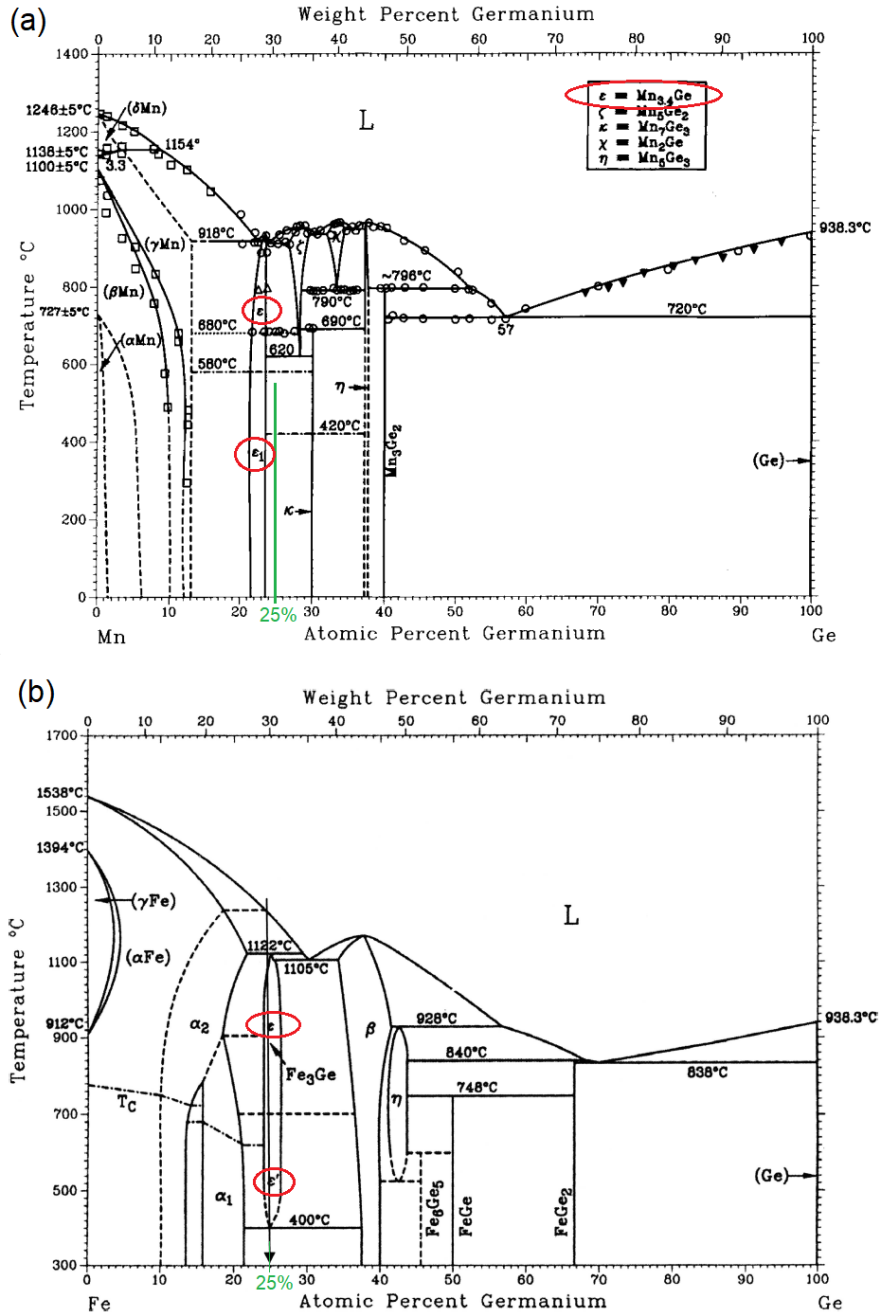


Figure 4.1: (a) Binary phase diagram of Mn - Ge[79]. (b) Binary phase diagram of Fe - Ge [81]. In both cases, ϵ and ϵ_1 phases (encircled by red) denote hexagonal and tetragonal phases.

close to the stoichiometry of the elements we started with.

Table 4.1: Stoichiometry of the compound taken before preparation is mentioned in the first column as ‘Starting stoich.’. After the synthesis, the stoichiometry of the compounds determined by the chemical analysis is mentioned in the second column as ‘Final stoich.’. 14% and 26% Fe doped samples were very small in amount, so chemical analysis could not be performed (mentioned as ‘Not done’). The samples are symbolized or mentioned in the following chapters as mentioned in the third column (‘Referred as’). The sample type is mentioned in the fourth column. SC and poly denote the single crystal and polycrystalline nature of the sample, respectively.

Starting stoich.	Final stoich.	Referred as	SC/poly
$Mn_{3.05}Ge$	$Mn_{3.10(5)}Ge$	$Mn_{3.1}Ge$ (S1)	SC
$Mn_{3.15}Ge$	$Mn_{3.20(5)}Ge$	$Mn_{3.2}Ge$ (S2)	SC
$Mn_{3.3}Ge$	$Mn_{3.55(5)}Ge$	$Mn_{3.5}Ge$ (S3)	SC
$(Mn_{0.97}Fe_{0.03})_{3.2}Ge$	$(Mn_{0.96(1)}Fe_{0.04(1)})_{3.25}Ge$	$(Mn_{0.96}Fe_{0.04})_{3.2}Ge$	SC
$(Mn_{0.90}Fe_{0.10})_{3.2}Ge$	$(Mn_{0.90(1)}Fe_{0.10(1)})_{3.18}Ge$	$(Mn_{0.90}Fe_{0.10})_{3.2}Ge$	SC
$(Mn_{0.86}Fe_{0.14})_{3.2}Ge$	Not done	$(Mn_{0.86}Fe_{0.14})_{3.2}Ge$	SC
$(Mn_{0.82}Fe_{0.18})_{3.2}Ge$	$(Mn_{0.83(1)}Fe_{0.17(1)})_{3.25}Ge$	$(Mn_{0.82}Fe_{0.18})_{3.2}Ge$	SC
$(Mn_{0.77}Fe_{0.23})_{3.2}Ge$	$(Mn_{0.79(1)}Fe_{0.21(1)})_{3.2}Ge$	$(Mn_{0.78}Fe_{0.22})_{3.2}Ge$	SC
$(Mn_{0.74}Fe_{0.26})_{3.2}Ge$	Not done	$(Mn_{0.74}Fe_{0.26})_{3.2}Ge$	poly
$(Mn_{0.70}Fe_{0.30})_{3.2}Ge$	$(Mn_{0.68(1)}Fe_{0.32(1)})_{3.2}Ge$	$(Mn_{0.7}Fe_{0.3})_{3.2}Ge$	poly

4.2.2 X-ray powder diffraction

X-ray powder diffraction (XRD) of all the samples was performed using the Huber X-ray diffractometer instrument mentioned in the last chapter. A powder sample of the single-crystal compounds was prepared by crushing a few pieces the crystals. The XRD pattern of the samples (used for the transport measurements) is shown in the Fig. 4.3. The data was analyzed using the FullProf software, and the goodness of the fitting parameter (χ^2) corresponding to the fitting is mentioned in each plot. The powder diffraction pattern in all the cases has been fitted with $P6_3/mmc$ space group (no. 194) symmetry. In the case of parent and 4% Fe doped samples, small peaks corresponding to the tetragonal- Mn_3Ge (space group symmetry $I4/mmm$) phase were also observed. A small amount of tetragonal impurity (low temperature) phase is inevitable in the case of Mn_3Ge samples, as reported by Refs. [37, 80]. The amount of tetragonal phase is less than 5% in each case. For higher doping (10%, 18%, 22%),

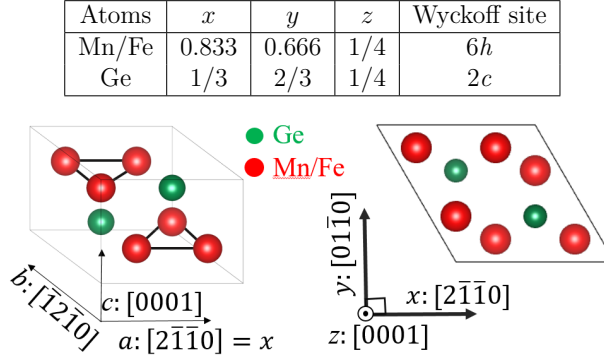


Figure 4.2: The table on the top shows the position of atoms corresponding to space group $P6_3/mmc$. The figure below shows nuclear structure of $(\text{Mn}_{(1-\alpha)}\text{Fe}_{\alpha})_3\text{Ge}$ in two different orientations.

no impurity peak was observed. In the case of 30% Fe doped samples, a pair of (small) impurity peaks were observed, which does not match the tetragonal phase. However, these impurity peaks were not observed in the case of 60% Fe doping. It can be observed in the Fig. 4.3 that the (200), (002), and (201) peaks shift towards higher 2θ with an increase in Fe doping, suggesting a decrease in the lattice parameters. The obtained lattice parameters are shown in the Fig. 4.4, where it is obvious to observe that the lattice parameters and volume decrease, almost linearly, with an increase in Fe doping. Such linear behavior justifies the validity of Vegard's law in Fe doped Mn_3Ge compounds. The hexagonal lattice structure corresponding to the space group $P6_3/mmc$ symmetry is shown in Fig. 4.2.

4.2.3 Laue diffraction and SC X-ray diffraction

Unlike Mn_3Sn , Mn_3Ge single crystals do not possess cleavage in a - b plane, which makes it difficult to guess the type (poly/SC) of the crystal. To determine the quality of the crystals, Laue diffraction of each sample was performed. Laue diffraction corresponding to the Mn_3Ge , along the three different axes, is shown in Fig. 4.5. Similar hexagonal Laue peaks were observed for all the samples up to 22% Fe doping. For $\alpha \geq 0.26$, the crystals showed very low intensity and scattered Laue peaks, suggesting the bad quality of the single crystal. Therefore samples with, $\alpha \geq 0.26$ were treated as polycrystalline. Also, no anisotropy in magnetization was observed, which implies its polycrystalline nature.

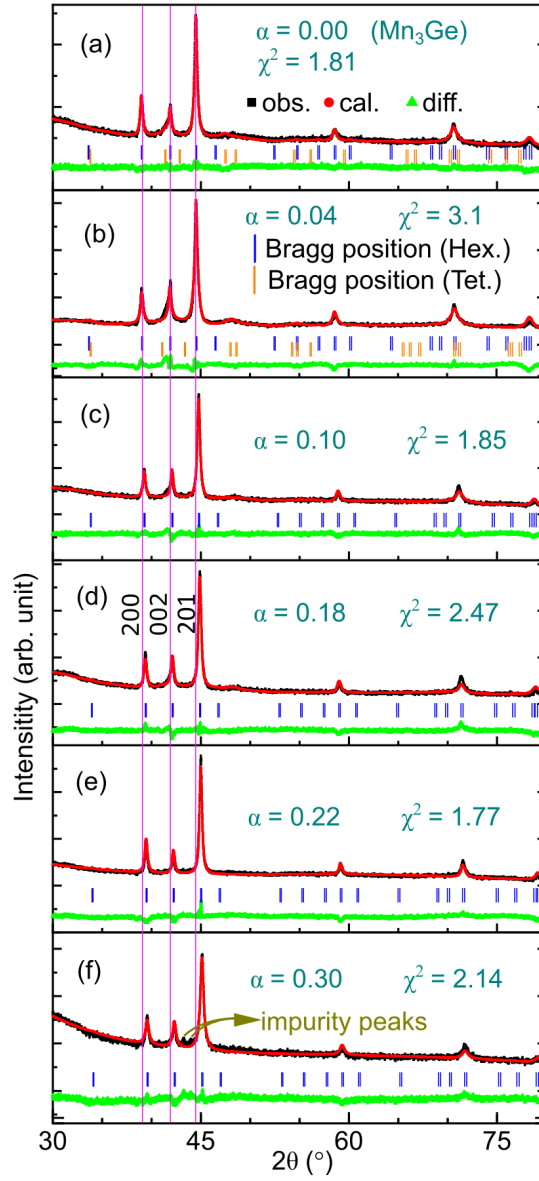


Figure 4.3: (a - f) X-ray powder diffraction of $(\text{Mn}_{1-\alpha}\text{Fe}_\alpha)_{3.2}\text{Ge}$. ‘Hex.’ and ‘Tet.’ refer to the hexagonal and tetragonal phases of the compound, respectively. χ^2 denotes the goodness of the fitting parameter.

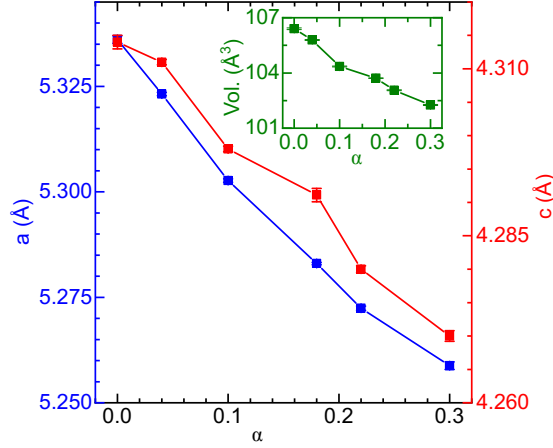


Figure 4.4: Change in the a and c lattice parameters of Hexagonal - $(\text{Mn}_{1-\alpha}\text{Fe}_\alpha)_{3.2}\text{Ge}$ with increase in Fe doping fraction (α) in place of Mn. Inset: change in lattice volume with α .

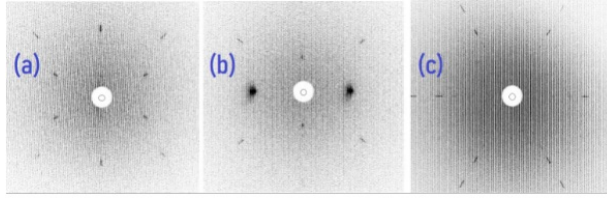


Figure 4.5: Laue diffraction of Mn_3Ge with $P6_3/mmc$ symmetry. (a-c) denote Laue pattern when X-ray beam parallel to x $[2\bar{1}\bar{1}0]$, y $[01\bar{1}0]$, z $[0001]$ axes, respectively.

Since Mn_3Ge and $(\text{Mn}_{0.78}\text{Fe}_{0.22})_{3.2}\text{Ge}$ samples were used for the single crystal neutron diffraction, single crystal X-ray diffraction of both the samples was performed, using the 6-circle SuperNova single crystal diffractometer, to determine the microscopic nature of the crystals. Diffraction patterns corresponding to both samples are shown in the Fig. 4.6. High intensity diffraction spots in the $(hk0)$ plane confirm the high quality of the single crystal with a hexagonal lattice structure, as expected.

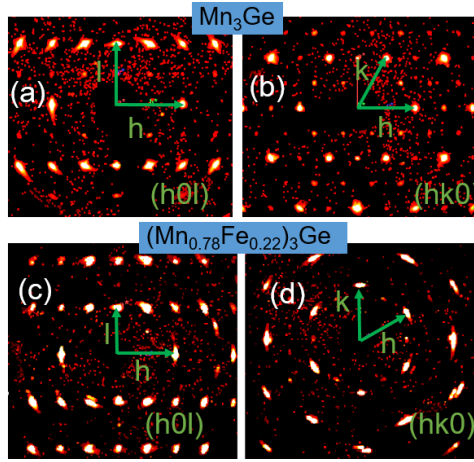


Figure 4.6: SC-XRD corresponding to the $(hk0)$ and $(h0l)$ planes for Mn_3Ge and $(Mn_{0.78}Fe_{0.22})_{3.2}Ge$ with $P6_3/mmc$ symmetry.

5 Magneto-resistance, and electronic transition in Mn_3Ge Weyl semimetal

5.1 Introduction

Topological materials are an extensive topic of research over the last decade because of the observed exotic transport properties. Among them, Weyl semimetals stand out because of the large anomalous transport properties, owing to the non-zero Berry curvature [1, 28, 55, 82, 83, 84]. As described in the chapter 2, the emergence of Weyl points results from the broken time reversal or/and space inversion symmetry. Such type of symmetry requirement is fulfilled by the Hexagonal- Mn_3X family of materials ($X = \text{Sn}, \text{Ge}, \text{Ga}$) [85, 86, 87, 88]. Despite this, the signature of the presence of Weyl points has been observed in the $X = \text{Sn}, \text{Ge}$ only [55, 1, 37]. Hexagonal Mn_3X possess inverse triangular in-plane antiferromagnetism (AFM) [85, 86], along with small ferromagnetic (FM) canting within the plane, which helps in the easy rotation of the Mn spin triangle. Such magnetic features of Mn_3X helps in controlling the chirality of the spin triangle, and lead to the easy rotation of the Mn moments within the plane. Therefore, the anomalous Hall effect (AHE) easily switches its sign within 200 Oersted (Oe) [37] of the applied magnetic field, which results in significantly smaller energy dissipation compared to the FM systems. Therefore, Mn_3X type Weyl semimetals can be very useful for efficient spintronic devices.

Among the Mn_3X family, Mn_3Ge shows a large anomalous Hall effect below the Néel temperature (T_N) of 365 K, down to the 2 K. Other than this, anomalous magneto-optic Kerr effect, anomalous Nernst effect has also been observed in the same temperature regime [56, 57]. However, a clear sign of the chiral anomaly effect has not been established yet.

Since Mn_3Ge has already been predicted to host Weyl points [51], we have measured magneto-resistance (MR) of the Mn_3Ge to observe the chiral anomaly-induced effects. The observation of AHE in a large temperature range makes it a suitable candidate to explore the temperature dependent dynamics of the Weyl points. We have analyzed the longitudinal MR, angular MR, and planar Hall effect below 365 K (Néel temperature), down to the 4 K, along different crystallographic axes using the single crystal- Mn_3Ge . Our analysis shows a few signatures of the chiral anomaly induced effects, which nearly vanishes up to room temperature. In the case of $B \parallel x$, beyond 1.5 T, the chiral anomaly is suppressed and electrical transport effects are dominated by the metallic and semimetallic nature of the compound. The carrier concentration of the compound changes at 190 K, which is near the same temperature where resistivity and high field MR changes sign. These features suggest an electronic transition

in the sample near 200 K. Since the lattice parameter show anomaly near 230 K, the electronic transition is likely to be driven by the lattice parameter of the sample.

5.2 Experimental details

Synthesis and characterization of multiple Mn_3Ge have sample has already been described in the chapter 4. We have used single crystal $\text{Mn}_{3.1}\text{Ge}$ (S1), $\text{Mn}_{3.2}\text{Ge}$ (S2), $\text{Mn}_{3.5}\text{Ge}$ (S3) samples to perform all the experiments. Mostly, S1 and S2 samples were used for the electrical transport measurements because of having similar Mn concentrations as reported by Refs. ([55, 37, 56, 80, 89]).

Neutron diffraction of the S3 sample was performed at FRM II, Garching, using the HEiDi instrument. The technical details of the instrument are mentioned in the chapter 3. The electrical transport measurements were performed using the PPMS and DynaCool setup mentioned in the chapter 3. The measurements were performed along the x, y, z axes, which is defined along the $[2\bar{1}\bar{1}0]$, $[01\bar{1}0]$, and $[0001]$ crystallographic directions, respectively, as mentioned in the Fig. 4.2 (chapter 4).

5.3 Magnetization

The temperature dependent magnetization (M - T) and magnetic field dependent magnetization (M - H) of all the Mn_3Ge samples were measured. Since S1 and S3 have significantly different composition of Mn, M - T , M - H corresponding to these compounds are compared in the Fig. 5.1 and Fig. 5.2, respectively. The M - T data shows that the T_N of the Mn_3Ge is near 365 K, which is the same as the reported by the Refs. [55, 37]. M - T data shows small ferromagnetic (FM) behavior below T_N , which comes from the small in-plane canting of the Mn moments. The M - H data along the x axis also show residual magnetization at zero fields, and it increases almost linearly as the field is increased. The M - H data along the z axis show almost linear behavior. These observations suggest that the Mn moment form AFM structure within the x - y (or a - b plane), along with small FM canting within the plane. The magnitude of FM canting is $20(2) \text{ m}\mu_B/\text{f.u.}$ when the field is applied along the x axis. The residual moment along z axis is below $5 \text{ m}\mu_B/\text{f.u.}$. Above T_N , M - H shows paramagnetic nature of the samples.

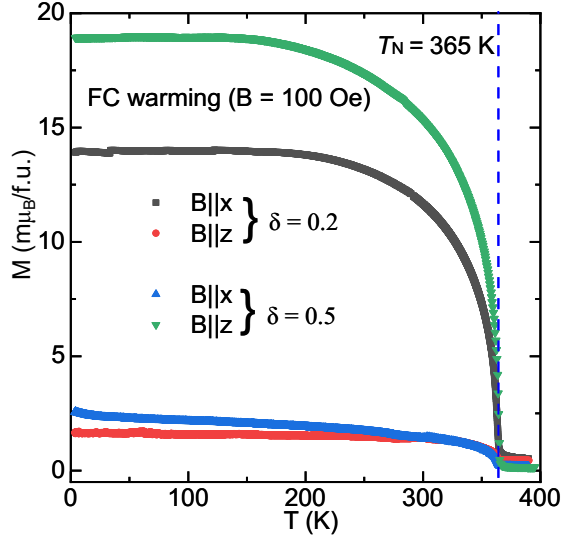


Figure 5.1: Magnetization of the S2 and S3 samples, denoted by $\delta = 0.2$ and $\delta = 0.5$, respectively. The direction of the applied magnetic is mentioned in the plot. The measurement was performed in field cooling (FC) condition under 100 Oe of the applied magnetic field.

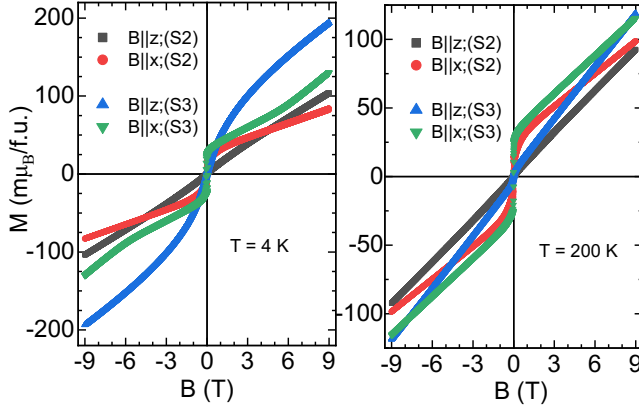


Figure 5.2: Field dependent magnetization of the S2 and S3 samples along various axes mentioned in each plot.

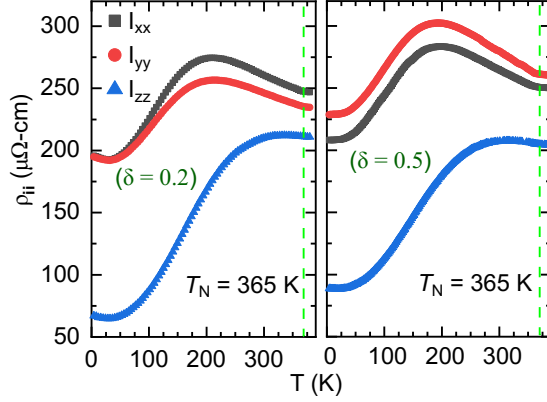


Figure 5.3: Longitudinal resistivity of the Mn_3Ge corresponding to S2 and S3 samples, which are denoted by $\delta = 0.2$ and $\delta = 0.5$, respectively.

5.4 Electrical transport measurements

Electrical transport measurements of the Mn_3Ge were performed using the PPMS and DynaCool setups. Initially, the zero-field longitudinal resistivity of the samples was measured with varying temperatures. The resistivity of the S2 and S3 samples along various axes are compared in the Fig. 5.3. The nature of the resistivity remains very similar for S2 and S3 samples, however, the resistivity of the S3 sample is larger compared to the S2, which is expected because of a larger amount of excess Mn in S3 compared to the S2 sample. Along the x , y axis, the Mn_3Ge shows metallic behavior below 200 K and semimetallic/half metallic behavior above this temperature. For convenience, we will assume our sample to be semimetallic above 200 K. However, it is important to mention that the spin-resolve density of state (DOS) calculations are required to determine whether the sample is half-metallic or semimetallic above 200 K. In contrast to the x axis, resistivity along the z axis remains metallic in below T_N , down to the 2 K, as shown in the Fig. 5.3. The behavior of resistivity of our sample is similar to the Refs. [55, 37].

5.4.1 Longitudinal magneto-resistance

Longitudinal magneto-resistance (LMR) of Mn_3Ge was measured along the different axes. In this scenario, the MR of the compound is measured with the magnetic field applied along the direction of the electric field. Most of the measurements were

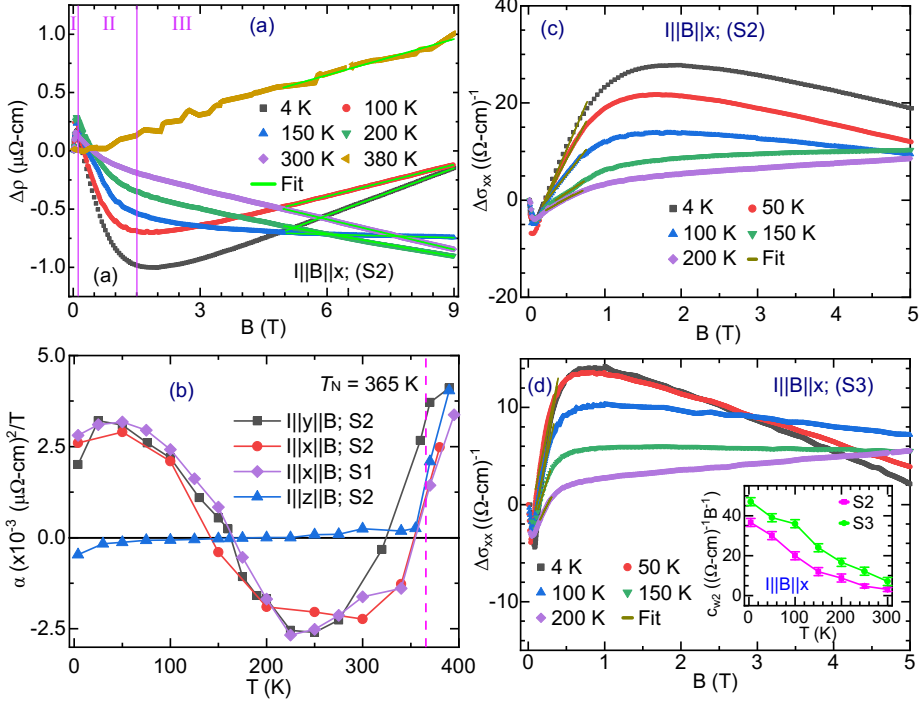


Figure 5.4: (a) shows LMR along the x axis, corresponding to the Mn_3Ge . Here, $\Delta\rho = \rho(B) - \rho(0)$. At high field ($B > 5$ T), the data is fitted with $\rho_{[\text{high } B]} = \alpha(B/\rho_0)$, and fitting is denoted as ‘Fit’. I, II, and III denote three different field regimes where the nature of LMR is different. (b) Temperature dependence of α (high field slope) corresponding to different samples. (c), and (d) show LMC along the x axis, for S2 and S3 samples, respectively. Here, $\Delta\sigma_{ii} = \sigma_{ii}(B) - \sigma_{ii}(0)$. In the case of S2 and S3 samples, LMC below 0.8 T and 0.4 T, respectively, is fitted with $\sigma_{[\text{low } B]} = c_{w2}B$. The evolution of c_{w2} with temperature is shown in (d) inset.

performed using the S2 sample. However, several measurements were repeated for the S1 and S3 samples as well to check the reproducibility of the data. The nature of all the measurements remains very similar for all three samples. The typical dimensions of the samples used are- length:width:thickness = (1.5 - 2.1 mm):(0.4 - 0.5 mm):(0.1 - 0.3 mm).

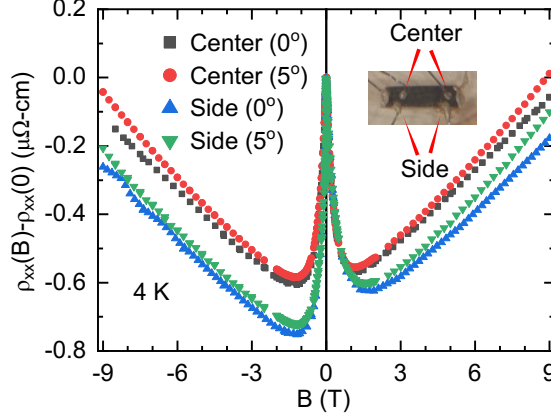


Figure 5.5: LMR corresponding to the S1 sample. Here, ‘Center’ and ‘Side’ denote the voltage measured at the center and side of the sample as shown in the picture. 0°, and 5° denote the mutual angle between the magnetic field and electric current.

The nature of the LMR remained consistent for all the samples when the magnetic field is applied above 0.05 T. The MR ($100 \times \frac{\rho(B) - \rho(0)}{\rho(0)}$) of all the samples remains within 1% along all the axes and temperature regimes, therefore, careful analysis is required to interpret their origin. Since anomalous Hall resistivity near zero fields is nearly 10 times larger than MR, large Hall contributions were observed during the MR measurements. Therefore, most of the collected MR data was symmetrized to obtain the true nature of the MR. As shown in the Fig. 5.6, the LMR along x , y remains very similar at all the temperatures, and most of the analysis is focused on the LMR along the x axis. LMR along the z axis was also measured, which shows significantly different behavior compared with the LMR along the x axis.

Current-jetting effect: As mentioned by the Refs. [40], a sample with large anisotropic MR, and high mobility can lead to the current jetting effect, which may result in the negative LMR if the four-probe wires are not aligned properly. Such phenomena are very prominent in the samples with large MR. To check for the presence of the current

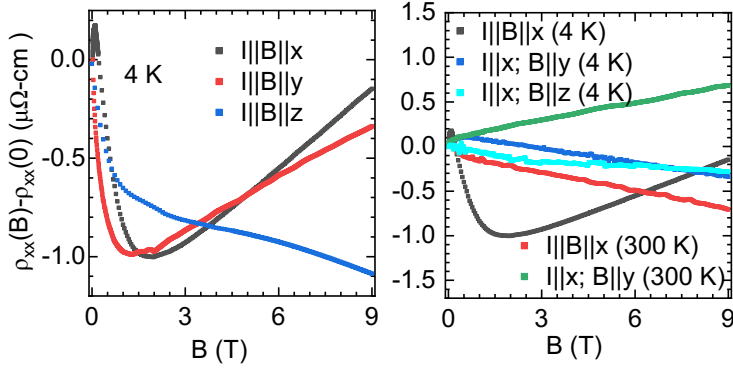


Figure 5.6: MR of Mn_3Ge (S2) at 4 K and 300 K in various combinations of the current and magnetic field as mentioned in the plot.

jetting effect in our sample, we measured the voltage using the different contacts on the sample piece, as shown in the Fig. 5.5(inset). The LMR was measured with tilting of the magnetic field as well. As clearly shown in Fig. 5.5, a negligible difference in LMR was observed in all the cases. Therefore, the effect of the current jetting effect is negligible in Mn_3Ge . This is expected because unlike the samples mentioned by Ref. [40], the resistivity of Mn_3Ge is of the same order of magnitude along all the axes, and the mobility of Mn_3Ge is also very low compared to the samples measured by the [40]. Also, the nature of LMR remains the same for different sample pieces. These observations suggest that the observed LMR has an intrinsic origin.

It is important to mention that magnetization of both the S2 and S3 samples are linear with the magnetic field, however, the LMR shows a drastic change in behavior near 1.5 T. This suggests that the observed non-monotonic LMR is not driven by the magnetization of the sample.

5.4.1.1 LMR along the x or y axis

When LMR is measured along the x axis, it shows non-monotonic behavior up to 9 T, as shown in the Fig. 5.4(a). Initially, the LMR increases up to 0.05 T, at all temperatures. We refer this field regime as region I (shown in Fig. 5.4(a)). Such an increase in LMR was not observed along y and z axis. In the field regime of 0.05 T - 1.5 T (for the S2 sample), referred as region II, the LMR along the x axis decreases with an increase in the magnetic field. Such a decrease in LMR was observed in all the samples, along all the axes. In the case of the S2 and S3 samples, negative LMR

starts to suppress near 1.5 T and 0.8 T respectively, and eventually, LMR starts to increase again at a higher magnetic field, which is referred as region III (Fig. 5.4(a)). Since region II and region III show similar natures for all three samples, their origin has to be intrinsic, which we will discuss below in detail.

LMR in region I: In the case of $I \parallel B \parallel x$, LMR in the region I increases, possibly, due to the weak antilocalization effect (WAL), which is very common in Weyl semimetals. For S1, S2, S3 samples, the magnitude LMR below 0.05 T is $< 0.05 \mu\Omega\text{-cm}$, $\sim 0.3 \mu\Omega\text{-cm}$ and $\sim 0.6 \mu\Omega\text{-cm}$, respectively. Such an increase in magnitude with excess Mn concentration is expected in the case of WAL because of the higher impurity scattering for higher excess Mn concentration.

LMR in region II: LMR in region II shows a sharp decrease for all three samples. We have compared the LMR in region II in the form of longitudinal magnetoconductivity (LMC). The relation between LMC (σ_{xx}) and LMR (ρ_{xx}) can be written as: $\sigma_{xx} = 1/(\rho_{xx})$. LMC corresponding to S2 and S3 sample is shown in the Fig. 5.4(c, d). In both the cases of S2 and S3, LMC increase with field up to 1.5 T and 0.8 T, respectively, and we are referring to this field regime as region II. The LMC in region II can be fitted linearly with $\sigma_{[\text{low } B]} \approx c_{w2}B$, where c_{w2} is the fitting parameter. Since the effect of the current jetting is negligible in our samples, the positive LMC might be driven by the magnetization of the sample or the chiral anomaly effect. We will discuss both possibilities below.

Magnetization: The temperature dependence of c_{w2} , corresponding to both the samples, shown in inset of Fig. 5.4(d). It shows a monotonic decrease with an increase in temperature, unlike magnetization which remains almost constant up to 200 K (Fig. 5.1). The magnitude of LMC for S3 is nearly one-third compared to the S2 sample. However, the magnetization of S2 and S3 and samples remains almost the same in magnitude. These observations strongly suggest that the observed negative LMR in our sample does not originate from the tiny magnetization of the sample.

Chiral anomaly effect: Linear increase of LMC is expected in the case of the type-II Weyl semimetals if LMC is measured along the tilt axis of the Weyl points [90, 82, 27, 46]. Since Mn_3Ge has been predicted to be the type-II Weyl semimetal, similar to the Mn_3Sn [51], the linear increase in LMC in region II suggests its origin to be the chiral anomaly effect. The temperature dependence of c_{w2} (shown in Fig. 5.4(d)), corresponds to both the samples showing a monotonic decrease with an increase in temperature, which is expected as the chiral anomaly weakens at a higher temperature. A similar observation can be made in the case of Mn_3Sn as well [82].

Furthermore, the magnitude of LMC for S3 is nearly one-third of the LMC corresponding to the S2 sample. An increase in Mn concentration increases the chemical potential (μ) of Mn_3Ge [90]. Since LMC due to the chiral anomaly is proportional to the $\frac{1}{\mu^2}$, a drastic decrease in LMC magnitude, for the S3 sample, can be justified as a consequence of the chiral anomaly effect [45, 91, 50]. A similar observation has been made in the case of Mn_3Sn also [82]. These observations suggest the positive LMC in region II is very likely driven by the chiral anomaly effect, similar to the Mn_3Sn [82]. However, further theoretical justification is required to justify the role of the chiral anomaly effect in the observed LMR.

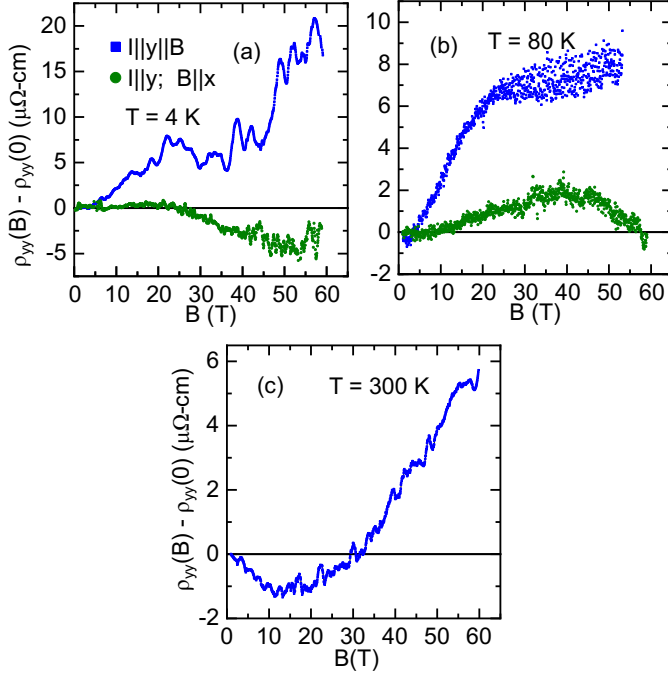


Figure 5.7: (a-c) High magnetic field LMR and transverse MR (TMR) for with current measured along the y axis, and field applied along the x and y axis for LMR and TMR measurement.

LMR in region III: It can be seen in the Fig. 5.4(a), that the LMR at a high field increases linearly with the magnetic field, which is not expected in the case of Weyl semimetals. This suggests that the chiral anomaly in this compound gets suppressed beyond 1.5 T. At high field, the LMR data in Fig. 5.4(a) can be easily fitted with

α ($\rho_{[\text{high } B]} \approx \alpha(B/\rho_0)$). The quantity- α determines the slope of the LMR beyond 5 T. The nature of α corresponding to various measurements using different samples is shown in the Fig. 5.4(b). It can be observed that the α corresponding to LMR along x or y axis is positive at low temperature, which is the opposite of what has been observed in the case of Mn_3Sn [82, 90]. It was also observed that the nature of high α or high field LMR changes near 165 K in all the cases. Sometimes, an external magnetic field can induce a band-gap in the Dirac points [92], which can change the behavior of MR. However, anomalous Hall has been observed up to 9 T, which suggests that the Weyl points in the Mn_3Ge compound remain stable. Therefore, change in LMR near 1.5 is not originated from field-induced electronic transition, as it happens in the case of TaAs [93].

It can be seen from the Fig. 5.3 that the Mn_3Ge is metallic below 200 K, and non-metallic above this temperature. We assume that the sample is semimetallic above 200 K. However, spin-resolved DOS calculations are required to confirm its true nature. Negative and positive MR has been observed in the case of half-metallic/ semimetallic and metallic samples, respectively. Their nature depends on the $3d$ spin density of states [49, 94, 95, 96, 97, 98, 99, 100]. In our case, the high field LMR slope (α) is negative and positive above and below 165 K, respectively (Figs. 5.4(a, b)). At low temperatures, even though LMR is positive at high field, chiral anomaly contribution (leading to the negative LMR) is present here as well. Therefore, the competition between two contributions with opposite behavior leads to the change in the sign the α lower than expected, which is 200 K. Moreover, the sample shows semimetallic and metallic behavior above and below 200 K, respectively (Fig. 5.3). Since the nature of high field, MR and resistivity changes near the same temperature, the origin of high field LMR along the x axis is driven by the semimetallic and metallic nature of Mn_3Ge , above and below ~ 200 K, respectively.

High field MR: We have also measured very high field (60 T) LMR and transverse MR (TMR) of the sample, along the y axis, using the pulsed magnetic field instrument mentioned in the chapter 3. The behavior of LMR along the x axis and y axis are same, as shown in the Fig. 5.6(a). Therefore, MR along the x and y axis can be considered as equivalent. It is important to mention that the high pulsed magnetic field setup is not as sensitive as the DynaCool instrument, which was used to measure MR up to 9 T. Therefore, the negative LMR region below 5 T is not observable during the pulsed magnetic field measurement. It can be seen in the Fig. 5.7 that the LMR

at 4 K and 80 K increases up to 60 T, similar to what we have observed between 1.5 T to 9 T (Fig. 5.4)(a). A change in the slope of LMR and TMR has been observed near 20 T (4 K, 80 K), whose origin is not yet clear. At 300 K, only LMR was measured, and negative to positive change in MR was observed. Here, the negative MR is possibly due to the semimetallic nature of the sample, and positive LMR at a higher field is due to the trivial MR which is known to be increasing for any system because of the Lorentz force.

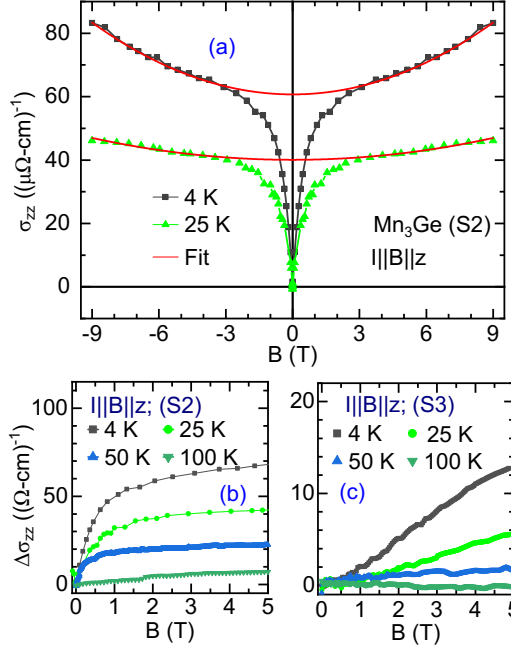


Figure 5.8: (a) LMC along the z axis. The data at high field ($B > 3$ T) is fitted (fit) with $a_0 + a_1 B^2$, where a_0 and a_1 are the fitting parameters. (b, c) LMC corresponding to the S2 and S3 samples, with the magnetic field applied along the z axis.

5.4.1.2 LMC along the z axis

LMC along the z axis also show sharp increase in the same field regime, as shown in the Fig. 5.8, similar to the Ref. [90]. However, LMC along the z axis remains increasing up to 9 T. The low field linear increase is possibly due to the magnetic domain effect because it takes a definite field strength to align the domain population

along the magnetic field [90]. The domain effect may be present, at low field, in the case of LMC along the x axis as well, which leads to the enhanced observation of the positive LMC, compared to positive LMC contribution solely due to the chiral anomaly effect. At high field ($B > 3$ T), the LMC along the z axis follows B^2 magnetic field dependence at the 4 K (Fig. 5.8(a)). As mentioned in the last section, the tilt of the Weyl points is likely towards the x axis, therefore, B^2 magnetic field dependence of the LMC along z axis is expected in the case of chiral anomaly effect [9]. As shown in the Fig. 5.8, the B^2 field dependence weakens, significantly, as the temperature is increased to 25 K. The LMC decreases with temperature, and almost vanished near 100 K. These observations are expected in the case of chiral anomaly effect, as it weakens significantly with an increase in temperature, due to the occupancy of the higher Landau levels. The magnitude of LMC corresponding to the S3 sample (higher Mn concentration) is nearly five times smaller than LMC for the S2 sample (lower Mn concentration), similar to the LMC along the x axis. As mentioned previously, LMC due to the chiral anomaly is proportional to the $\frac{1}{\mu^2}$, which leads to a significant decrease in the LMC magnitude if chemical potential increases (due to an increase in Mn concentration for S3 sample) Therefore, the significantly small magnitude of LMC for S3 sample, compared to the S2 sample, suggest the origin of LMC along the z axis to be the chiral anomaly effect.

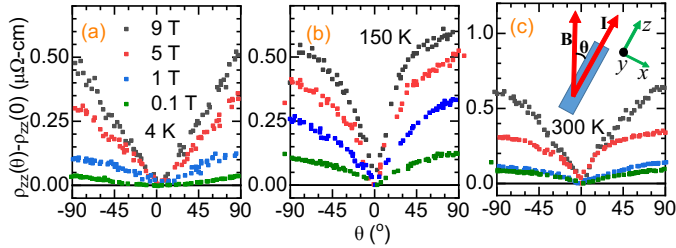


Figure 5.9: (a-c) θ MR corresponding to the $I \parallel B \parallel x$; B rotated from z to x axis. The experimental setup is illustrated in (c).

5.4.2 Angular magneto-resistance

Angle (θ) dependent MR (θ MR) of Mn_3Ge (S2) was measured along different axes while rotating the sample in various possible planes. The nature of θ MR can be guessed from Fig. 5.6, where it is clear that the nature of θ MR, defined as $= \rho_{\perp} - \rho_{\parallel}$, should be positive in most of the cases, and the same has been observed during the

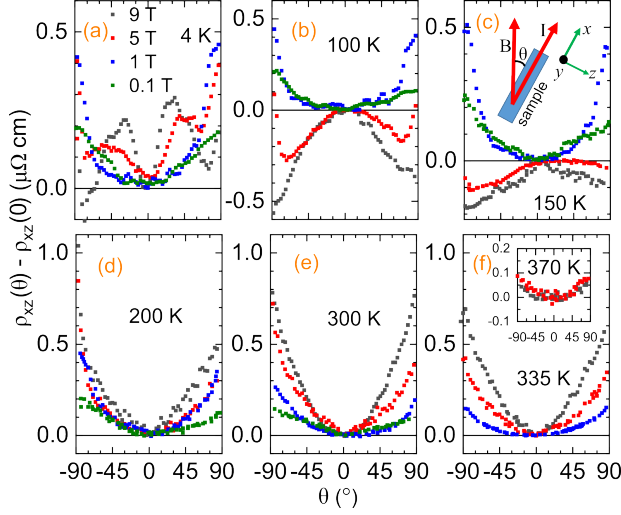


Figure 5.10: (a-f) denote θMR corresponding for $I \parallel B \parallel z$; B rotated from x to the z axis. The experimental setup is illustrated in (c). (f) Inset: θMR at 370 K, which is above the T_N .

θMR measurements as well. The measurements were performed while rotating the sample in x - z and x - y planes. We will discuss both cases below.

First of all, the θMR was measured in the x - z plane, with current applied along the z and x axis. As observed in Figs. (5.9, 5.10), positive θMR is present in the case of $B \parallel I \parallel z$; B rotation from z to x , and $B \parallel I \parallel x$; B rotation from x to z . In the former case, the θMR increases with the magnetic field, however, it remains nearly the same in magnitude at 4 K and 300 K. In contrast to this, θMR behaves non-monotonically with temperature and field in the latter case when θMR is measured with current applied along the x axis. Different θMR behavior within the sample plane suggests that the θMR within x - z plane does not originate from the chiral anomaly effect. Furthermore, LMC along the z axis almost vanishes beyond 100 K, in contrast with θMR which remains significantly large up to room temperature. Therefore, it is certain that the θMR in x - z does not result from the chiral anomaly effect. Such a different behavior θMR within the x - z plane, could be observed due to the magnetic anisotropy within this plane.

Further, θMR was measured in the x - y plane. The measurements were done for $B \parallel I \parallel y$; B rotated from y to x , and $B \parallel I \parallel x$; B rotated from x to y , as shown in the Fig. 5.11 and Fig 5.12(a-f). It can be observed that the behavior of θMR in x - y plane

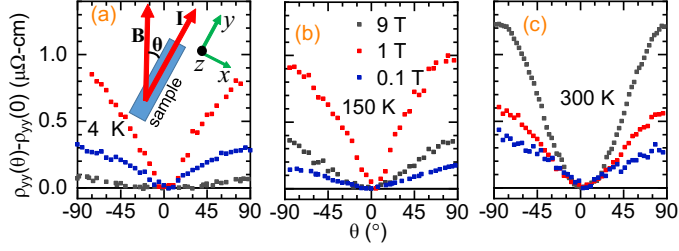


Figure 5.11: (a-c) denote θMR corresponding to the $I\parallel B\parallel y$; B rotated from y to the x axis. The experimental setup is illustrated in (a).

remains almost the same when the current is applied along the x axis and the y axis. Therefore, θMR in this plane may arise from the chiral anomaly effect, which solely depends on the angle between the magnetic field and the electric current direction.

We have analyzed the θMR for $B\parallel I\parallel x$; B rotation from x to y measurement in detail. In this case, positive θMR is observed in all the cases. The evolution of magnitude of θMR with temperature is shown in the Fig. 5.12(g). The magnitude of θMR , at 9 T, increases with an increase in temperature up to 200 K and starts to decrease further. However, in the case of chiral anomaly, θMR is expected to decrease as $a - bT^m$ [101], where a , b are fitting parameters. In contrast to 9 T, θMR at 1 T decreases monotonically with temperature, and $m = 2.3(2)$ was obtained, which is slightly higher than other Weyl semimetals, as obtained by the Ref. [101]. These observations suggest that the θMR *only* at 1 T possibly originates from the chiral anomaly effect, which is justified because LMR along the x axis, below 1.5 T, originates from the chiral anomaly effect.

Field dependence of the magnitude of θMR is shown in Fig. 5.12(h). θMR at 4 K increases with field up to 1.5 T and decreases at higher field. In contrast to this, θMR at 300 K increases linearly up to 9 T. These observations, in combination with LMR along the x axis, suggesting that the θMR , at 4 K, is induced by the chiral anomaly effect up to 1.5 T only. θMR at 300 K is larger than 4 K. However, the chiral anomaly effect is very weak at room temperature compared to the 4 K. This suggests that the θMR at 300 K does not originate from the chiral anomaly effect. Furthermore, the non-monotonic field dependent behavior of θMR at different temperatures suggests that θMR does not originate from the magnetization of the sample.

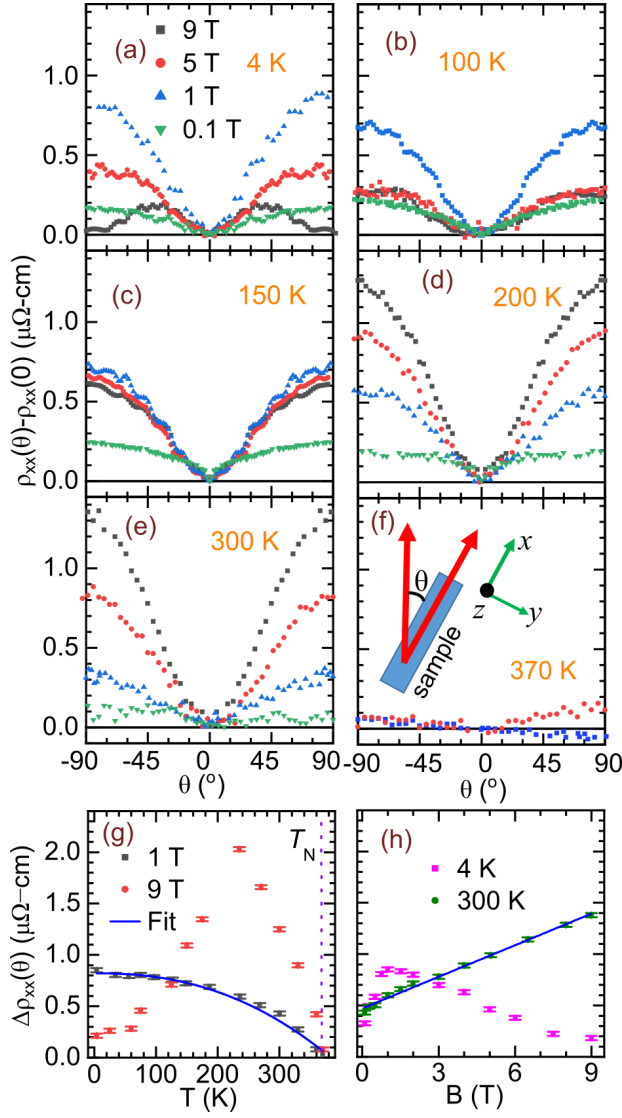


Figure 5.12: (a-f) denote θMR corresponding to the $I\parallel B\parallel x$; B rotated from x to y axis, for Mn_3Ge (S2) sample. (g, h) show temperature and magnetic field dependence of θMR oscillations. $\Delta\rho_{xx} = \rho(\theta_{\max}) - \rho(0)$, where θ_{\max} means θ at which the maximum magnitude of oscillation is observed.

5.4.3 Analysis of high field θ MR

As explained by the Refs. [99, 102], the difference in up and down the spin density of states (DOS) can lead to the negative or positive nature of the θ MR. The same has been observed by Refs. [49, 100]. We will denote the component of θ MR, induced by the unequal spin DOS, as θMR_s . Since Mn_3Ge is metallic below 200 K, θMR_s should show negative ($\rho_{\perp} < \rho_{\parallel}$) behavior below 200 K. Whereas, chiral anomaly induced θ MR ($\text{MR}\theta_{ch}$) show positive θ MR ($\rho_{\perp} > \rho_{\parallel}$) [46, 91, 43]. On the basis of the temperature and field dependent θ MR, it can be argued that at low temperature (at 4 K), $\text{MR}\theta_{ch}$ and θMR_s compete with each other, such that $\text{MR}\theta_{ch}$, θMR_s dominate below and above 1.5 T, respectively. Therefore, θ MR increase up to 1.5 T and decreases beyond this field (Fig. 5.12(h)). The observed θ MR is the resultant of the $\text{MR}\theta_{ch}$ and θMR_s , and both are opposite below 200 K. Therefore, an increase in θ MR magnitude, at 9 T, up to 200 K, is possible, if the strength of $\text{MR}\theta_{ch}$ and θMR_s decreases with increase in temperature at different rates (Fig. 5.12(g)).

For $T > 200$ K, the sample show semimetallic behavior. Therefore, θMR_s should be positive, similar to the behavior of chiral anomaly induced θ MR. Also, the chiral anomaly is significantly weak at high temperatures. Therefore, the linear (field dependent) increase in the magnitude of θ MR (at 300 K) originates from the semimetallic nature of the sample.

5.4.4 Anomalous Hall effect

Hall resistivity of different samples was measured with the magnetic field applied along the different axes, as shown in the Fig. 5.13(a-d). We will denote Hall resistivity as ρ_{ij} , where i, j implies the axes along which current and voltage are measured while applying the magnetic field normal to both axes. The residual Hall resistivity at $B = 0$ is known as anomalous Hall resistivity (AHR). AHR can be measure by the high field Hall resistivity data (linear) fitting, as shown in the Fig. 5.13(a) (denoted as ρ_{xz}^A). Large AHR was observed in the case of $B \parallel (x, y)$. Beyond 1 T, linear field dependence is observed in all the Hall resistivity measurements as shown in the Fig. 5.13.

AHR can be observed as long as an internal magnetic field is present inside the system, as happens in the case of FM systems [34, 103]. However, in the case of Weyl semimetals, the non-zero Berry curvature act as a fictitious magnetic field inside the system, leading to the anomalous Hall effect (AHE), which generates AHR. Total Hall resistivity can be given as: $\rho_{ij} = R_s M + R_B B + \rho_{ij}^A$. The first component denotes Hall

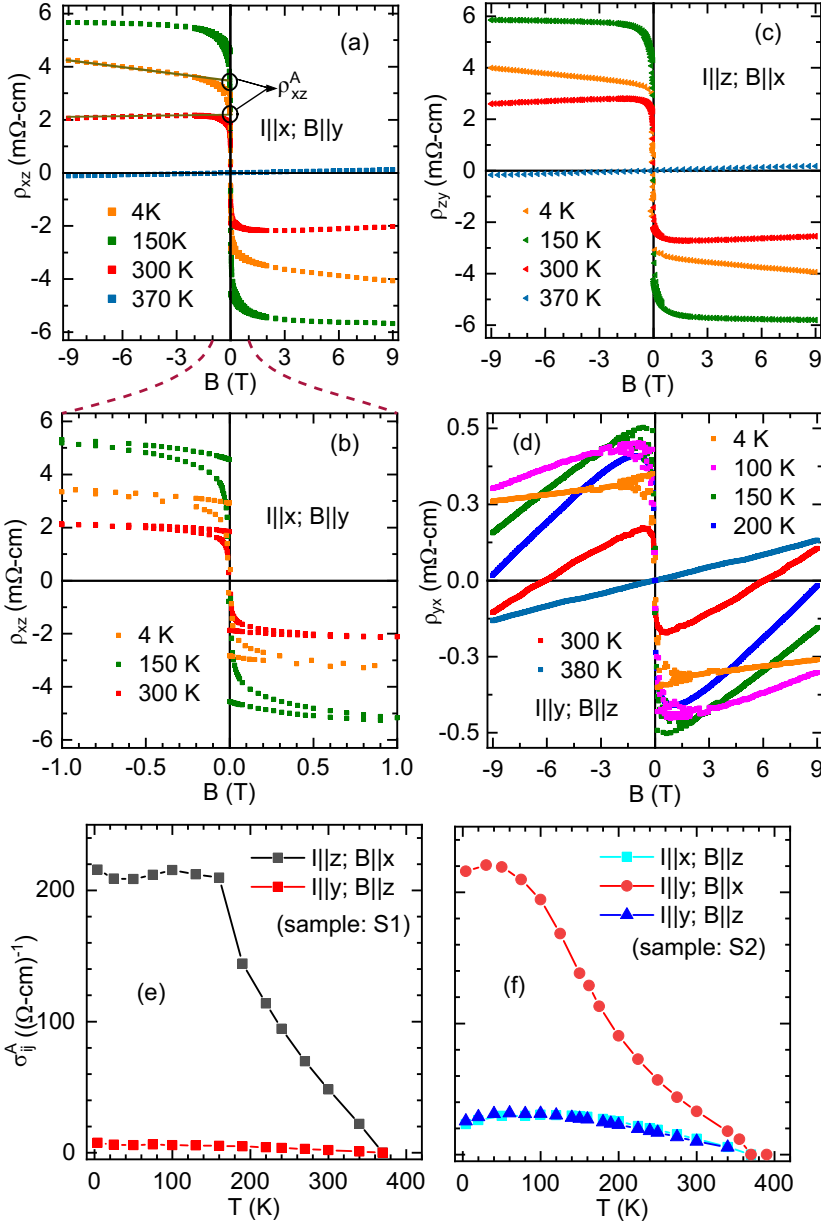


Figure 5.13: (a-d) denote field dependence of Hall resistivity with the magnetic field applied along the different axis mentioned in each plot. The straight line in (a) shows the linear fitting of the Hall resistivity in the field range of -9 T to -3 T, and the y axis intercept (ρ_{xz}^A) is known as the anomalous Hall resistivity. (e), (f) show the temperature dependence of anomalous Hall conductivity (σ_{ij}^A) for S1 and S2 samples, respectively.

resistivity due to the magnetization (M) of the sample [34]. The second component shows normal Hall resistivity which is proportional to the applied magnetic field. The last term ρ_{ij}^A denotes AHR due to the Non-zero Berry curvature in Weyl semimetals. It is important to note that the nature of AHR in Fig. 5.13 is completely different from the field dependent magnetization of the sample (Fig. 5.2). Therefore, the observed AHR certainly results from the Weyl semimetallic nature of the sample, as justified by the Refs. [55, 37] as well.

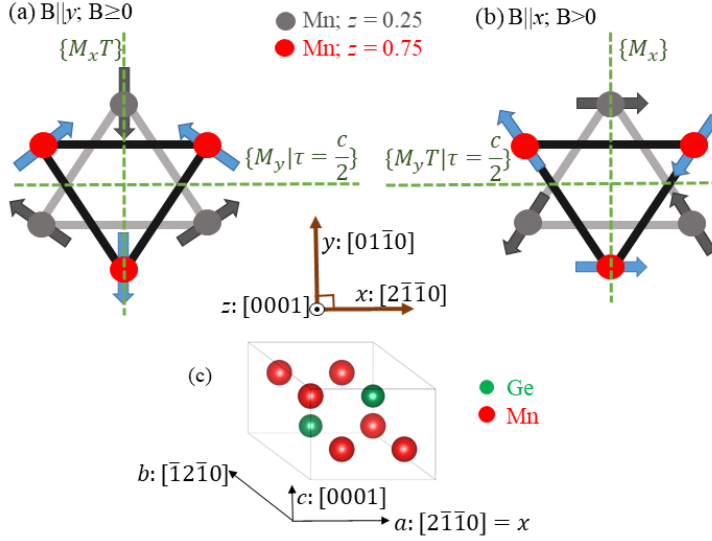


Figure 5.14: (a) denote magnetic structure when $B \parallel y$ is applied, or $B = 0$. (b) correspond to the magnetic structure when $B \parallel x$ is applied. [87, 88]. Green dashed lines illustrates symmetry planes, where M_x , M_y implies mirror-plane in x - z and y - z planes, respectively. T corresponds to the time-reversal symmetry. $\tau = \frac{c}{2}$ means the translation along the c axis (or z axis) by $\frac{c}{2}$. (c) shows lattice structure of Hexagonal - Mn_3Ge .

Since the anomalous Hall conductivity (AHC) is directly linked with the Berry curvature, we have compared various AHR in terms of the AHC. AHC (denoted as σ_{ij}^A) can be determined using the AHR (ρ_{ij}^A), as ($\sigma_{ij}^A \approx \frac{-\rho_{ij}^A}{\rho_{ii}\rho_{jj}}$). Where, ρ_{ii} denote normal resistivity along the i axis. The temperature dependence of AHC ($\sigma_{ij}^A(T)$) for various combinations, corresponding to S1 and S2 samples, are shown in the Fig. 5.13(e, f). The nature of $\sigma_{ij}^A(T)$ remains almost same for both the samples. AHC is significantly large as long as the field is approaching to zero along x or y axis. As

shown in the Fig. 5.13(e, f), AHC along the x axes remains almost the same up to 160 K and 80 K in the case of S1 and S2 samples, respectively. Weaker AHC for the S2 sample compared to the S1 sample is reasonable since Weyl points move away from the Fermi surface as Mn concentration increases [90]. A similar observation has been made by Refs. [37, 90]. Small AHC for $B\parallel z$ results from the misalignment of the sample, such that a small component of the field along the x or y axis as well, which gives small AHR along the z axis as well.

The non-zero Berry curvature in Mn_3Ge is linked with the in-plane magnetic symmetry of the sample. Mn_3Ge possesses an in-plane AFM structure, where Mn moments align in a reverse triangular structure. They also possess small FM canting within the plane, leading to the tiny residual magnetization as observed in the Fig. 5.2. Due to the presence of a small FM moment, the Mn spin triangle can be rotated very easily within the a - b plane. Therefore, the chirality of the spin triangle can be reversed within the ~ 200 Oe of the external magnetic field, as can be seen in the Fig. 5.13(b). Field-dependent neutron diffraction by Refs. [88, 87] shows that the magnetic structure of Mn_3Ge changes within the plane, depending on the direction of the magnetic field. The magnetic structure when magnetic field applied along the y and x axes are shown in the Fig. 5.14(a, b), respectively. The magnetic structure in the absence of a magnetic field remains the same as Fig. 5.14(a). In the case of $B\parallel x$, and $B\parallel y$, a mirror plane exist, as shown in the Fig. 5.14, which are denoted as M_x and M_y , respectively. Mirror reflection retains the Berry curvature but reverses the chirality. This leads to the non-zero Berry curvature, Ω^y , and Ω^x in case of $B\parallel y$ and $B\parallel x$, respectively. Therefore, the observation of large AHR in Mn_3Ge is justified due to the presence of the large Berry curvature, as long as the magnetic field is applied along the x or y axis. The Berry curvature along the z axis (Ω^z) vanishes due to the symmetry. Therefore AHR is not expected when the field is applied along the z axis. This also justifies that the observed AHR in the case of $B\parallel z$ may result from the slight misalignment of the sample, leading to a small contribution from ρ_{xz}^A or ρ_{zy}^A .

At a high field, Hall resistivity increases linearly with the magnetic field. In the case of $B\parallel z$ axis, the single-band model fit gives the approximate carrier concentration to be $\sim 10^{21}/\text{cm}^3$, which is nearly 10 times lower than obtained by Ref. [89] for the same compound. This possible difference could arise due to the different Mn composition, and different sample preparation techniques. The Hall coefficient (R_H) can be calculated as $R_H \approx \frac{\partial \rho_{ij}}{\partial B}$, which gives information about the dominant carrier concentration of the sample. R_H corresponding to the different samples, with field

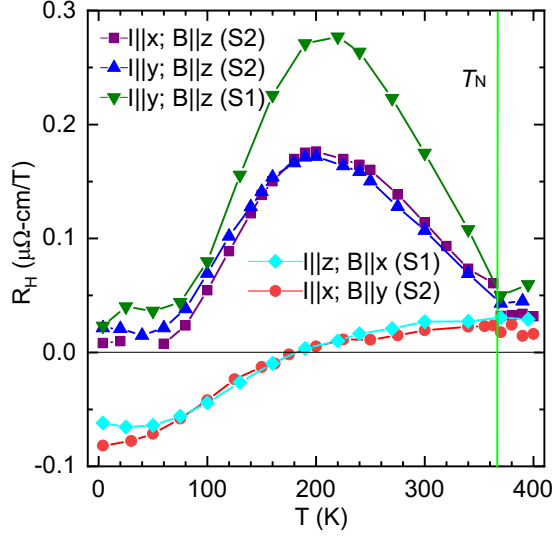


Figure 5.15: Temperature dependence of Hall coefficient (R_H) for different samples, under different conditions.

applied along different axes, is shown in the Fig. 5.15. It can be observed that the R_H remains positive when the field is applied along the z axis, and it shows a maximum near 200 K. However, R_H changes sign near 200 K in the case when the field is applied along the x or y axis. These observations suggest that Mn_3Ge possesses a hole (electron) as the dominant carrier concentration below (above) ~ 190 K. This observation is very similar to the Ref. [104], where an electron-hole transition is observed in the thin film Mn_3Ge sample. Therefore, we can conclude that single-crystal Mn_3Ge also goes through an electronic phase transition near 190 K, which is near the same temperature where the metal-semimetal transition is observed in the resistivity measurement (Fig. 5.3). These observations suggest that the metallic-semimetallic transition and change in carrier concentration are intimately connected, which is reasonable as both the effects are results from the electronic band structure and DOS of the compound. It also strengthens our previous claim that the Mn_3Ge goes through an electronic (topological) transition near 200 K. Similar electronic topological transition has been observed (at 50 K though) in the case of thin film Mn_3Ge as well [104].

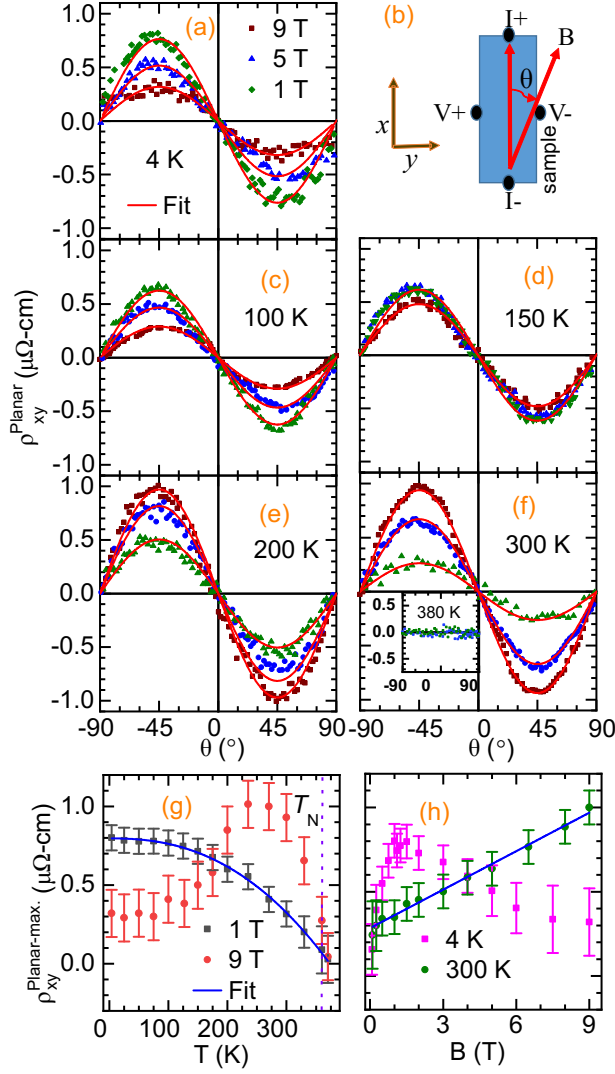


Figure 5.16: (a, c - f) corresponds to the PHE for Mn_3Ge (S2) sample. The measurement setup is illustrated in (b). (g, h) show temperature and magnetic field dependence of PHE oscillations. $\rho_{xy}^{\text{Planar-max.}} = \rho_{xy}^{\text{Planar}}(-45^\circ) - \rho_{xy}^{\text{Planar}}(0)$.

5.4.5 Planar Hall effect

The planar Hall effect (PHE) of the sample of Mn_3Ge (S2) was measured with the sample rotated within the sample plane. In such cases, transverse/Hall voltage is not expected in normal antiferromagnetic metals, however, oscillations are observed in the case of any Weyl semimetals. PHE was measured in the x - y plane, and clear sinusoidal oscillations are observed, as shown in the Fig. 5.16. In the case of chiral anomaly induced PHE, it can be fitted with the following equation [46, 43]:

$$\rho_{ij}^{\text{PHE}}(\theta) = -\Delta\rho_{ii}\left(\frac{\sin 2\theta}{2}\right); \Delta\rho_{ii} = \rho_{\perp} - \rho_{\parallel} \quad (5.1)$$

It is interesting to observe that the magnitude of PHE is determined by the the magnitude of the LMR at the given field. The observed PHE were fitted with the above equation as shown in the same plot (Fig. 5.16). The magnitude of PHE oscillations is analyzed in the Fig. 5.16(g, h). The magnitude of PHE behaves non-monotonically with the temperature and magnetic field, similar to the θMR . The temperature and field dependence of (chiral anomaly originated) PHE is expected to behave similarly to the θMR [9, 43, 91]. The PHE magnitude decreases monotonically with the temperature at 1 T, which can be fitted with the formula mentioned in the θMR section ($a - bT^m$), and $m = 2.3(1)$ was obtained, which is nearly the same as observed for the θMR . The temperature dependence of PHE, at 4 K, remains non-monotonic at 9 T, similar to the θMR . The magnitude of PHE at all the temperatures and field range varies similar to the θMR data, which suggest their common origin. Since PHE is the direct consequence of anisotropic angular MR [48], the origin of PHE at various temperatures and magnetic field remains the same as the θMR . Therefore, here again, we can argue that the PHE below 1.5 T originates from the chiral anomaly effect. However, large PHE at high field and high temperatures are the consequence of the metallic and semimetallic nature of the sample, below and above 200 K, respectively.

5.5 Single crystal neutron diffraction

Since the existence of Weyl fermions owe to the underlying symmetry of the system, ground state magnetic structure plays a very important role. We have observed a change in MR near 200 K, therefore it is very important to carefully analyze the magnetic structure at various temperatures looking for the possible change in magnetic structure or magnetic moment of the sample below and above 200 K. For this

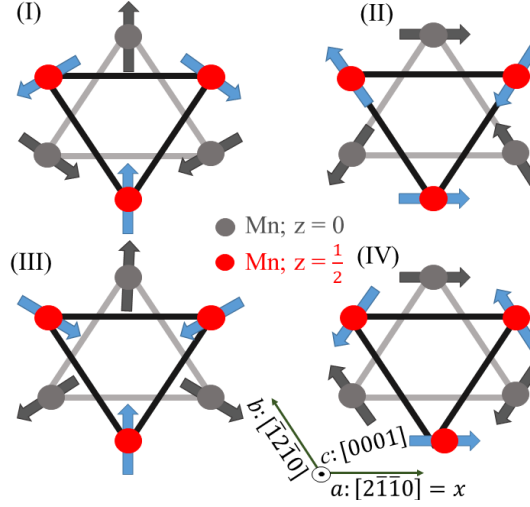


Figure 5.17: Various possible magnetic models of Mn_3Ge , based on the magnetization of the sample. In the case of (I, III) models, moments lie towards the $[01\bar{1}0]$, and in (II, IV) moments are along the $[2\bar{1}\bar{1}0]$ axis.

purpose, we performed single-crystal neutron diffraction of Mn_3Ge (S3) sample at 4 K, 175 K, and 300 K, using the HEiDi instrument mentioned in the chapter 3. The propagation vector $\mathbf{k} = 0$ for the Hexagonal phase of Mn_3Ge [86, 87, 52], Therefore magnetic and nuclear reflections coincide at the same scattering vector (Q). However, magnetic reflections becomes insignificant at high Q ($= \sin \theta / \lambda$) but nuclear reflections remain strong. Therefore, nuclear parameters were analyzed using the high Q data ($0.7 > Q > 0.4$), with the help of JANA2006 software [105]. Analysis has clearly shown that the crystal synthesizes with $P6_3/mmc$ hexagonal symmetry, as determined by the X-ray diffraction analysis mentioned in chapter 4. The neutron diffraction analysis shows that Mn and Ge occupy $6h$ and $2c$ Wyckoff positions, respectively. Also, the analysis provides clear evidence that the excess Mn occupies the Ge site ($2c$ Wyckoff site). The chemical formula determined by the neutron diffraction analysis is $\text{Mn}_3(\text{Mn}_{[0.09(1)]}\text{Ge}_{[1-0.09(1)]})$, which is equivalent to the $\text{Mn}_{3.4(6)}\text{Ge}$, slightly lower than the chemical composition determined by the ICP-OES method ($\text{Mn}_{3.55(5)}\text{Ge}$).

Further, the nuclear parameters determined at high Q were used to analyze the low Q data to determine the magnetic parameters. The representation analysis corresponding to $P6_3/mmc$ space group with $\mathbf{k} = 0$ gives total 18 basis vectors, implying 18 different type of possible magnetic structures. Several of them can be rejected

Table 5.1: Refinement result of the neutron diffraction analysis. The goodness of the fitting parameter (χ^2) at different temperatures, corresponding to different models.

Temperature	4 K	175 K	300 K
χ^2 (model I)	1.82	1.35	1.79
χ^2 (model II)	1.82	1.35	1.79
χ^2 (model III)	4.18	3.43	2.58
χ^2 (model IV)	3.95	3.31	2.4

Table 5.2: Refined parameters determined after the neutron diffraction data refinement, using the magnetic model I.

Temperature	4 K	175 K	300 K
Moment	2.15(8)	2.01(7)	1.68(9)
χ^2	1.82	1.35	1.79
R	2.76	2.32	2.37
R^w	3.15	2.53	3.22
$U_{\text{iso}}[\text{Mn}]$	0.0036(2)	0.0058(1)	0.0082(3)
$U_{\text{iso}}[\text{Ge}]$	0.0014(2)	0.0031(2)	0.0050(2)
Domain ratio	55:35:10	50:35:15	52:42:6
No. of reflections	229	165	175

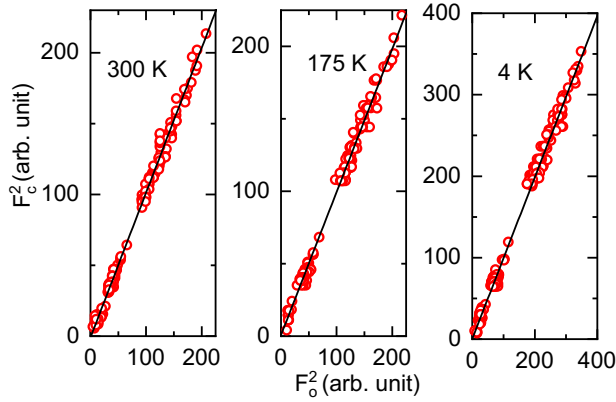


Figure 5.18: Calculated vs. observed intensity corresponding to model I, at different temperatures. F_c^2 , and F_o^2 denote calculated and observed intensities, respectively.

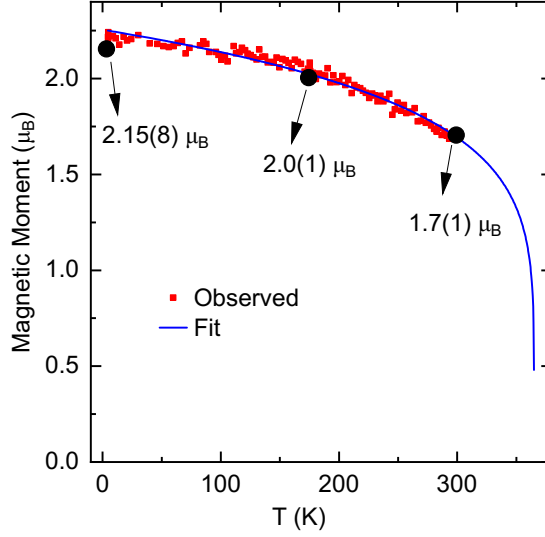


Figure 5.19: Evolution of the magnetic moment with temperature. Black dots represent the magnetic moment determined by the data fitting at 4 K, 175 K, and 300 K. The data (red dots) follows the blue curve (Fit), which corresponds to the equation: $\mu(T) = \mu_0(1 - T/T_N)^\beta$, where $\beta = 0.16(1)$.

as they do not fulfill the conditions demanded by the magnetization of the sample. Finally, 4 magnetic models (shown in Fig. 5.17) were selected which can comply with the magnetization of the sample. All four magnetic models were fitted at all the temperatures, and the corresponding goodness of the fitting parameter (χ^2) is mentioned in the Table 5.1. During the fitting, the possibility of unequal (120°) domains was also considered. It was interesting to observe that the data fits best with model I and model II at all three temperatures. As suspected, the χ^2 corresponding to model I and model II remains the same, as suggested by the Ref. [53] as well. Models I and II remain the best fit at all three temperatures, and Ref. [52] has determined the magnetic structure of Mn_3Ge to be model I. Therefore, we can conclude that the ground magnetic state of Mn_3Ge remains the same at all three measured temperatures. The calculated vs observed intensity for model I, at all the temperatures, is shown in the Fig. 5.18. Various fitting parameters are mentioned in the Table 5.2.

The evolution of magnetic moment with temperature was determined by collecting the (1 0 1) peak starting from 4 K to 300 K. The intensity was normalized with the magnetic moment and plotted in the Fig. 5.19, illustrating the variation of mag-

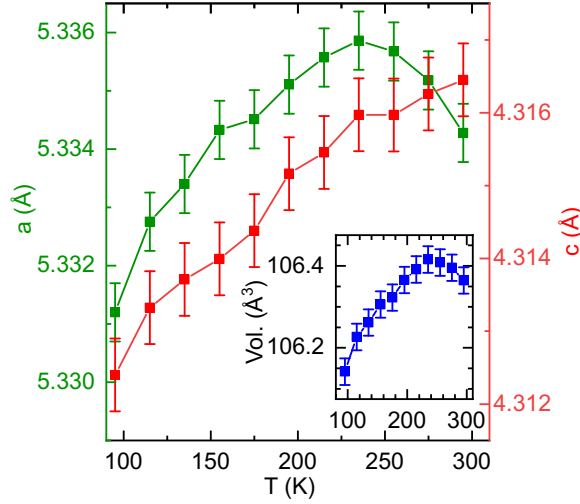


Figure 5.20: Temperature dependence of the lattice parameters determined by the X-ray powder diffraction analysis. Inset: Evolution of the lattice volume with temperature.

netic moment with temperature. It can be observed that the Mn moments vary smoothly with temperature, without any anomaly near 200 K. Temperature dependent magnetic moment ($\mu(T)$) follows power law of the form $\mu(T) \approx \mu_o(1 - \frac{T}{T_N})^\beta$, with $\beta = 0.16(1)$. Here β is an exponent, and μ_o is the maximum possible magnetic moment at $T = 0$, which is $2.5 \mu_B$.

Neutron diffraction analysis concluded that the Mn_3Ge does not possess any anomaly in the magnetic structure or the magnetic moment around 200 K. Therefore the observed change in MR behavior near 200 K is not explicitly linked with the magnetic parameters of the sample. Further, we performed temperature dependent X-ray powder diffraction of the sample in the temperature range of 100 K - 300 K. The evolution of lattice parameters and volume is shown in the Fig. 5.20. Interestingly, a lattice parameter shows a maximum near 230 K, which is unusual for any normal metallic sample. A similar observation has been made by the Refs. [106, 107] also. Since we observed the metal-semimetal transition near 200 K, which is slightly below 230 K, it can be argued that the onset of the electronic (topological) transition is driven by the characteristic of a lattice parameter of the sample.

5.6 Conclusion

The electrical and magnetic transport properties of three different Mn_3Ge samples remain almost the same. LMR measurements have clearly shown negative behavior in various cases. The analysis of LMR in terms of conductivity suggests that the observed positive LMC (below 1.5 T for x axis, and up to 9 T for z axis) is very likely to be originated from the chiral anomaly effect. A similar conclusion is made based on θMR data analysis as well. It is observed that the chiral anomaly effect weakens, significantly, with the increase in temperature, and increase in Mn concentration as well. In the case of LMR (along the x axis), and θMR (within x - y plane), the chiral anomaly is suppressed beyond 1.5 T, as LMR and θMR behavior does not follow the characteristics of chiral anomaly. However, the temperature dependence of high field MR and θMR show similarities with the resistivity and R_H of the sample, as they change their nature near 200 K. These observations suggest that the high field MR results from the metallic/semimetallic nature of the sample. Carrier concentrations also change near 200 K, suggesting its intimate connection with the metallic-semimetallic nature of the sample. These observations suggest that Mn_3Ge goes through an electronic (topological) transition near 200 K. Furthermore, neutron diffraction analysis did not show any anomaly in the magnetic characteristics of the sample, however, ‘ a ’ lattice parameter of the sample shows a maximum near 230 K. Therefore, it can be argued that the electron transition in Mn_3Ge , near 200 K, is driven by the change in its lattice parameter.

6 Magnetic structure of (Mn_{0.78}Fe_{0.22})_{3.2}Ge using Neutron diffraction measurements

6.1 Introduction

Anomalous transport effects in Weyl semimetals have gained enormous attention due to their robust nature and topological origin. The anomalous Hall effect (AHE) gains special attention as it provides a measure of the intrinsic magnetic field present inside the compound. Large AHE can be observed in the Ferromagnetic materials [34, 103, 108]. However, they come with a large hysteresis in each cycle, which makes them a non-ideal case for spintronic applications due to the heat loss in every cycle. Search for the efficient spintronic devices has given the scientific community an optimism after the discovery to antiferromagnetic Weyl semimetals - Mn_3X ($X = \text{Ge}, \text{Sn}$) [82, 55].

Hexagonal- Mn_3Ge possesses co-planar, non-collinear antiferromagnetic (AFM) structure [52], with broken time-reversal symmetry [55]. Among the several Weyl semimetals, Mn_3Ge shows large AHE starting from 2 K, up to 360 K. This makes it one of the best candidates for spintronic applications. The intrinsic magnetic field in Mn_3Ge can be as large as 200 T, due to the presence of large Berry curvature. The recent discovery of singlet to triplet spin-polarized cooper pairs in thin film Mn_3Ge [109] is one experimental evidence that the presence of an intrinsic magnetic field can be utilized for different purposes.

For an efficient application of Weyl semimetals, it is very important to know the parameters which can tune the Weyl points and resulting transport effects. However, the underlying physics behind the characteristics of the Weyl points, in magnetic Weyl semimetal, is not yet clearly established. In the case of Hexagonal- $\text{Mn}_{3+\delta}\text{Ge}$, the anomalous Hall effect can be slightly tuned by changing the amount of excess Mn concentration (δ) between 0.15 - 0.60 [37, 90]. However, it remains quite large due to the robustness of the 3D Weyl points. Search for the methods to tune the Weyl points has been already started [110, 111]. One of the well-known methods is using the suitable dopant of the parent Weyl semimetal [112, 113, 114].

Since both the Mn_3Ge and Fe_3Ge both can be synthesized in the hexagonal phase [79, 81], Fe can be an excellent candidate to substitute Mn and change the characteristics of Weyl Fermions hosted by the Mn_3Ge . Fe doped Hexagonal- Mn_3Ge has already been studied for decades [115, 116, 117, 118, 119]. However, their electrical transport properties have not been studied yet from the topological points of view. It has been reported by the Refs. [115, 116] that the in-plane antiferromagnetic transition temperature (T_{N1}) of the Mn_3Ge decreases with Fe doping up to $\sim 30\%$ Fe

doping. In the case of compounds with $\sim 15\% - 30\%$ Fe doping, second AFM transition was observed at $T_{N2} (< T_{N1})$, with moments along the z axis [116, 115]. The T_{N2} gradually increases, and approaches the T_{N1} between $25\% - 30\%$ Fe doping. Near 25% Fe doping, the sample starts to show ferromagnetic (FM) behavior, with an increase in critical temperature (T_c) as Fe doping increases. Eventually, T_c suppresses both the AFM ordering near 30% Fe doping, and the samples beyond 30% Fe doping show purely FM behavior [116, 115].

The 20% Fe doped Mn_3Ge compound show a significantly large temperature range where magnetization is similar and different, compared to the Mn_3Ge , within different temperature regimes [116, 115]. Therefore, to investigate the existence and nature of Weyl points with magnetic structure and Fe doping, we investigated the 22% Fe doped Mn_3Ge compound in detail. In this chapter, we will provide a detailed analysis of the magnetization, and resistivity of the compound. We observed that the Néel temperature ($T_{N1} = 242$ K) of the 22% Fe doped Mn_3Ge compound is much lower than Mn_3Ge (365 K). Also, the sample goes through another magnetic transition near ~ 120 K (T_{N2}). Anomalous Hall conductivity (AHC) is observed between T_{N1} and T_{N2} only. Detailed neutron diffraction analysis has shown that the ground state magnetic structure of the $(\text{Mn}_{0.78}\text{Fe}_{0.22})_{3.2}\text{Ge}$ compound, is same as Mn_3Ge between T_{N1} and T_{N2} . Below T_{N2} , the sample changes the moment direction, and becomes collinear AFM along the z axis. Finally, we conclude that the Weyl points are likely to be present in the 22% Fe doped Mn_3Ge compound as long as the magnetic structure of the sample remains the same as the Mn_3Ge .

6.2 Experimental details

The synthesis and characterization of the single crystal used for the experiment are already mentioned in the chapter 6. To perform the experiments, samples were oriented using the Laue diffractometer, along the required axes. Different crystallographic axes in the hexagonal and Cartesian coordinates are shown in the Fig. 6.1(a). Further, the magnetization and electrical transport measurements were performed using the PPMS and DynaCool setup mentioned in Chapter 3.

An unpolarized and polarized neutron diffraction experiments were performed using D23, and CRYOPAD (D3) instruments at ILL, France. The details instruments and experimental techniques of both instruments are mentioned in the Chapter 3. We have used the same crystal, shown in Fig. 6.1(b), for both experiments. In the case

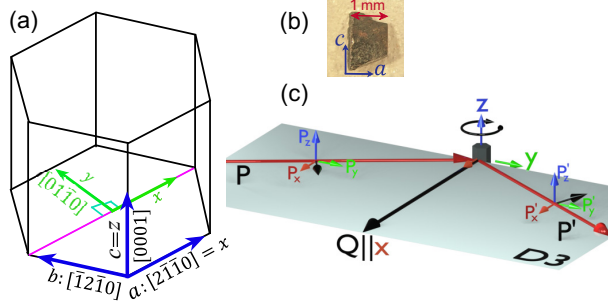


Figure 6.1: (a) Crystallographic axes in the hexagonal and Cartesian coordinate. (b) Picture of the crystal used during the neutron diffraction. (c) Illustration of the diffraction geometry of the CRYOPAD setup. The sample is rotated in the x - y plane. P' and P denote scattered and incident neutron beam.

of CRYOPAD experiment, tiny ferromagnetic moment ($\sim 0.028(3) \mu_B/\text{Mn}$) between T_{N1} and T_{N2} can slightly depolarize the polarized neutron beam. Therefore, a crystal with a very small path length (0.8 mm - 1.2 mm), weighing 13 mg, was used during the experiment. The CRYOPAD experiment was performed in two parts. Initially, the sample was oriented with c axis along the vertical to access the $(hk0)$ reflections. Further, the crystal was reoriented with b axis along the vertical direction to measure the $(h0l)$ -type reflections. In each case, the sample was cool down, below 300 K, under the 1 T of the magnetic field set along the b axis (using vertical and horizontal field setup). The field cooling of the sample populates most of the domains along the easy axis.

6.2.1 Magnetization

The temperature (T) dependent magnetization (M) of the $(\text{Mn}_{0.78}\text{Fe}_{0.22})_{3.2}\text{Ge}$ shows two magnetic transitions, while heating the sample, near 242(2) K (T_{N1}) and 120(1) K (T_{N2}), as shown in the Fig. 6.2(a-c). These observations are similar to the Refs. [116, 115, 117, 118, 119]. It can be observed that the magnetization of the sample between T_{N1} and T_{N2} remains the same as the parent sample Mn_3Ge [55, 37]. On this basis, we can infer that the sample goes through paramagnetic to (in-plane) AFM regime at T_{N1} . This type of in-plane magnetic structure persists down to the T_{N2} . We will refer this magnetic region as **AF-I**. Below T_{N2} , the magnetization becomes very low, suggesting a pure antiferromagnetic structure of the sample in this temperature region, as predicted by the Ref. [115] as well. We will refer this magnetic regime as

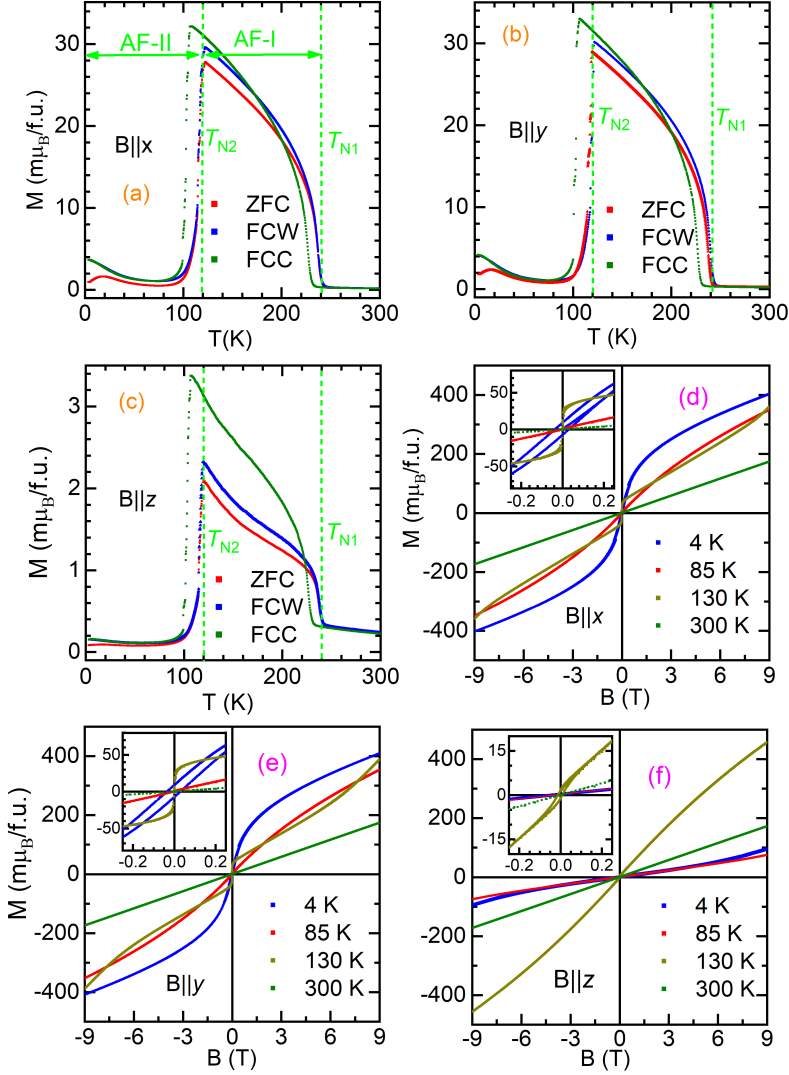


Figure 6.2: Temperature dependent magnetization (M) of the sample along (a) x axis, (b) y axis and (c) z axis. ZFC, FCC, and FCW denote zero field cooling, field cool cooling, and field cool warming conditions. The measurements were performed with 100 Oe of applied magnetic field. (d-f) shows the field dependent magnetization ($M(H)$) along three different axes (x , y , z). Low field (magnified) $M(H)$ along the x , y , z axes are shown in the inset of (d, e, f), respectively.

AF-II, which ranges from the lowest measured temperature, up to $T_{\text{N}2}$. AF-I and AF-II phases are shown in the Fig. 6.2(a).

The magnetic field dependent magnetization ($M(H)$) along different axes are also shown in the Fig. 6.2(d-f). It can be observed that the $M(H)$ and $M-T$ of the sample remain almost the same in nature when the field is applied along the x or y axis. However, the magnetization of the sample is significantly different along the z axis. Despite this, the clear signature of the magnetic phase transition is observed, along all the axes, near the same temperature irrespective of the direction of the applied magnetic field. Magnetization measurements of the sample were performed under zero field cooled (ZFC) and field cooled conditions, with a magnetic field of 100 Oe applied along the different axes. In the case of field cooled conditions, the measurement was done while cooling and warming the sample, and both the data are referred as FCC and FCW, respectively in the Fig. 6.2(a-c). Large thermal hysteresis of nearly 15 K and 10 K is observed near $T_{\text{N}2}$ and $T_{\text{N}1}$, respectively while cooling and warming the sample. The thermal hysteresis remains the same in magnitude whether the cooling/heating rate is kept at 2 K/min or 5 K/min. This suggests that the thermal hysteresis along all the axes is intrinsic.

The $M-T$ along the x and y axes, in the AF-I range, show a very small magnitude of the magnetization, suggesting the presence of tiny FM in the sample within the a - b plane. The $M(H)$ along the x and y axis shows that the residual magnetization of nearly $0.028(3) \mu_{\text{B}}/\text{f.u.}$ is present at 130 K (AF-I regime), which also implies the presence of small FM moment in this temperature regime. In contrast to this, no residual moment was observed in the magnetization along the z axis. $M(H)$ data along all the axes shows almost linearly increasing behavior with the magnetic field, which suggests the AFM nature of the sample. These observations are very similar to the magnetization of the parent phase - Mn_3Ge . Therefore, it can be argued that the magnetic structure of the sample remains the same as the parent phase - Mn_3Ge [52]. However, the in-plane FM moment in the $(\text{Mn}_{0.78}\text{Fe}_{0.22})_{3.2}\text{Ge}$ ($0.028(3) \mu_{\text{B}}/\text{f.u.}$) is larger compared to the Mn_3Ge ($0.018 \mu_{\text{B}}/\text{f.u.}$ [55]).

Below 110 K ($T_{\text{N}2}$), the magnetization reduces significantly, as shown in the Fig. 6.2(a-c). The $M(H)$ data (at 4 K, 85 K) shows nearly AFM behavior at low field ($B < 1$ T) along all the axes (Fig. 6.2(d-f)). This suggests that the sample is AFM in the AF-II regime as well. Ref. [115] suggest that nearly 22% Fe doped sample shows AFM behavior below 120 K, followed by the FM structure below 70 K. We have observed tiny splitting between the ZFC and FCW curve below 25 K (Fig. 6.2(a-c)),

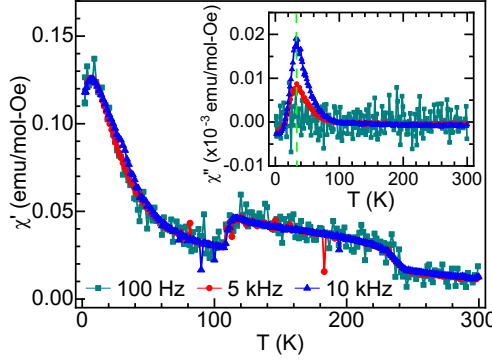


Figure 6.3: Temperature dependent magnetic susceptibility of the sample at 10 Hz, 5 kHz, 10 kHz frequency. The samples oscillates along the x axis. χ' show real part of the AC magnetic susceptibility. Inset: χ'' shows imaginary part of the AC magnetic susceptibility of the sample along the x axis. Dashed line show the onset temperature of the tiny FM in the sample.

suggesting the presence of small FM below this temperature. $M(H)$ data at 4 K and 85 K also show different natures at high fields. $M(H)$ data at 4 K show very small field hysteresis, and magnetization starts to saturate beyond 1 T, which is not the case at 85 K. These observations imply the onset of FM behavior, at high field applied at the low temperature. However, the magnetization of the sample shows the presence of dominant AFM behavior near zero field, in the entire AF-II regime.

AC susceptibility (χ_{AC}) of the sample was measured at 1000 Oe (DC field), as shown in the Fig. 6.3. Real part of χ_{AC} (χ') also show phase transitions at T_{N1} and T_{N2} . However, the imaginary part of the χ_{AC} (χ'') does not show anomaly near T_{N1} and T_{N2} , but a kink near 50 K is observed, which enhances with the increase in frequency. The peak position of the χ'' does not change with frequency, suggesting the absence of the spin glass magnetic phase in the sample, as observed at low temperature in the case of Mn_3Sn [120]. The kink in χ'' is slightly above the temperature where splitting the ZFC - FCW of the sample. These observations suggest the presence of FM fluctuations or field induce FM transition in the sample below ~ 50 K.

Since various types of magnetic structures can give rise to the observed magnetization, different neutron diffraction techniques were used to determine the ground state magnetic structure of the sample in AF-I and AF-II regimes.

6.3 Electrical transport measurements

Resistivity of the sample along the x , y , and z axis was measured as shown in the Fig. 6.4(a). The resistivity behavior along all the axes remains similar to each other. The magnetic transitions at 120 K and 242 K are visible in all the resistivity measurements. This suggests a strong coupling between the magnetic structure and electrical properties of the sample. A sharp jump in resistivity data can be observed near 120 K, very similar to the magnetization. The resistivity data also show thermal hysteresis of ~ 15 K, similar to the M - T , while cooling and warming resistivity measurements of the sample (inset of Fig. 6.4(a)). Thermal hysteresis remains the same in magnitude, similar to the M - T when the measurement was done at 1 K/min, and 5 K/min. Therefore, the origin of thermal hysteresis near $T_{\text{N}2}$ is intrinsic. The nature of resistivity in the AF-I and AF-II regimes is semi-metallic and metallic, respectively.

Hall resistivity of the sample was measured for various combinations of electric current and magnetic field. When the magnetic field was applied along the z axis, Hall resistivity vanishes as the field approaches zero, as shown in the Fig. 6.4(b). In contrast to this, for $B \parallel x$, significant residual Hall resistivity was observed at zero fields when the measurement was done in the AF-I regime (130 K, 200 K). The observed residual Hall resistivity is referred as the anomalous Hall resistivity (AHR) and denoted as ρ_{zy}^A in the Fig. 6.4(c). The observed AHR in our sample is similar to the AHR observed in the Mn_3Ge [55, 37]. AHR is usually observed in the ferromagnetic (FM) samples [103], in which case Hall resistivity follows $M(H)$ behavior of the sample. However, in our case, the Hall resistivity for $B \parallel x$ (ρ_{zy}^A) does not follow the $M(H)$ curve (for $B \parallel x$) of the sample (compare Fig. 6.4(c) and Fig. 6.2(d)). Therefore, the origin of AHR in our sample has to be intrinsic and originated from the non-zero Berry curvature, similar to the Mn_3Ge .

Anomalous Hall conductivity (AHC), which is an intrinsic quantity, denoted as σ_{ij}^A , and defined as: $\sigma_{ij}^A \approx -\rho_{ij}^A/(\rho_{ii}\rho_{jj})$. Here, ρ_{ii} and ρ_{jj} denote the normal resistivity of the sample along the i and j axes, respectively. ρ_{ij}^A denotes the AHR, where current and voltage is measured along the i and j axes, respectively, and field is applied perpendicular to i and j both. Hall effect, with magnetic field along the x axis, was measured at various temperatures below 300 K, down to the 4 K. Residual Hall resistivity at zero fields was determined (in the same way as mentioned above) at various temperatures. The temperature dependence of AHR and AHC (calculated using AHR) corresponding to the $B \parallel x$ is shown in the Fig. 6.4(d). It is interesting

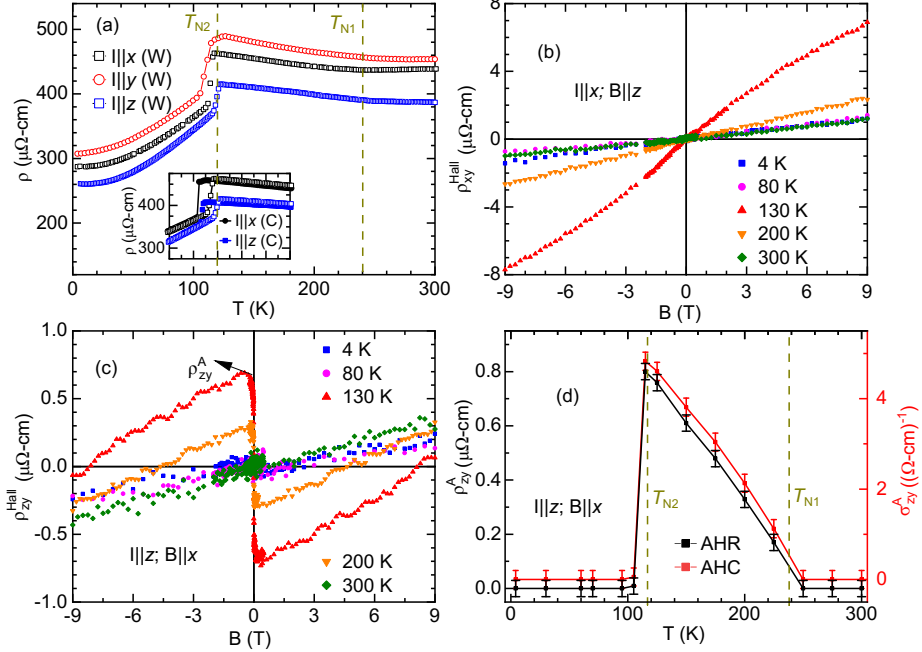


Figure 6.4: (a) Resistivity of the sample along the different axes mentioned in the plot. A magnified version of resistivity near 120 K is shown in the inset. The legends showing (W) and (C) imply that the data were collected while warming, and cooling the sample, respectively. (b) Hall resistivity of the compound with the magnetic field applied along the z axis. (c) Hall resistivity of the sample with current is applied along the z axis, and the magnetic field is applied along the x axis. The data were anti-symmetrized to extract the pure Hall contribution and deduct the magneto-resistance contribution. Non-zero Hall resistivity was observed, at a few temperatures, as the field approaches zero. The residual Hall resistivity is marked as ρ^A_{zy} , which is known as anomalous Hall resistivity (AHR). (d) shows the temperature dependence of the AHR and anomalous Hall conductivity (AHC) corresponding to the $B \parallel x$.

to observe that the AHC is observed in the AF-I temperature regime only, which is expected because the magnetization of the sample behaves similar to the parent compound within the AF-I regime only.

The AHC vanishes in the AF-II regime, which suggests that the Berry curvature vanishes in the AF-II regime. Usually, Berry curvature vanishes in the conventional AFM systems with pairwise antiparallel moments [51, 55, 121, 122]. It can be argued that Berry curvature may sustain in the case of collinear AFM systems as well, if non-magnetic atoms are sitting in the non-centrosymmetric sites, leading to the anisotropic magnetization density of the magnetic atom [123, 124, 125]. However, in our case, the Ge atom, which is non-magnetic, is located at the centrosymmetric site. Furthermore, we will see in the next section that the magnetic structure of the sample in the AF-II regime is collinear AFM along the z axis. Therefore, Berry curvature has to vanish in the AF-II regime, which confirms that the Weyl points do not exist in the AF-II regime.

The observation of AHC in the AF-I regime, and Mn_3Ge type magnetization in the same temperature regime suggest that the Weyl point is likely to be present in the 22% Fe doped Mn_3Ge compound as well (in the AF-I regime only). However, The magnitude of AHC is nearly 50 times smaller than the Mn_3Ge , which suggests that the location of Weyl points is much farther from the Fermi surface, and separation between a pair of Weyl points is much smaller when compared with the Mn_3Ge [56, 90]. Since the magnetic symmetry of the sample is intimately connected with the existence of Weyl Fermions, we have determined the ground state magnetic structure of the sample using different neutron diffraction techniques.

6.4 Neutron diffraction

Mn_3Ge possesses an in-plane AFM structure, which is unambiguously determined by the Ref. [52] using the CRYOPAD setup. Among the several possible in-plane non-collinear AFM structure, two magnetic structures cannot be easily differentiated. Since we also expect Mn_3Ge type magnetic structure in the AF-I regime, we performed unpolarized and polarized neutron diffraction of the sample using the D23, and CRYOPAD setups mentioned in chapter 3. A combined analysis of both experiments concludes the ground state of the $(\text{Mn}_{0.78}\text{Fe}_{0.22})_{3.2}\text{Ge}$.

The magnetic form factors for the Fe and Mn elements are close to each other, which makes it difficult to separate the individual magnetic moment, as both the

atoms occupy the same ($6h$) Wyckoff position. Therefore, we have performed all the neutron diffraction analyses with the assumption that both the Fe and Mn atoms (at $6h$ Wyckoff position) are magnetically ordered. We will refer to the combined magnetic moment of Mn and Fe as Mn+Fe moment.

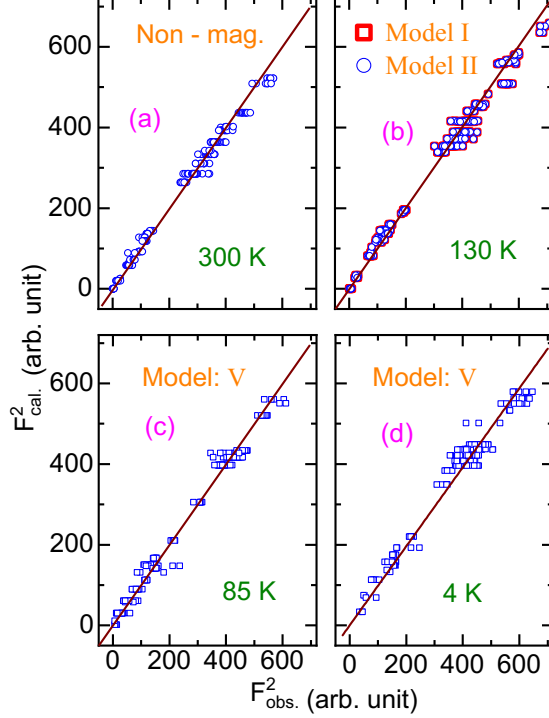


Figure 6.5: (a-d) Calculated (cal.) vs. observed (obs.) intensity at 300 K, 130 K, 85 K, and 4 K, respectively. Except at 300 K, the intensities at 4 K, 85 K, and 130 K correspond to the magnetic and nuclear contributions. The fitted models are mentioned in each plot and shown in the Fig. 6.6.

6.4.1 Unpolarized neutron diffraction (D23)

Unpolarized neutron diffraction of the sample was performed using the D23 instrument. Similar to the Mn_3Ge , propagation vector, $\mathbf{k} = 0$ is reported for the low Fe doped Mn_3Ge compound as well [115]. We also observed increased intensity (below T_{N1}) on the nuclear Bragg positions. This reconfirms the $\mathbf{k} = 0$ for our sample, as reported by the Ref. [115]. It has been reported by Ref. [115] that the 22% Fe doped

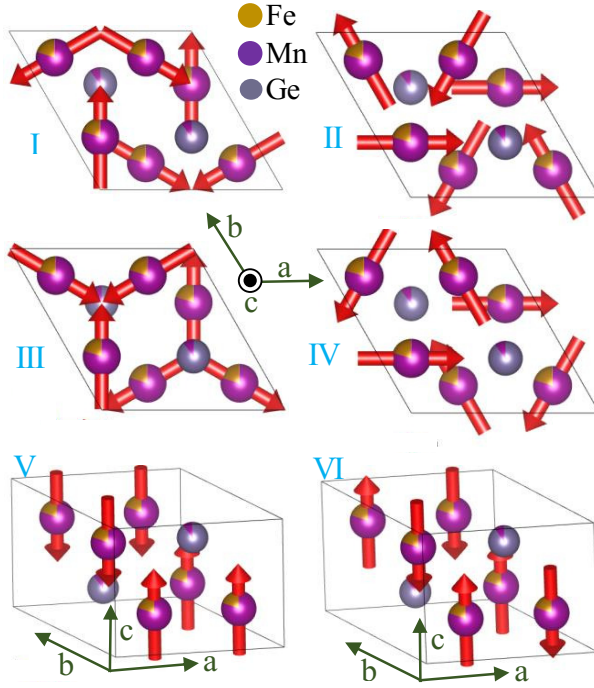


Figure 6.6: (I-IV) shows various magnetic models used for the neutron diffraction data analysis in the AF-I regime. In this case, the a and b axes are along the $[2\bar{1}10]$, and $[\bar{1}2\bar{1}0]$ crystallographic directions. (V-VI) denote the magnetic model with the moments lying along the z axis ($[0001]$).

sample is FM below 70 K, and the AFM phase is above this temperature. To confirm this, we have performed neutron diffraction measurements at 4 K, and 85 K, in addition to the 130 K, and 300 K. The neutron diffraction was performed with scattering vector, $Q (= \frac{\sin\theta}{\lambda})$, varying from 0.1 to 0.7.

The data analysis was performed using the JANA2006 software [105]. The nuclear structure refinement was performed at 300 K data. It was observed that the data fit well the hexagonal crystal lattice having $P6_3/mmc$ symmetry (space group no. 194), the same as the parent compound. Calculated (cal.) vs. observed (obs.) intensity, corresponding to the 300 K, is shown in the Fig. 6.5(a), where a good agreement between observed and calculated intensity confirms that the nuclear model with the given symmetry $P6_3/mmc$ is present in the sample at 300 K. The refined parameters at 300 K is mentioned in the Table 6.1. The refined chemical formula of the sam-

Table 6.1: The refined parameters of the D23 data analysis, at different temperatures, corresponding to the best fitted magnetic models.

Temperature	4 K	85 K	130 K	300 K
Magnetic model	Fig. 6.6(V)	Fig. 6.6(V)	Fig. 6.6(I; II)	-
Moment (μ_B)	1.24(8)	1.18(12)	1.24(9); 1.25(8)	0
χ^2	1.5	2.9	2.4	2.2
R_w	4.3	3.9	3.1	2.8
Domain ratio	-	-	25:39:41; 42:31:29	-
No. of independent reflections	25	19	25	22

ple is $(\text{Mn}_{0.79(2)}\text{Fe}_{0.21(2)})_3(\text{Mn}_{0.12(5)}\text{Ge}_{0.88(5)})$. This suggests that nearly 12% Ge sites (Wyckoff position: $2c$) are occupied by the Mn atoms, which is slightly more than predicted by the chemical analysis of the sample ($\sim 6\%$). It also means that $\sim 1.5\%$ excess (unreacted) of Mn atoms is sitting randomly inside the sample. The neutron diffraction analysis confirms that $\sim 21\%$ Mn sites (Wyckoff position: $6h$) are occupied by the Fe atoms, which is matching with the chemical analysis. Allowing Fe atoms to occupy Ge sites increases the goodness of fitting parameters, which implies that Fe atoms may not be occupying Ge sites.

The data analysis was performed at 130 K, using the nuclear parameters obtained at 300 K. The data were analyzed assuming that the Mn and Fe atoms occupying $6h$ sites are magnetically ordered. Representation analysis, using the SARAh software [126], suggests 12 irreducible representations with 18 basis vectors (ψ_j ; $j = 1, 2, 3 \dots 18$) in the case of space group $P6_3/mmc$ with the $\mathbf{k} = 0$. Each basis vector corresponds to a definite magnetic structure. Most of the magnetic structures can be neglected based on the magnetization data, except for 4 models which are possible in the AF-I regime. These magnetic models are shown in the Figs. 6.6 (I-IV). These magnetic models were used to refine the data at 130 K, and the fitting parameters (χ^2 , R_w) corresponding to each model are mentioned in Table 6.2. It is interesting to note that the magnetic models I and II (corresponding to ψ_{16} and ψ_{18} , respectively) fit equally well with the data at 130 K. The observed vs. calculated intensity for both the models (I and II) are shown in the Fig. 6.5(b), where it can be observed that model I and model II cannot be separated. The refined parameters corresponding to the model I and II are mentioned in the Table 6.1.

The propagation vector remains the same ($\mathbf{k} = 0$) at 85 K and 4 K as well, therefore

18 basis vectors are possible in this case also. Since the sample is AFM in the AF-II regime, any model among model I-VI (Fig. 6.6) can be the possible magnetic structure at these temperatures. Magnetic models I-VI were fitted with the neutron diffraction data at 4 K and 85 K. The χ^2 corresponding to the 4 K and 85 K data, fitted with different models, is mentioned in the Table 6.3, where it is clear that the model V fits best at 85 K and 4 K as well. A similar observation has been reported by the Ref. [115] also. The observed vs. calculated intensity (for model V) at both temperatures are shown in the Fig. 6.5 (c, d). Various refined parameters at 4 K and 85 K fittings are mentioned in the Table 6.1. It has been observed that the determined moment value ($1.24(8)\mu_B$) in our case is slightly lower than the value reported by the Ref. [115] ($1.4\mu_B$). This is possible because Ref. [115] has used a lower Fe doped compound for the neutron diffraction experiment.

Table 6.2: Goodness of fitting parameters for the D23 data, at 130 K, fitted with different possible magnetic models.

(130 K) Model	Fig. 6.6(I)	Fig. 6.6(II)	Fig. 6.6(III)	Fig. 6.6(IV)
χ^2	2.36	2.36	5.5	4.6
R_w	3.09	3.09	6.5	5.4

The integrated intensity of (101) and (110) reflections was measured at various temperatures between 4 K to 300 K as shown in the Fig. 6.7. The intensity corresponding to the (101) and (110) reflections remains almost the same, with an increase in temperature, in the AF-II regime. Both the intensities show a sharp increase near T_{N2} , reach a maximum near 125 K, and start decreasing as temperature increases.

Table 6.3: Goodness of fitting parameters for the D23 data. The data at 85 K and 4 K were fitted with different possible magnetic models.

Model	$T = 4 \text{ K } (\chi^2; R_w)$	$T = 85 \text{ K } (\chi^2; R_w)$
Fig. 6.6(I)	3.2; 11.7	17.4; 21.3
Fig. 6.6(II)	3.2; 11.9	17.2; 21.2
Fig. 6.6(III)	5.4; 12.7	26.1; 29.5
Fig. 6.6(IV)	4.9; 11.7	21.2; 25.1
Fig. 6.6(V)	1.5; 4.3	2.9; 3.9
Fig. 6.6(VI)	3.3; 10.5	14.5; 17.1

Intensity of the (101) and (110) reflections remains nearly constant beyond T_{N1} .

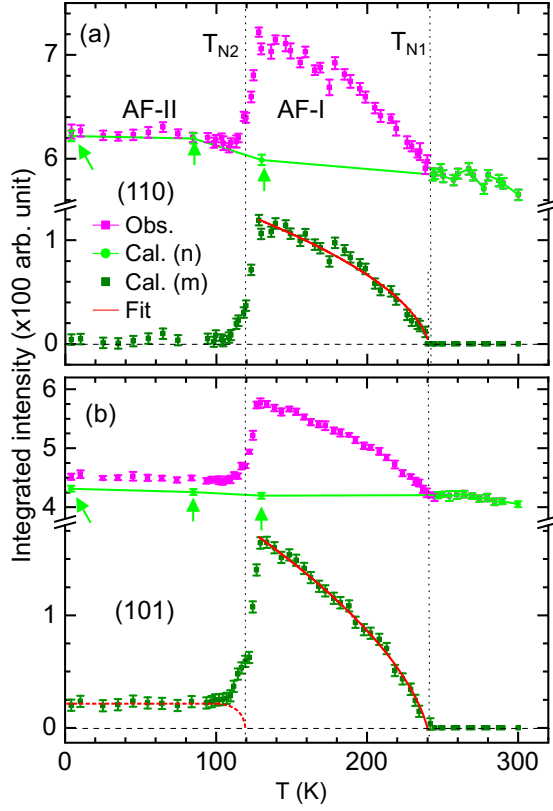


Figure 6.7: (a, b) shows variation of (110) and (101) reflections, respectively, with temperature. The reflections were measured using the D23 instrument while warming the sample. Obs. and Cal. denote observed and calculated intensity. (n) and (m) imply the nuclear and magnetic intensity contributions, respectively. The arrow pointed at 4 K, 85 K, and 130 K nuclear data means that the nuclear contribution is calculated using the D23 data analysis at these temperatures. Beyond 242 K, the sample is non-magnetic, therefore observed intensity is the same as the nuclear intensity. The dashed (yellow) line in (b) is a guide to the eye and represents the order parameter in the AF-II regime.

Nuclear and magnetic intensities were separated at 4 K, 85 K, and 130 K, using the complete neutron diffraction analysis. Since the nuclear intensity is expected to remain constant with temperature, temperature dependent nuclear intensity for (110)

and (101) reflections were calculated by extrapolating the data, as shown in the Fig. 6.7. Temperature dependent magnetic intensity was also calculated by subtracting the nuclear contribution. As shown in the Fig. 6.7, magnetic intensity is almost negligible for the (110) reflection in the AF-II regime. However, magnetic intensity for the (101) reflection is significant in the same magnetic regime (AF-II). The magnetic intensity of 101 reflection remains constant with temperature, which suggests that the order parameter remains constant in the AF-II regime.

The magnetic intensity corresponding to the (110) and (101) intensity decreases with temperature in the AF-I regime, and follows the order parameter relation: $I_{\text{mag}}(T) = I_{\text{mag}}^0(1 - T/T_{\text{N1}})^{2\beta}$. Where I_{mag}^0 denotes the intensity at the lowest temperature, and β is an exponent. $\beta = 0.26(4)$ and $0.28(2)$ were observed in the AF-I regime, for (110) and (101) reflections, respectively, which is slightly larger than observed in the case of Mn_3Ge ($\beta = 0.21$ [80]).

6.4.2 Polarized neutron diffraction (CRYOPAD)

The spherical neutron polarimetry (SNP) technique was used to determine the true ground state magnetic structure of the sample in the AF-I regime as the D23 experiment could not distinguish between models I and II. For this purpose, the polarized neutron diffraction experiment was performed at 130 K. The experiment was also performed at 4 K to reconfirm the results obtained using the D23 data analysis.

Table 6.4: The reduced χ^2 (χ_r^2) - the goodness of fit statistical parameter for the CRYOPAD experiment data. The data were fitted with the various possible magnetic models at the mentioned temperatures.

Model ($T = 130$ K)	Fig. 6.6(I)	Fig. 6.6(II)	Fig. 6.6(III)	Fig. 6.6(IV)
χ_r^2 ($h0l$)	15	78	1934	943
χ_r^2 ($hk0$)	19	20	398	489
Model ($T = 4$ K)	Fig. 6.6(V)	Fig. 6.6(VI)		
χ_r^2 ($h0l$)	22	913		
χ_r^2 ($hk0$)	47	6998		

The polarization matrix - P_{ij} , was measured at 130 K corresponding to the several ($hk0$) and ($h0l$) planes. The polarization data were analyzed using the MAG2POL software [78]. The data were refined with the magnetic models I-IV shown in the Fig. 6.6. The reduced χ^2 (χ_r^2) corresponding the different reflections, fitted with the

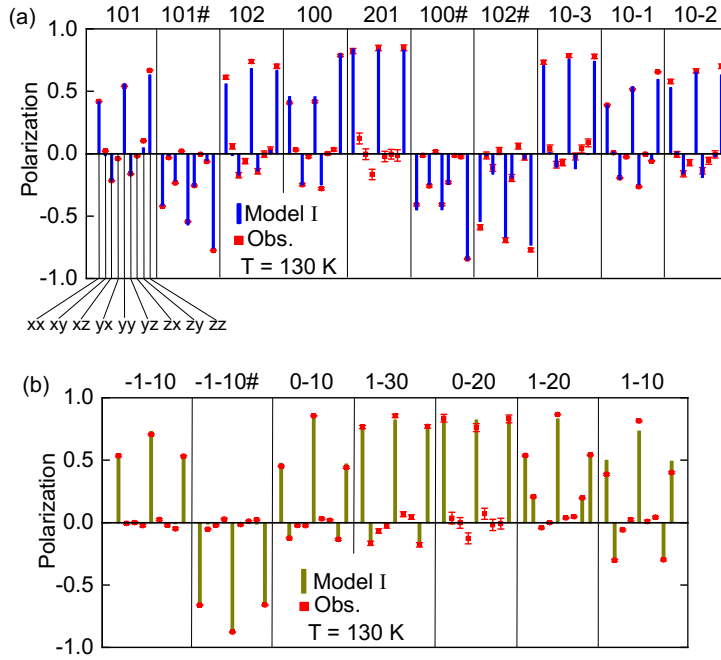


Figure 6.8: (a, b) Measured and calculated polarization, at 130 K, corresponding to the P_{ij} matrix elements, determined for the different (hkl) planes mentioned on the top. The reflection which is followed by # suggests that the incident polarization was reversed.

different possible models are mentioned in the Table 6.4. Models III and IV give very high χ_r^2 , therefore, they can be easily rejected. Whereas, it is interesting to observe that the χ_r^2 corresponding to the $(hk0)$ remains almost the same for models I and II. However, χ_r^2 is significantly different for these models when $(h0l)$ reflections are compared. Since model I fits best for all the reflections, with the significantly low value of χ_r^2 , it has to be the ground state of the sample at 130 K. The calculated and measured polarization corresponding to the various reflection fitted with the model I is shown in the Fig. 6.8. It can be noticed that the calculated polarization values for the model I is matching with the observed value, suggesting a good fit with the data. While fitting the data, the possibility of the different domain (120°) population was also considered because the sample was cooled down at 1 T of the applied magnetic field. The magnetic domain population ($\pm 120^\circ$) ratio, and refined magnetic moment at 130 K are mentioned in the Table 6.5. The average magnetic moment (average of

Table 6.5: Refined parameters at 4 K and 130 K, corresponding to the magnetic models which fit best with the CRYOPAD experiment data. Here, $(hk0)$ and $(h0l)$ denote the experimental configuration where c and b crystallographic axis, respectively, of single crystal was kept along the z axis (vertical position) of the instrument.

Temperature	4 K $[(h0l), (hk0)]$	130 K $[(h0l), (hk0)]$
Model	Fig. 6.6(V)	Fig. 6.6(I)
Moment (μ_B)	1.44(6), 1.59(9)	1.42(6), 1.38(7)
χ_r^2	22, 42	15, 18
Domain ratio	-	16:30:54, 60:25:15
No. of P_{ij} elements	90, 78	90, 72

$(hk0)$ and $(h0l)$ value, at 130 K, determined by the SNP analysis of data with the model I is $1.4(1) \mu_B$, which similar (within the error bar) to the magnetic moment determined value determined by the D23 data analysis ($1.24(9) \mu_B$). This observation confirms that the magnetic model I represents the ground state magnetic structure of the compound in the AF-I regime.

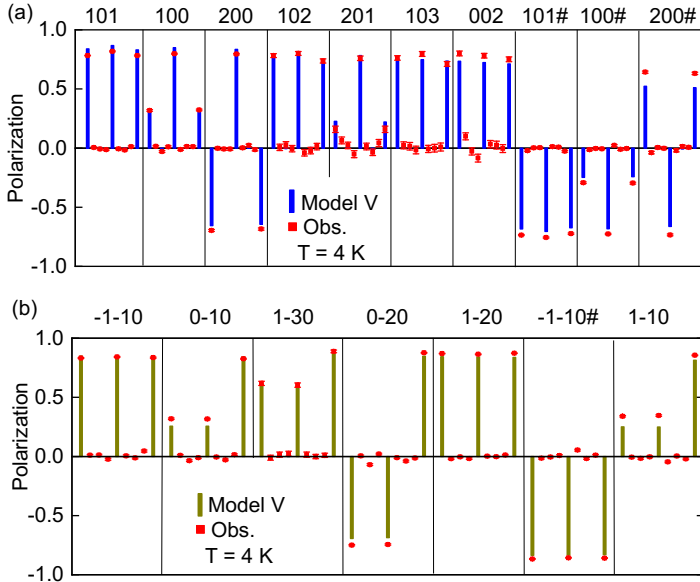


Figure 6.9: (a, b) Measured and calculated polarization at 4 K, corresponding to the different crystallographic planes mentioned on the top. Same as previous, the reflections followed by # suggest the reversed incident polarization.

Interestingly, the model I also correspond to the ground state magnetic structure of Mn_3Ge [52]. This suggests that the magnetic structure of the hexagonal- Mn_3Ge may persist up to 22% Fe doping at least in a small temperature regime. Since TRS is broken in the magnetic model I [51, 55], the observation of AHC in the AF-I regime is justified (Fig. 6.4(d)). This observation strengthens the possibility of the existing Weyl Fermions in the doped sample as well.

The SNP analysis was also carried out at 4 K, to reconfirm the ground state magnetic structure in the AF-II regime. Same as previous, P_{ij} matrix elements were obtained, at 4 K, corresponding to the several $(hk0)$ and $(h0l)$ reflections. The polarization matrix was analyzed with the magnetic models V and VI as they are the best possible models in the AF-II regime. The χ_r^2 corresponding to both the models are mentioned in the Table 6.4 ($T = 4$ K), where it is obvious to conclude that the goodness of fit for model V is orders of magnitude lower for model V compared to the model VI. The observed and calculated intensity for model V (best fit at 4 K), is shown in the Fig. 6.9, where it can be seen that nearly all the observed polarization elements match with the polarization calculated for the model V. This observation confirms that the magnetic structure of the sample in AF-II regime given by the model V (Fig. 6.6). The refined parameters, at 4 K, are mentioned in the Table 6.5(4 K). The obtained average magnetic moment (average of $(h0l, hk0)$) value at 4 K is $1.5(1) \mu_B$, which is slightly higher than the Mn+Fe moment magnitude determined by the D23 analysis ($1.24(8) \mu_B$). Such a small difference in two different may arise because of the following reason: the propagation vector, $\mathbf{k} = 0$ for our sample leads to the significantly large error bar in the various nuclear parameters using the D23 data analysis. The CRYOPAD analysis is very sensitive to the nuclear parameters because of the nuclear and magnetic interference. Therefore, a small difference between the Mn+Fe moment value, determined by two different techniques, is possible.

6.5 Conclusion

Magnetic phase transitions at T_{N1} and T_{N2} were observed in the resistivity and magnetization measurements of the $(\text{Mn}_{0.78}\text{Fe}_{0.22})_{3.2}\text{Ge}$ compound. Magnetization of the sample remains the same as the Mn_3Ge Weyl semimetal, within the AF-I regime. Hall resistivity measurements with field applied along the x and z axis show that the AHC is present in the sample when the field is applied along the x axis, as long as the sample temperature lies in the AF-I regime. The true magnetic structure of the

compound was determined using different neutron diffraction techniques and found that the sample possesses a Mn_3Ge type magnetic structure, which is a coplanar AFM structure in the a - b plane, in the AF-I regime. However, the magnetic structure in the AF-II regime is collinear AFM with Mn+Fe moments lying along the z axis.

Since all the characteristics of the $(\text{Mn}_{0.78}\text{Fe}_{0.22})_{3.2}\text{Ge}$ are similar to the Mn_3Ge , it can be argued that the Weyl points are very likely to be present in the Fe doped Mn_3Ge compounds as well. The AHC in our sample is nearly 50 times lower than the parent compound, which suggests that the separation between a pair of Weyl points is significantly smaller in 22%Fe doped compound, compared to the Mn_3Ge . Significantly small AHC also suggests that the location of Weyl points is much farther in the doped sample when compared with the Mn_3Ge . The AHC vanishes in the AF-II regime, which is expected because the sample possesses a collinear AFM structure, where Berry curvature usually vanishes. This implies that the existence of Weyl points is intimately linked with the underlying symmetry of the system. The persistence of Weyl points in the significantly Fe doped Mn_3Ge compound signifies its robust nature, which is very useful for spintronic application purposes. So, in the next chapter, we will discuss the detailed electrical transport effects, using several samples up to 22% Fe doping, to determine the evolution of Weyl points and its induced effects with Fe doping in Mn_3Ge .

7 Magnetic and transport properties of $(\text{Mn}_{(1-\alpha)}\text{Fe}_{\alpha})_{3.2}\text{Ge}$

7.1 Introduction

Anomalous transport properties of materials are determined by the topological band structure, which is very robust in nature [8, 23], as explained in the chapter 2. Anomalous transport effects observed in Weyl semimetals have their origin in the Weyl points. However, the location of Weyl points relative to the Fermi surface and separation between a pair of Weyl points determine the strength of chiral anomaly, and anomalous Hall effects, which originate due to the non-zero Berry curvature. Since Weyl semimetals have the potential for their application in spintronic devices, it is very important to study the dynamics of Weyl points, which can eventually pave the way to control anomalous transport effects. Mn_3Ge possesses Weyl points in a large temperature range, which makes it one of the best candidates to study the evolution of Weyl points under various circumstances. Since Fe_3Ge also possesses a hexagonal magnetic structure similar to the Mn_3Ge [79, 81], Fe can be substituted in the place of Mn in the Mn_3Ge compound, while retaining the Hexagonal phase. Therefore, we have explored the Fe doped Mn_3Ge compound to study the dynamics of the Weyl point with doping. Also, we observed in the last chapter that the magnetic structure of the 22% Fe doped compound changes (to collinear AFM) at low temperatures. Therefore, the study of Fe doped Mn_3Ge compound also provides an opportunity to determine the effect of change in magnetic structure over the persistence of the Weyl points, and resulting transport effects.

In this chapter, we will discuss the evolution of magnetic and transport properties of the various Fe doped Mn_3Ge samples. Analysis has shown that the magnetic structure of Mn_3Ge may sustain up to 26% Fe doping, within a certain temperature regime. Transport measurements were performed along the different axes and observed that the intrinsic Hall conductivity persists in the temperature regime where Mn_3Ge type non-collinear magnetic structure is present. We also interpret that the intrinsic Hall conductivity decreases significantly with doping concentration, and vanishes when the magnetic structure changes. Positive longitudinal magneto-conductivity (LMC), and planar Hall effect were observed as long as Mn_3Ge type magnetic structure persists. However, these effects weaken with Fe doping, and almost vanish or change their nature in the magnetic regime where the non-collinear triangular magnetic structure vanishes. These observations strongly suggest the existence of Weyl points in the doped compounds as long as the Mn_3Ge -type magnetic structure is retained. 30% Fe doped sample, which is ferromagnetic (FM), also shows a large anomalous Hall effect.

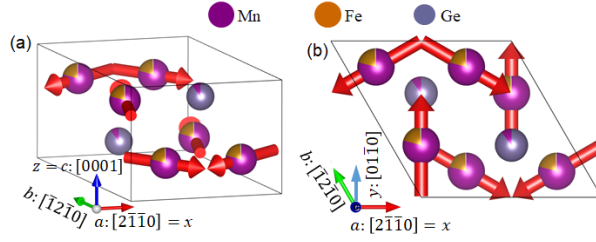


Figure 7.1: Magnetic and nuclear structure of $(\text{Mn}_{0.78}\text{Fe}_{0.22})_3\text{Ge}$ ($T = 130\text{K}$) as determined in the chapter 6. The crystallographic axes a , b , and c are described in the hexagonal lattice structure. a and b axes are oriented by 120° with each other. However, x , y , z axes form Cartesian coordinate system such that x and y , oriented by 90° with each other, lying within the a - b plane.

However, its origin can be explicitly linked with the magnetization of the compound.

7.2 Experimental methods

To perform the experiments, we have synthesized $(\text{Mn}_{(1-\alpha)}\text{Fe}_\alpha)_{3.2}\text{Ge}$ compounds with $\alpha = 0, 0.04, 0.10, 0.14, 0.18, 0.22, 0.26, 0.30$, as already explained in the chapter 4. We have grown single-crystal of samples with $\alpha = 0 - 0.22$. However, higher doped samples ($\alpha = 0.26, 0.30$), remained polycrystalline. X-ray diffraction analysis shown in the chapter 4, justifies that all the compounds synthesized in a hexagonal phase with $P6_3/mmc$ space group symmetry. The change in lattice parameters of the samples follows Vegard's law, implying that Mn is consistently replaced by Fe as doping concentration is increased. The single-crystal neutron diffraction analysis of $\alpha = 0.22$ sample (chapter 6) confirms that all the doped Fe atoms occupy the Mn sites ($6h$ Wyckoff site), which is expected. In addition to this, is also clear that the excess Mn occupies the Ge sites. The crystal and magnetic structure of the Fe doped sample are shown in Fig. 7.1.

The electrical transport and magnetization measurements of all the samples were performed using the PPMS and DynaCool instruments mentioned in the chapter 3. Most of the measurements were performed along the a axis and c axis, which are same as x and z (Cartesian) axes, respectively. The various crystallographic axes are defined in Fig. 7.1.

7.3 Magnetization

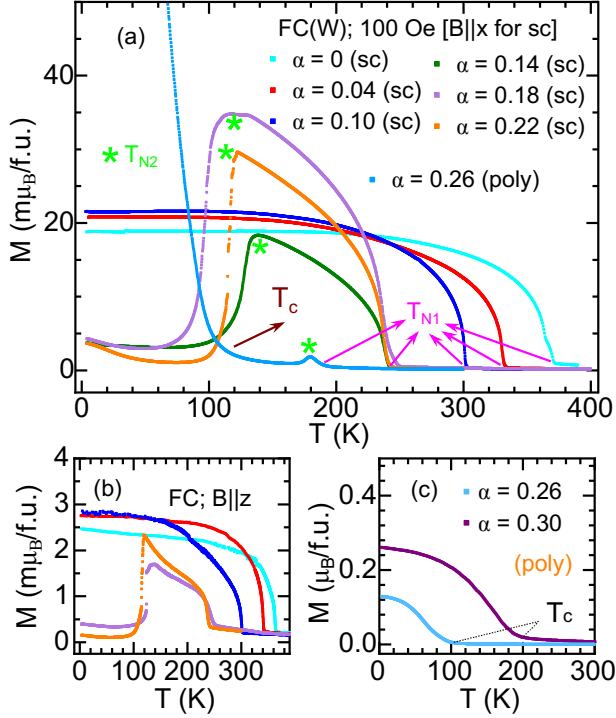


Figure 7.2: (a) Magnetization of the single-crystal (sc) Fe doped Mn_3Ge samples ($\alpha = 0 - 0.22$). Magnetization of polycrystalline (poly) $\alpha = 0.26$ is also shown. (b) Magnetization of the Fe doped samples ($\alpha = 0 - 0.22$) with magnetic field applied along the z axis. (c) Magnetization of the $\alpha = 0.26, 0.30$ (polycrystalline) samples.

The temperature dependent magnetization (M - T) of all the samples was measured between 4 K - 400 K. In the case of the single-crystal sample, magnetization was measured with the magnetic field (B) applied along x, y and z axes. The magnetization of the $\alpha = 0.22$ sample remains nearly same in the x - y crystallographic plane, as shown in the previous chapter (Fig. 6.2). Similarly, magnetization of $\alpha = 0 - 0.18$ also remains the same in the $(x$ - y) plane. However, the magnetization is significantly different when the magnetic field is applied along the z axis. The magnetization of the doped single-crystals ($B \parallel (x, z)$), and polycrystalline samples are shown in the Fig. 7.2.

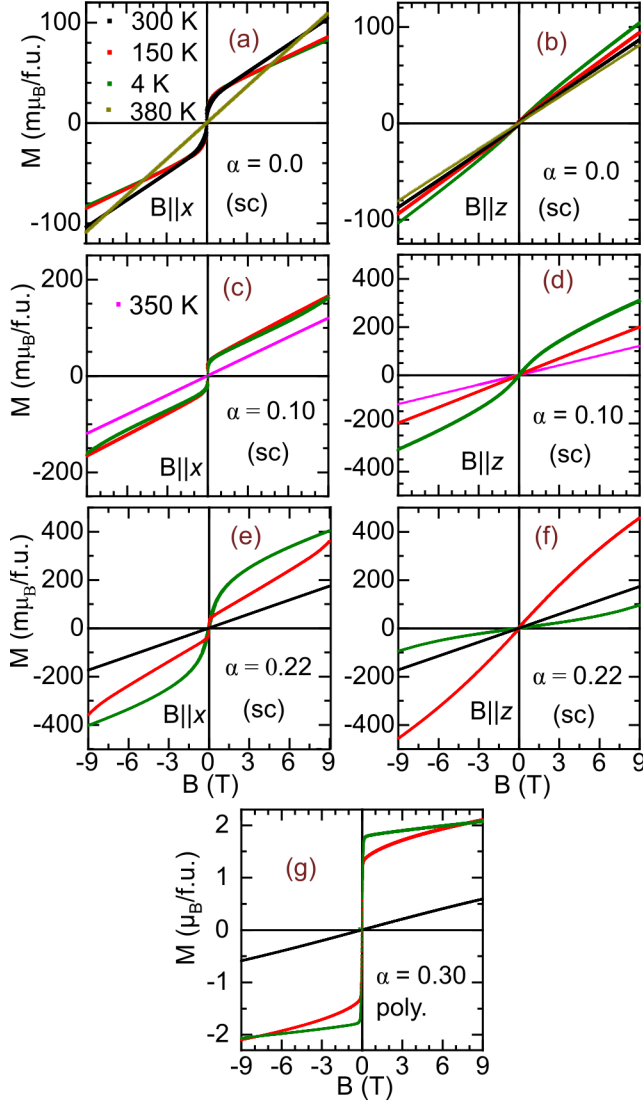


Figure 7.3: (a-f) Magnetic field (B) dependent magnetization (M) of the selected samples which show different magnetization behavior. Each plot shows M - B at different temperatures denoted by different colors (online). For $\alpha = 0, 0.10, 0.22$, measurements were performed using single-crystals (sc) with $B \parallel (x, z)$. (g) $\alpha = 0.30$ sample show average behavior as it is polycrystalline (poly.) in nature.

As shown in the Fig. 7.2, the nature of magnetization remains almost same for $\alpha = 0 - 0.10$. However, the Néel temperature (T_{N1}) decreases with increase in Fe doping fraction. For higher doping, $\alpha = 0.14 - 0.26$, second magnetic transition was also observed below T_{N1} , which is denoted as T_{N2} in the Fig. 7.2(a). Neutron diffraction analysis of $\alpha = 0.22$ in the last chapter has shown that its magnetic structure remains the same as the Mn_3Ge at 130 K, where magnetization is similar to the Mn_3Ge . It is interesting to observe that the magnetization of $\alpha = 0 - 0.10$, and $\alpha = 0.14 - 0.26$ compounds remain same as the parent sample below T_{N1} , and between $T_{\text{N1}} - T_{\text{N2}}$, respectively. Therefore, it can be concluded that $\alpha = 0.0 - 0.26$ compounds possess coplanar antiferromagnetic (AFM) structure, similar to the Mn_3Ge , below T_{N1} for $\alpha = 0.04, 0.10$, and between $T_{\text{N2}} - T_{\text{N2}}$ for $\alpha = 0.14 - 0.26$. We will refer this magnetic regime as **AF-I**. Magnetization of the doped compounds, along the z axis, also shows behavior similar to the Mn_3Ge within the AF-I regime (Fig. 7.2(b)).

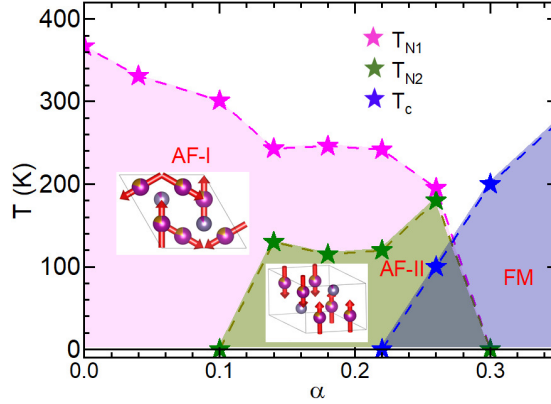


Figure 7.4: Magnetic phase diagram of the Fe doped Mn_3Ge . T_{N1} and T_{N2} correspond to the magnetic transitions shown in the Fig. 7.2(a). T_c correspond to the ferromagnetic (FM) transition temperature, which is visible for $\alpha = (0.26, 0.30)$ in the Fig. 7.2(c). AF-I corresponds to the Mn_3Ge type in-plane non-collinear magnetic structure, as shown in the same region. AF-II corresponds to the collinear AFM structure along z axis, as shown within this region. The details of the magnetic structure shown in different phases can be found in the chapter 6. The ground state magnetic structure in the FM regime is not known.

For $\alpha = 0.14 - 0.22$, second magnetic transition appears near 110 K, denoted as T_{N2} , below which magnetization becomes very small when compared to the parent sample (Fig. 7.2(a)). The magnetic structure of $\alpha = 0.22$, at 4 K, is collinear AFM along z

axis, as mentioned in the chapter 6. This suggests that, below T_{N2} , $\alpha = 0.14 - 0.26$ compounds possess collinear AFM structure along the z axis (shown in chapter 6). We will define this magnetic regime as **AF-II**.

In the case of polycrystalline $\alpha = 0.26, 0.30$ compounds, ferromagnetic (FM) transition below 100 K and 200 K, respectively, is observed, which is regarded as T_c in the Fig. 7.2(c).

Field dependent magnetization (M - B) of the samples were also measured, as shown in the Fig. 7.3, for selected compounds in which different magnetization is expected ($\alpha = 0.10, 0.22, 0.30$). In the case of $\alpha = 0.04 - 0.22$, the M - B behavior at 150 K (within the AF-I regime), along x and z , axes remains same as the $\alpha = 0$, which supports our previous conclusion that magnetic structure of $\alpha = 0.04 - 0.22$ are same as Mn_3Ge in AF-I regime. For $\alpha = 0.22$, which is similar to the $\alpha = 0.18$, the M - B at 4 K show AFM behavior, at low field, along x and z axis, which is reasonable because, in the AF-II regime (4 K), the sample possesses collinear AFM behavior with Mn+Fe moments lying along the z axis (chapter 6). M - B for this compound show FM behavior at high field, which suggests field induced FM transition in the compound at 4 K, as we discussed in the last chapter as well. M - B corresponding to the $\alpha = 0.26, 0.30$ show FM behavior below T_c , which is in line with the magnetization the same compounds.

The Fe doping fraction (α) dependence of T_{N1} , T_{N2} and T_c is shown in the phase diagram (Fig. 7.4). It is interesting to observe that T_{N1} decreases with the increase in α , and vanishes between $\alpha = 0.26 - 0.30$. The AF-II regime ($T < T_{N2}$) emerges between $\alpha = 0.10 - 0.14$, below ~ 110 K. T_{N2} remains almost constant up to $\alpha = 0.22$, then steadily increases up to $\alpha = 0.26$, and eventually suppressed by the FM of the samples between $\alpha = 0.26 - 0.30$. $\alpha = 0.30$ compound completely suppresses both the AFM ordering of the compound and becomes FM. Ground state magnetic structure of $\alpha = 0.26, 0.30$ in the FM regime is not known. The obtained phase diagram is roughly similar to the one determined by the Refs. [115, 116].

7.4 Electrical Transport Results

Our primary aim in this chapter is to study the evolution of Weyl points with Fe doping. Since Weyl points are likely to be present in the AF-I regime, we have mostly discussed the electrical transport properties of $\alpha \leq 0.22$. Initially, electrical transport measurements were performed for single-crystals with $\alpha = 0, 0.04, 0.10, 0.18, 0.22$. The resistivity of all the samples was measured along the different axes. Similar to mag-

netization, the resistivity of all the compounds behaves the same way along the x and y axes. However, the nature of resistivity is significantly different, compared to the x axis, along the z axis. The resistivity of the single-crystal ($\alpha \leq 0.22$) along x and z axes is shown in the Fig. 7.5, where different nature of the samples in the x - z plane is evident.

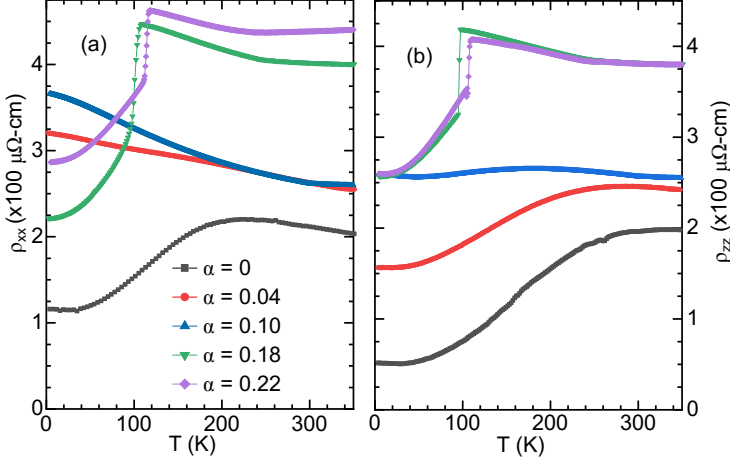


Figure 7.5: Resistivity of single crystal with $\alpha = 0-22$ samples. (a, b) denote the zero field resistivity of the different Fe doped samples along x and z axes.

As shown in the Fig. 7.5, for $\alpha = 0.04, 0.10$, the ρ_{xx} increases below T_{N1} , down to 2 K. ρ_{xx} for $\alpha = 0.18, 0.22$ compounds also increase below T_{N1} , however it drops suddenly below T_{N2} , and follow metallic behavior below T_{N2} . The resistivity data also show transition near T_{N2} , very similar to the magnetization, which suggests a strong link between the electrical transport and the magnetization of the compounds.

The resistivity of the compounds increases with an increase in Fe concentration, which acts as a substitution impurity. Therefore, magneto-resistivity (MR), Hall resistivity, and planar Hall effect (PHE) shall increase naturally, even if Berry curvature and location of the Weyl points remain the same in the doped compounds. There exist a direct connection between non-zero Berry curvature and induced anomalous Hall conductivity. Planar Hall conductivity and positive longitudinal magneto-conductivity (LMC) are also intrinsic effects, related to the location of the Weyl points. Therefore, to explore the evolution of Weyl points, comparisons between the different samples are made in the terms of conductivity, which is normalized by the longitudinal resistivity of the same compound.

As shown in the phase diagram (Fig. 7.4), the non-collinear coplanar magnetic structure persists in the temperature range of 120 K - 240 K, for all the compounds up to $\alpha = 0.26$. Therefore, electrical transport measurements corresponding to $\alpha = 0-0.22$ are compared at 150 K and 200 K to study the evolution of Weyl points with Fe doping. The measurements are also compared at 4 K, to observe the effect of change in magnetic structure on electrical transport phenomena. This may provide a hint of the link between the exotic transport effects of the Weyl semimetals and the magnetic symmetry of the sample.

7.4.1 Anomalous Hall effect

Hall resistivity of $\alpha = 0, 0.04, 0.10, 0.18, 0.22$ were measured with magnetic field applied along the different axes. Similar to the Mn_3Ge (chapter 5), the Hall resistivity of all the doped samples behaves the almost same way as long as the magnetic field is applied along the x or y axis. However, its nature is very different when the field is applied along the z axis. The Hall resistivity measurements with magnetic field along y and z axes, each at 4 K and 150 K is shown in the Fig. 7.6. Interestingly, non-zero Hall resistivity is observed for $\alpha = (0 - 0.22)$ at 150 K, when the field is applied along the y axis and turned back to zero. The residual Hall resistivity of the sample corresponding to the $B \approx 0$ is known as anomalous Hall resistivity (AHR), denoted as ρ_{xz}^A in Fig. 7.6(b). Where, $x(z)$ denote the axes along which current (Hall voltage) is applied (measured), given that the magnetic field is applied perpendicular to both the axes. It is important to note that the Hall hysteresis remains below 200 Oe for the doped and parent compounds as well (Fig. 7.6(c)). This suggests that the underlying magnetic characteristics of all the compounds are almost the same. Non-zero Hall resistivity is observed when the field is applied along the z axis, which is not expected (Fig. 7.6(d, e)). Since the anomalous Hall effect (AHE) corresponding to $B \parallel (x, y)$ is very large, even a small tilt away from the z axis can give rise to the small AHR. Therefore, AHR observed in the case of $B \parallel z$ possibly originates due to the small misalignment of the magnetic field away from the z axis, towards the x or y axis.

It can be observed that, at 4 K, $\rho_{xz}^A > 0$ in the case of $\alpha = (0, 0.04, 0.10)$ only. For higher doping ($\alpha = 0.18, 0.22$), $\rho_{xy}^A = 0$ was observed (Fig. 7.6(a)). However, when $B \parallel y$ is applied, $\rho_{xz}^A > 0$ at 150 K in all the cases ($\alpha = 0 - 0.22$) (Fig. 7.6(b)). Several Hall effect measurements were performed for $\alpha = 0 - 0.22$, at different temperatures

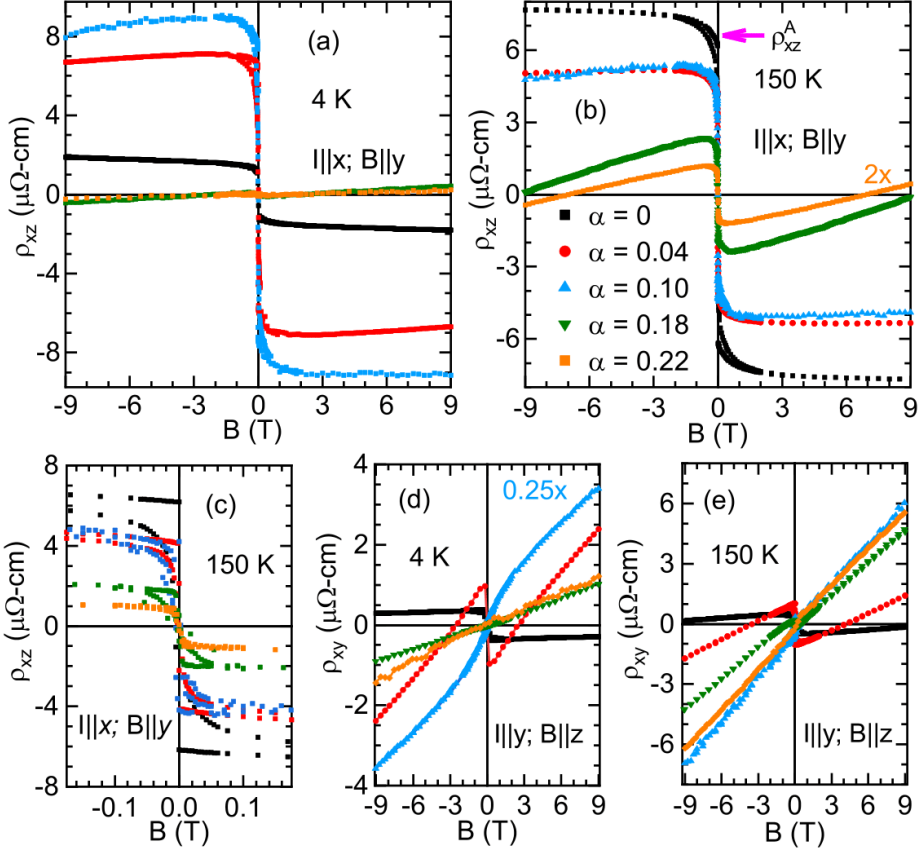


Figure 7.6: Hall resistivity corresponding to the $\alpha = 0, 0.04, 0.10, 0.18, 0.22$. (a, b) shows Hall resistivity at 4 K with the magnetic field applied along the y axis and z axis, respectively. The arrow in (b) denotes the zero field Hall resistivity, which we will refer as anomalous Hall resistivity. (c) A magnified version of the (b), showing Hall hysteresis corresponding to the mentioned compounds. (d, e) Hall resistivity at 4 K and 150 K, respectively, with the magnetic field, applied along the z axis.

starting from 4 K to 370 K, and corresponding AHR (ρ_{xz}^A) was determined whenever it was observed. AHR can be converted to anomalous Hall conductivity (σ_{xz}^A), using: $\sigma_{xz}^A \approx \rho_{xz}^A / (\rho_{xx}\rho_{zz})$. Where, ρ_{xx} and ρ_{zz} denote longitudinal resistivity along the x and z axes. Temperature dependence of σ_{xz}^A for $\alpha = 0 - 0.22$ is shown in the Fig. 7.7(a). It is interesting to observe that the $\sigma_{xz}^A > 0$ below T_{N1} for $\alpha = 0, 0.04, 0.10$, and between $T_{N1} - T_{N2}$ for $\alpha = (0.18, 0.22)$. $\sigma_{xz}^A = 0$ was observed below T_{N2} (in

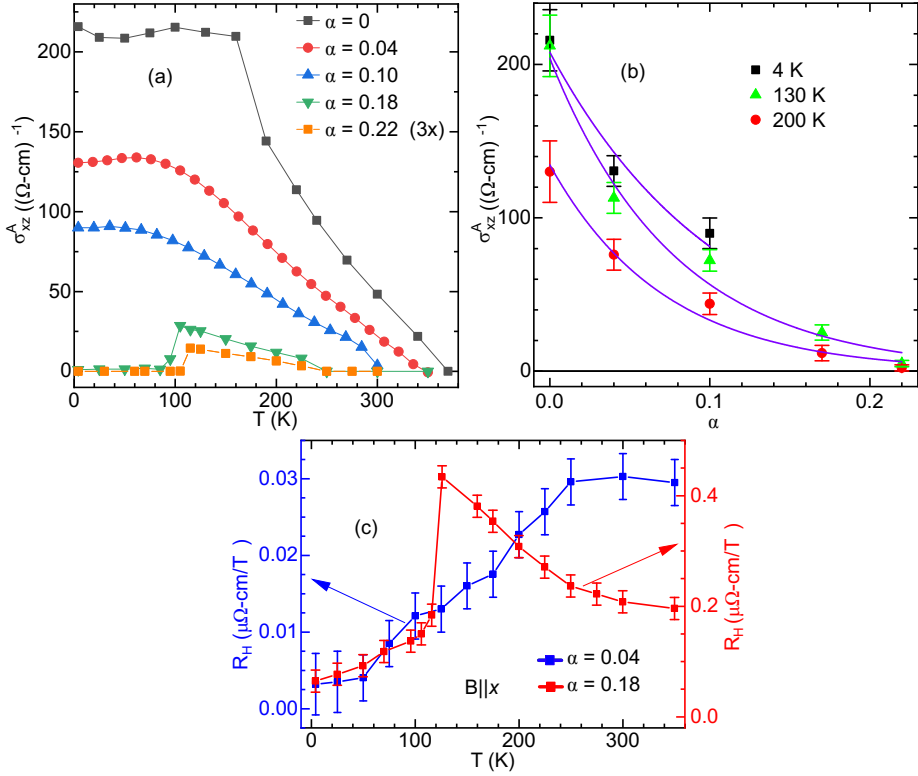


Figure 7.7: (a) Temperature dependence of σ_{xz}^A for different samples. σ_{xz}^A for $\alpha = 0.22$ shown in the graph is 3 times more than the actual value. (b) Change in σ_{xz}^A with doping fraction (α), at different temperatures. At 4 K, $\sigma_{xz}^A = 0$ for $\alpha = (0.17, 0.22)$ therefore not shown here. The data at 150 K and 200 K follow exponential decay behavior. Blue lines are the guide to the eye. (c) Temperature dependence of Hall coefficient (R_H) for two Fe doped samples, which shows different magnetization nature.

AF-II regime), in the case of $\alpha = (0.18, 0.22)$. The nature of σ_{xz}^A for different α follows behavior very similar to the magnetization (Fig. 7.2(a)). Since magnetic structure in the AF-I regime is the same as the parent sample, and non-zero σ_{xz}^A is present in the AF-I regime only, Weyl points are very likely to be present in the Fe doped compounds in the AF-I regime. This shows the robustness of the Weyl points, which is expected because of its 3D topological protection. The AHE vanishes in the AF-II regime, where the magnetic structure is collinear AFM having pairwise antiparallel Mn moments. Since Berry curvature vanishes in the centrosymmetric,

collinear AFM systems with pairwise antiparallel moments [55, 121, 123, 124, 125], vanishing AHE in the AF-II regime is justified. These observations show an intricate connection between anomalous Hall conductivity, the existence of Weyl Fermions, and the magnetic symmetry of the compound.

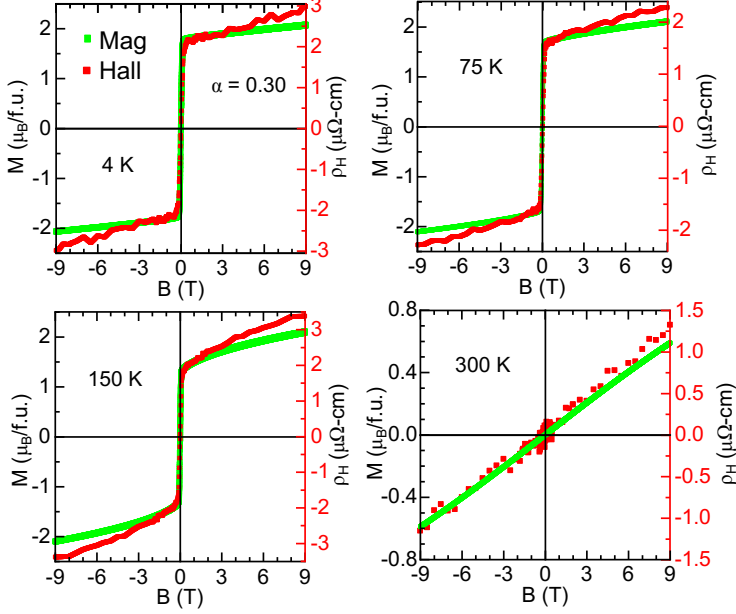


Figure 7.8: Field dependence of magnetization and Hall resistivity (for $\alpha = 0.30$) plotted together at each temperature $T = 4$ K, 75 K, 150 K, 300 K.

The evolution of σ_{xz}^A at 4 K, 150 K, and 200 K with doping fraction (α) is shown in Fig. 7.7(b). It is interesting that the σ_{xz}^A at 150 K and 200 K show exponential decay behavior with an increase in doping fraction. In a simplistic model, the magnitude of σ_{xz}^A is governed by the separation between Weyl points [32]. However, the location of Weyl points also decides the magnitude of the anomalous transport effect. Therefore, we can argue that the separation between the pair of Weyl points decreases, and the location of Weyl points changes with respect to the Fermi energy, with an increase in the Fe doping in Mn_3Ge .

Hall coefficient (R_H) for low and high Fe doped samples were measured ($\alpha = 0.04, 0.18$), and shown in the Fig. 7.7(c). Unlike Mn_3Ge , the Hall coefficient does not change in sign, for $\alpha = 0.04, 0.18$ compounds. Furthermore, metal-semimetal transition, which is observed in the Mn_3Ge , also vanishes for all the Fe doped compounds

(Fig. 7.5(a)). These observations suggest that the electronic topological transition observed in the Mn_3Ge is suppressed just by 4% of Fe doping. Interestingly, a sudden change in R_H is also observed for $\alpha = 0.18$, which implies a change in carrier concentration near 110 K driven by the magnetic transition.

Hall effect measurements were also performed for $\alpha = 0.30$, which is FM. AHR has been observed below T_c . The field dependence of Hall resistivity and magnetization measured at 4 K, 75 K, 150 K, and 300 K is plotted together, as shown in Fig. 7.8. The AHR vanishes at 300 K, which is beyond T_c . It is interesting to observe that Hall resistivity can be scaled with the magnetization of the sample, which suggests that the anomalous Hall effect in the compound with $\alpha = 0.30$ originates due to the magnetization of the sample. A similar observation has been made by Ref. [103] in the case of different FM compounds. Scaling of Hall resistivity with magnetization suggests AHR does not originate due to the Weyl points, suggesting the absence of Weyl Fermions in this compound. It can be observed in Fig. 7.8 that the Hall resistivity slope is slightly higher than expected in the case of its perfect scaling with magnetization. Hall resistivity for magnetic compounds can be written as $\rho(H) = p_1 B + p_2 M(B)$, where p_1 and p_2 correspond to the proportionality constants. This implies that the residual Hall slope corresponds to the hall contribution due to the normal Hall resistivity of the sample, which determines the carrier concentration of the compound.

7.4.2 Chiral anomaly

Fe doped compounds with $\alpha = 0 - 0.22$ possess magnetic structures the same as the Mn_3Ge . They show AHE, owing to the non-zero Berry curvature whose source and sink are, most likely, the pair of Weyl points with opposite chirality. Chiral anomaly is one of the fundamental signatures of the Weyl semimetals. Therefore, to ensure the presence of Weyl points, we have measured magneto-resistance and the planar Hall effect of the Fe doped compounds to find out if the chiral anomaly induced effects are present (in the AF-I regime) or not. Systematic analysis of these measurements helps us to determine the evolution of the chiral anomaly effect and Weyl points with Fe doping.

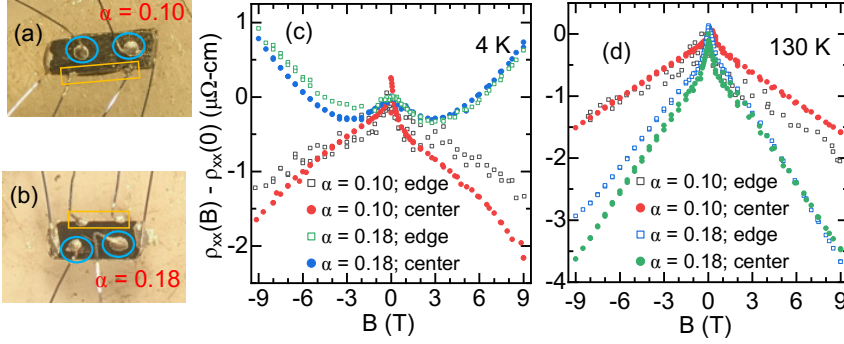


Figure 7.9: Raw data of the longitudinal magneto-resistance measurements (raw data) with different locations of the voltage contacts to determine the effect of current jetting in the $\alpha = 0.10, 0.18$ samples. (a, b) show contacts used to measure the current jetting in $\alpha = 0.10$ and $\alpha = 0.18$ compounds, respectively. Sky blue circles denote contacts near the ‘center’ of the sample. Whereas, the orange rectangle encloses the voltage contacts which are at the ‘edge’ of the sample. (c, d) show LMR of the samples (along the x axis) at 4 K and 130 K, respectively. At each temperature, the LMR was measured by the voltage contact which are at the ‘edge’, and ‘center’ of the sample, as shown in (a, b).

7.4.2.1 Longitudinal magneto-conductivity

We have measured longitudinal magneto-resistance (LMR) of $\alpha = (0, 0.04, 0.10, 0.18, 0.22)$ compounds with magnetic field (B) applied parallel to the electric current (I) direction. The magneto-resistance percentage of the sample ($\text{MR}\% = \frac{\rho(B) - \rho(0)}{\rho(0)} \times 100$) remains within 1% for all the compounds, up to $B = 9$ T. Such a small change in MR can arise due to the anisotropy in longitudinal MR, or current jetting effect. Since Mn_3Sn and Mn_3Ge are the low mobility compounds with very small anisotropy in MR and resistivity of the compounds [82], the effect of the current jetting effect is negligible in these compounds [82], same as observed in the chapter 5, for Mn_3Ge . We have also measured the effect of current jetting due to inhomogeneous electric current in the $\alpha = 0.10, 0.18$ compounds using the voltage contact at the center, and the edge of the sample (Fig. 7.9)(a, b). As shown in the Fig. 7.9(c, d), the LMR of the sample remains very similar irrespective of the location of voltage contacts. This justifies that the effect of current jetting is negligible in Fe doped Mn_3Ge compounds under measurements. Moreover, most of the measurements were performed multiple times using thin samples (0.1 - 0.2 mm) having lengths and breadth of 1 - 1.5 mm and 0.5

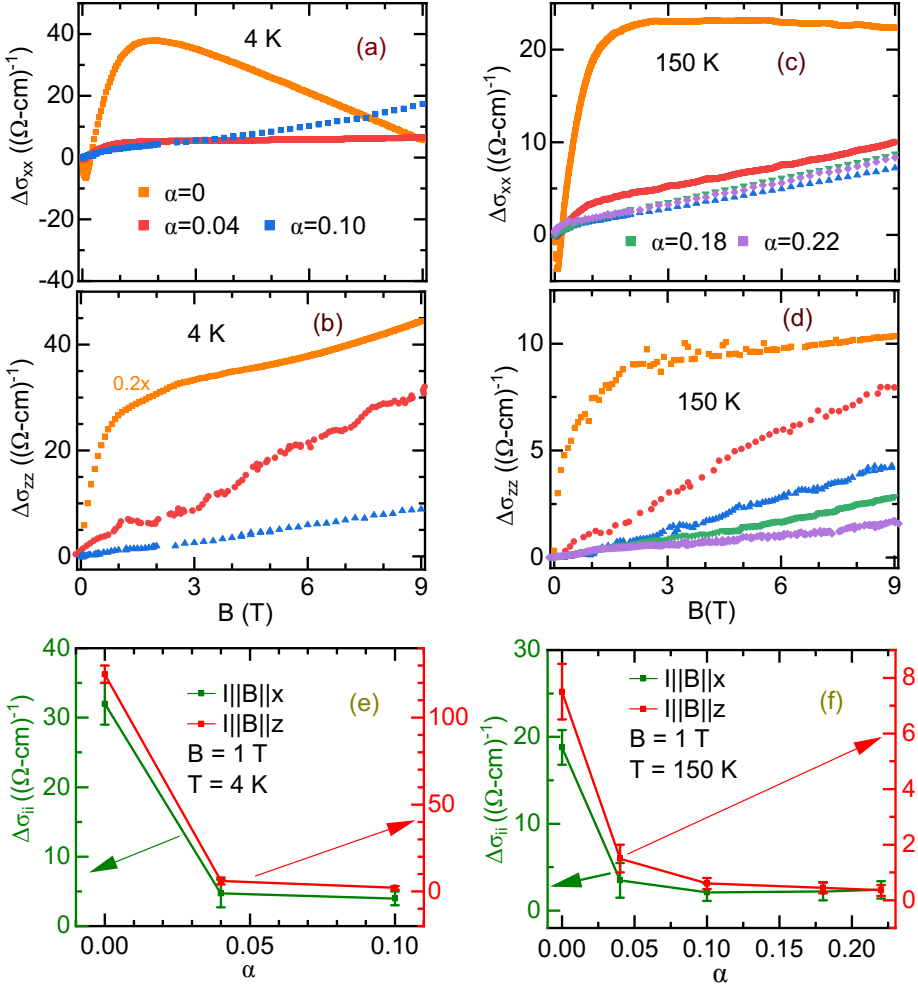


Figure 7.10: Longitudinal magneto-conductivity (LMC) of the parent and Fe doped samples at (a, b) 4 K, (d, e) 150 K. $\Delta\sigma_{ii} = \sigma_{ii}(B) - \sigma_{ii}(0)$, where, ii denotes the LMC along the i axes. The variation of $\Delta\sigma_{ii}$ ($i = x, z$) at 1 T, with Fe doping fraction (α) is shown in (c, f).

- 0.8 mm, respectively, and similar results were observed during each measurement. This confirms the intrinsic origin of the observed data.

One of the prominent experimental signatures of the chiral anomaly effect is the observation of positive longitudinal magneto-conductivity (LMC) [45, 48, 91]. The LMC along x and z axes can be obtained by using the fundamental relation between longitudinal resistivity and longitudinal conductivity: $\sigma_{ii}(B, T) = 1/\rho_{ii}(B, T)$. Since the signature of the presence of Weyl points is observed in the AF-I only, we will perform (below) a separate analysis of LMC data corresponding to AF-I, AF-II, and FM regimes.

For $\alpha \leq 0.10$ compounds, the measurements at 4 K and 150 K belong to the AF-I regime. For $\alpha = 0.18$ and 0.22, measurements at 150 K belong to the AF-I, however, measurements at 4 K belong to the AF-II regime.

LMC in AF-I regime: It can be observed in the Fig. 7.10 (a-d) that positive LMC (along the x and z axis) at 4 K and 150 K is present, at least at a low magnetic field, for all the samples in the AF-I regime. In contrast with Mn_3Ge , LMC for all the Fe doped samples keeps increasing, in the AF-I regime, up to 9 T. The probable reason behind such a difference between parent and doped compound could be the significant change in the spin density of states (SDOS), due to the Fe doping. This is possible because SDOS near the Fermi surface is very sensitive to the chemical composition. The LMC corresponding to the Fe doped sample in the AF-I regime is very similar to the Mn_3Sn [82, 90], which suggests that the origin of the positive LMC in the doped compounds could be the chiral anomaly effect, which is expected as well.

It is also important to mention that the resistivity of all the Fe doped compounds up to $\alpha = 0.22$ (Fig. 7.5) shows non-metallic behavior (in AF-I regime) in all the cases, except for the resistivity of $\alpha = 0.04$ along the z axis. As mentioned in the last chapter, positive and negative LMC can be observed in the case of half-metallic/semimetallic and metallic samples, respectively [49, 94, 95, 96, 98, 99]. Therefore, the observed positive LMC may also arise from the semimetallic nature of the Fe doped compounds. Therefore, further justification in favor of chiral anomaly is required to strengthen the claim for chiral anomaly effect in the Fe doped compounds.

Since Mn_3Ge shows chiral anomaly induced positive LMC (along the x axis) below 1.5 T only, we will compare the LMC magnitude for different samples, in the AF-I regime, at 1 T. As shown in the Fig. 7.10(e), the magnitude of LMC, at 4 K, decreases by nearly 10 times just after 4% Fe doping. Similarly, at 150 K, 4% Fe doping leads

to a decrease in the magnitude of LMC by nearly 5 times (Fig. 7.10(f)). A similar observation has been made in the case of Mn_3Sn as well [82], which shows a clear sign of the chiral anomaly effect. Such a drastic decrease in the positive LMC with very small Fe doping is one of the strongest signs of its origin to be the chiral anomaly effect because chiral anomaly induced conductivity, $\sigma_{\text{chiral}} \propto 1/\mu^2$. Where, μ is the location of the Weyl points with respect to the chemical potential [91, 43].

Furthermore, Weyl points are very likely to exist in the AF-I regime, therefore chiral anomaly induced effects, very small though, are expected. Therefore, the observed positive LMC (in AF-I regime) in Fe doped compounds is very likely to be originated from the chiral anomaly effect. However, the positive LMC magnitude is very small compared to the parent sample, therefore further theoretical justifications are required to justify that the origin of the positive LMC is dominated by the chiral anomaly effect.

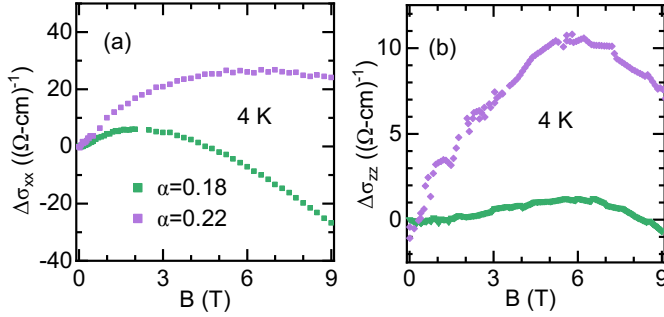


Figure 7.11: LMC for the $\alpha = 0.18, 0.22$ compounds at 4 K, which lies in the AF-II regime.

LMC in AF-II regime: Low temperature range for the compounds $\alpha = 0.18, 0.22$ correspond to the AF-II regime, where Weyl points are not expected to be present. We have analyzed LMC for these two compounds at 4 K, which lies in the AF-II regime. As shown in the Fig. 7.11, LMC along the x and z axes increase with the magnetic field up to a certain field. However, it smoothly starts to decrease with the increasing magnetic field at higher fields. Since Weyl points are not expected to exist in the AF-II regime, the positive LMC at the low field may arise due to the weak localization in the compound [127, 128]. Furthermore, we will see in the next section that the magnitude of θMC , at 4 K, for these two compounds is nearly zero. This suggests that the conductivity of the sample is independent of the relative orientation

between the magnetic field and the electric field (or electric current). Therefore, the chiral anomaly has to vanish in the AF-II regime ($\alpha = 0.18, 0.22$; $T = 4$ K).

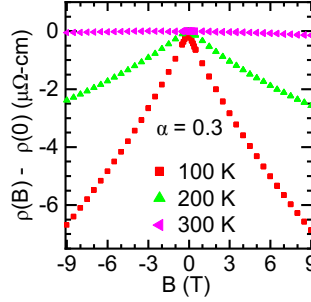


Figure 7.12: Longitudinal MR for the $\alpha = 0.30$ polycrystalline sample.

LMR in FM regime: MR with $B \parallel I$ was also measured for $\alpha = 0.30$ polycrystalline sample. Interestingly, negative LMR has been observed below T_c , as shown in the Fig. 7.12. We concluded in the last section that the compound with $\alpha = 0.30$ does not host Weyl Fermions. Also, negative longitudinal MR is very common in FM samples [99, 129]. Therefore, the negative LMR, in this case, does not originate from the chiral anomaly effect.

7.4.2.2 Angular magneto-conductivity

As mentioned in chapters 5 and 6, the magnetization of the parent and $\alpha = 0.22$ compounds, respectively, is nearly same within the x - y plane, and very different in magnitude within the x - z plane. A similar observation was made for the intermediate Fe doped compounds as well. Therefore, in order to avoid (anisotropic) magnetization driven angular magneto-conductivity (θ MC), the θ MC was measured within the x - y plane, with magnetic field changing angle (θ) with the electric current direction, as shown in Fig. 7.13(a). In this case, the current was applied along the x axis, and the magnetic field was rotated from the x axis, towards the y axis. The measurements were performed for $\alpha = 0 - 0.22$ at different temperatures in AF-I and AF-II regimes. Significant magnitude of θ MC signal was observed in at 4 K (for $\alpha \leq 0.10$), and 150 K (for $\alpha \leq 0.22$) as shown in the Fig. 7.13(a, b).

In the case of Weyl semimetals with very small magneto-conductivity ($\leq 1\%$), chiral

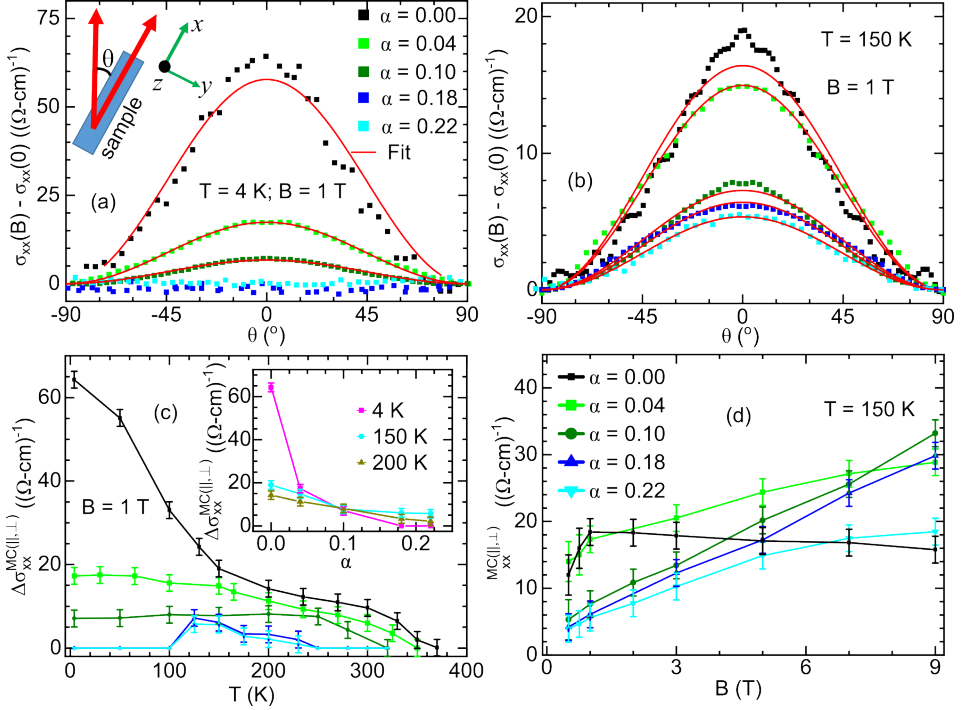


Figure 7.13: θ MC measurements for $\alpha = 0 - 0.22$ with magnetic field and electric current applied along the x axis. (a, b) θ MC measurements, at 1 T, are compared for different compounds, at 4 K and 150 K, respectively. The schematic of the measurement setup is also shown in (a). (c) Temperature dependence of the magnitude of θ MC oscillations ($\Delta\sigma_{xx}^{\text{MC}(\parallel,\perp)}$) corresponding to the different samples. Here, $\Delta\sigma_{xx}^{\text{MC}(\parallel,\perp)} = \sigma(0^\circ) - \sigma(90^\circ)$ at the mentioned temperature and magnetic field. Inset: Variation of the magnitude of the oscillations with an increase in Fe doping compared at different temperatures. (d) Magnetic field dependence of the magnitude of the θ MC oscillations corresponding to the $\alpha \leq 0.22$ compounds.

anomaly induced θMC follows [48, 46, 91]:

$$\sigma_{xx}(\theta) - \sigma_{xx}(\perp) = \Delta\sigma_{xx}^{\text{MC}(\parallel,\perp)} \cos^2\theta \quad (7.1)$$

Where $\Delta\sigma_{xx}^{\text{MC}(\parallel,\perp)}$ signifies the difference between longitudinal conductivity when magnetic field is applied parallel (\parallel) and perpendicular (\perp) to the current ($\Delta\sigma_{xx}^{\text{MC}(\parallel,\perp)} = \sigma_{xx}^{\parallel} - \sigma_{xx}^{\perp}$). The θMC for different Fe doped samples can be fitted with Eqn. (7.1), at 4 K and 150 K, as shown in the Fig. 7.13(a, b). For convenience, the magnitude of the θMC oscillations ($\Delta\sigma_{xx}^{\text{MC}(\parallel,\perp)}$), at different temperatures, corresponding to the different samples is shown in Fig. 7.13(c). It can be seen that the positive θMC is observed below $T_{\text{N}1}$. for $\alpha = 0, 0.04, 0.10$, down to the 4 K. However, for $\alpha = 0.18, 0.22$, positive θMC is observed between $T_{\text{N}2}$ and $T_{\text{N}1}$ only. It is also observed (inset of Fig. 7.13(c)) that the θMC magnitude decreases with an increase in Fe doping at 150 K, and 200 K, similar to the LMC. θMC decreases significantly with an increase in Fe doping. However, the magnetization of the doped compounds ($\alpha = (0-0.22)$) remains comparable to the Mn_3Ge , which suggests that the magnetization of the sample has negligible contribution to the observed θMC . These observations, in addition to the fact that AHE is observed in the AF-I regime only, suggest the origin of positive θMC in the AF-I regime to be the chiral anomaly effect, as observed in the case of Mn_3Sn and Mn_3Ge as well [82, 90].

We would like to mention that the positive θMC can be observed for halfmetallic/semimetallic systems also [99, 49]. As mentioned in the previous section, the role of trivial magneto-conductivity due to semimetallic nature of the sample, cannot be neglected. Therefore, as mentioned previously, further theoretical calculations are required to justify the effect of the chiral anomaly effect on the observed θMC in the AF-I regime.

As shown in Fig. 7.13(d), the field dependence of θMC at 150 K, where all the compounds are in the AF-I regime, shows an almost linear increase for $\alpha \geq 0.04$, which suggest type II nature of the Weyl points present in Fe doped samples [46], similar to the Mn_3Ge (Chapter 5).

7.4.2.3 Planar Hall effect

Observation of the large planar Hall effect (PHE) is another crucial signature of the chiral anomaly effect [45, 46]. PHE for $\alpha = 0 - 0.22$ is measured when transverse voltage is measured while rotating the magnetic field within the sample plane as

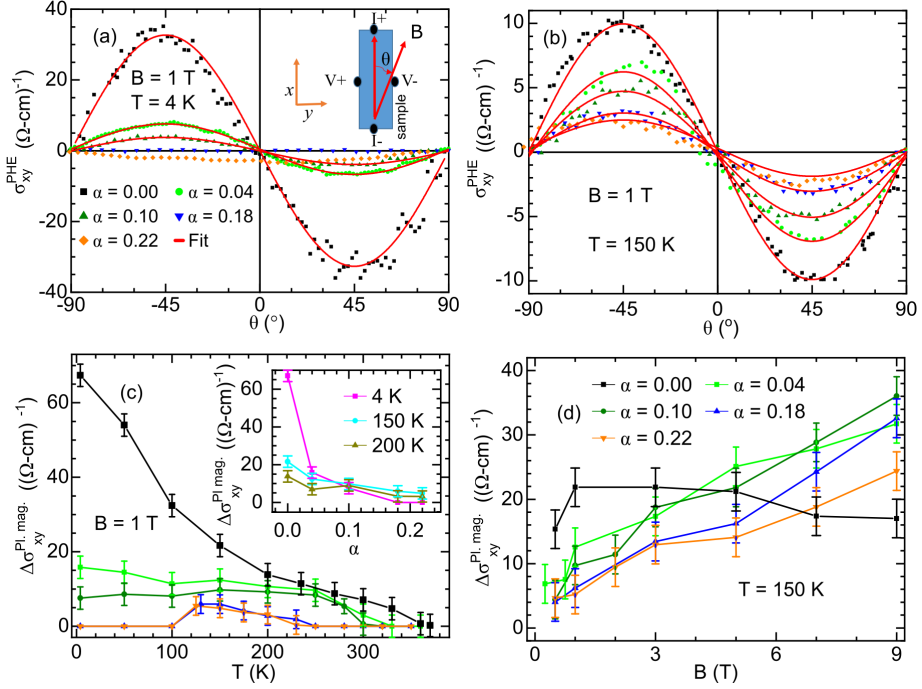


Figure 7.14: (a, b) Planar Hall effect measurement (PHE) of the Fe doped samples at 4 K and 150 K, respectively. A schematic of the experimental setup is shown in (a), where the sample is rotated such that the magnetic field makes an angle θ with the current direction. (c) Here, $\Delta\sigma_{xx}^{\text{Pl. mag.}}$ denote the magnitude of oscillations determined by the data fitting using Eqn. (7.2). Temperature dependence of the $\Delta\sigma_{xx}^{\text{Pl. mag.}}$ corresponding to different compounds mentioned in the plot. Inset: Evolution of the PHE magnitude, at different temperatures, with Fe doping fraction. (d) Magnetic field dependence of the magnitude of PHE oscillations for the $\alpha \leq 0.22$ compounds.

shown in Fig. 7.14(a). In the case of normal metals, no PHE signal is expected to be observed. However, in the case of Weyl semimetals, sinusoidal oscillations with 180° periodicity are expected to be observed [43, 46, 91].

We have measured PHE of $\alpha = 0, 0.04, 0.10, 0.18, 0.22$ compounds at several temperatures within the x - y plane. It was observed that PHE at 4 K is present for $\alpha = 0, 0.04, 0.10$, and vanishes for $\alpha = 0.18, 0.22$ (Fig. 7.14(a)). However, clear PHE oscillations were observed at 150 K for all the compounds ($\alpha = 0 - 0.22$), as shown in the Fig. 7.14(b). In the case of chiral anomaly, PHE follows:

$$\sigma_{xy}^{\text{PHE}} = \Delta\sigma_{xx}^{\text{Pl. mag.}} \sin\theta \cos\theta \quad (7.2)$$

Here, $\Delta\sigma_{xx}^{\text{Pl. mag.}}$ corresponds to twice of the magnitude of the PHE ($2[\sigma(-45^\circ) - \sigma(0^\circ)]$). Ideally, $\Delta\sigma_{xx}^{\text{Pl. mag.}} = \Delta\sigma_{xx}^{\text{MC}(\parallel, \perp)}$, as θMC and PHE shares the common origin - chiral anomaly effect [46]. PHE oscillations can be fitted with Eqn. (7.2) as shown in the Fig. 7.14(a, b).

Temperature dependence of $\Delta\sigma_{xx}^{\text{Pl. mag.}}$ at 1 T corresponding to the $\alpha = 0 - 0.22$ is shown in the Fig. 7.14(c), which also looks very similar to the temperature dependence of θMC . PHE signal decreases significantly with an increase in doping, and it is present only within the AF-I regime. The evolution of magnitude of the PHE, $\Delta\sigma_{xx}^{\text{Pl. mag.}}$, with α , at constant temperature and field is shown in the inset of the Fig. 7.14(c). As expected, on the basis of temperature dependent θMC , the $\Delta\sigma_{xx}^{\text{Pl. mag.}}$ decreases significantly with the increase in Fe doping. The α dependence of $\Delta\sigma_{xx}^{\text{Pl. mag.}}$ is very similar in nature as $\Delta\sigma_{xx}^{\text{MC}(\parallel, \perp)}$ (compare the insets of Figs. (7.13(c), 7.14(c)) Similar to the θMC , the magnitude of PHE at 150 K also increases almost linearly with an increase in the magnetic field as shown in the Fig. 7.14(d).

The field, temperature and α dependence of PHE magnitude look very similar to that of the θMC (7.13(c, d)), which is expected because of their common origin. Temperature dependence of $\Delta\sigma_{xx}^{\text{Pl. mag.}}$ at 1 T (Fig. 7.13(c)) clearly suggest that the $\Delta\sigma_{xx}^{\text{Pl. mag.}}$ remains non-zero only within the AF-I regime, which suggests its probable origin to be the chiral anomaly effect.

Since AHE, positive LMC, θMC , and PHE are observed only within the AF-I regime, Weyl points and the resulting chiral anomaly effect are very likely to be present in the AF-I regime of the compounds with $\alpha = 0 - 0.22$. The strength of chiral anomaly decreases with an increase in the gap between Weyl points and chemical potential [48]. Therefore, the decrease in the magnitude of LMC, θMC , and PHE

oscillations with doping signifies that the Weyl points are moving significantly away from the chemical potential with the substitution of Fe in Mn_3Ge .

7.5 Conclusion

Magnetization of several Fe doped Mn_3Ge samples suggests that the Mn_3Ge type magnetic structure persists up to 26% Fe doping in the AF-I regime. Electrical transport properties of $\alpha = 0 - 0.30$ compounds are also studied in detail. AHE was observed for $\alpha = 0 - 0.22$ in the AF-I regime only, which implies that the Weyl Fermions most likely exist in the Fe doped compounds as well. The anomalous Hall conductivity decreases rapidly with an increase in Fe doping, which, primarily, implies that the separation of the Weyl nodes decreases with Fe substitution. Further, the observation of positive LMC, θMC , and PHE, only in the AF-I regime, suggest their most probable origin to be the chiral anomaly effect. However, the role of semimetallic nature of the Fe doped compounds on various MC cannot be neglected. Further theoretical calculations are required to justify the role of the chiral anomaly effect on the observed LMC. The magnitude of LMC and various oscillations decreases consistently with an increase in Fe doping, possibly due to the increasing gap between the Weyl nodes and the chemical potential, as Fe doping is increased [48, 91, 90]. In short, we can conclude that the Weyl points can be tuned by the suitable dopant of the parent Weyl semimetal. Also, the vanishing nature of intrinsic AHE and chiral anomaly in AF-II and FM regimes suggests that the Weyl points and induced transport phenomena are intimately connected with the magnetic symmetry of the compound.

8 Summary and outlook

8.1 Summary

We have studied the transport and magnetic properties of the parent and Fe doped Mn_3Ge to determine the dynamics and stability of the Weyl points. First of all, we performed a detailed analysis of the electrical transport measurements of Mn_3Ge in the a - b and a - c planes to look for the presence of chiral anomaly, which is one of the most prominent signatures of the existence of Weyl points. We observed chiral anomaly induced negative longitudinal magneto-resistance (LMR) along all the axes, within a certain field regime. In contrast to the low field, high field LMR along the x axis is governed by the metallic and semimetallic nature of the compound, below and above 200 K, respectively. Carrier concentration type, high field MR, and θMR changes sign near 200 K. Since all these effects are governed by the electronic band structure and DOS near the Fermi surface, it is very likely that the Mn_3Ge goes through an electronic (topological) transition near the 200 K. Furthermore, the neutron diffraction measurement did not show any anomaly in the magnetic structure or magnetic moment, below 300 K. However, the temperature dependent lattice parameters show a maximum near 230 K, which is unusual. Since the electronic band structure is very sensitive to the lattice parameters, it can be argued that the change in the nature of electrical transport effects is governed by the lattice parameters of the compound.

Mn_3Ge samples with low Mn composition show large anomalous Hall effects (AHE) up to room temperature, which concludes that Weyl points are well separated and located significantly close to the Fermi surface. However, a decrease in AHE and a lower chiral anomaly effect are observed as Mn concentration is increased, which suggests that the location of Weyl points can be tuned relative to the Fermi surface as Mn concentration is changed.

Fe doped Mn_3Ge compounds were synthesized in order to observe the evolution of separation between a pair of Weyl points, and their location with respect to the Fermi surface. One of the main advantages of the study of these samples is the fact that the magnetic structure of samples up to 26% Fe doping remains the same as Mn_3Ge , in a certain temperature regime. This provides us with a large range of samples with very different characteristics of Weyl points but having the same magnetic structure which allows the Weyl points to exist because of broken time reversal symmetry.

While studying the samples up to 22% Fe doping, we have observed an anomalous Hall effect, which decays significantly as doping concentration increases. Clear

signatures of the LMC, θ MC, and PHE are observed only in the temperature and doping range where the Mn_3Ge type magnetic structure persists. The magnitude of anomalous Hall conductivity, planar Hall effect, and positive longitudinal magnetoconductance drop as Fe doping increases to $\alpha = 0.22$. These observations strongly suggest that the Weyl points are very likely to exist in the doped compounds within the AF-I regime. Furthermore, the separation between a pair of Weyl points decreases, and Weyl points move farther away from the Fermi surface as Fe doping increases. Therefore, we can conclude that the characteristics of Weyl points can be significantly tuned by the suitable dopant of the parent phase.

8.2 Outlook

As suggested in the chapter 5, spin-resolved density of states (SDOS) calculation for Mn_3Ge needs to be performed to confirm the origin of high field LMR along the x axis. Moreover, SDOS needs to be calculated for low Fe doped Mn_3Ge compounds as well to determine the location of the Weyl points. Reduced AHE is observed upon Fe doping, however, it is not clear how far the Weyl points move away from the Fermi surface, and how much the separation between a pair of the Weyl points decreases with the Fe doping. Therefore, detailed theoretical calculations are required to substantiate our qualitative observations.

Electrical transport effects show that the Weyl points are likely to persist in the Fe doped Mn_3Ge compounds. Compared to the electric transport measurements, thermal transport measurements are much more sensitive to the Weyl points located nearest to the Fermi surface. Therefore, thermal transport measurements, like the Nernst effect, should be performed to probe the local dynamics of the Weyl points located closest to the Fermi surface. Magneto-optical Kerr effect measurements of the doped compounds can be performed to further strengthen the claim for the presence of Weyl points in doped compounds. Since Weyl points are very likely to persist in the Fe doped Mn_3Ge compounds, angle-resolved photoemission spectroscopy (ARPES) needs to be done to experimentally verify the presence of Weyl points.

Fe doping in Mn_3Ge work as electron doping in the compound, which changes the Fermi surface such that the AHE is reduced in the doped compounds. Therefore, the evolution of the magnetic and transport properties of Mn_3Ge should also be studied with hole doping in Mn_3Ge . One of the possible candidates for hole doping could be Cr. It would be very interesting to observe how Weyl points evolve with the decrease

in the electron carrier concentration in the compound.

Bibliography

- [1] S. Nakatsuji, N. Kiyohara, and T. Higo. Large anomalous Hall effect in a non-collinear antiferromagnet at room temperature. *Nature*, 527(7577):212–215, 2015.
- [2] G. Chang, B. Singh, S.-Y. Xu, G. Bian, S.-M. Huang, C.-H. Hsu, I. Belopolski, N. Alidoust, D. S. Sanchez, H. Zheng, et al. Magnetic and noncentrosymmetric Weyl Fermion semimetals in the $R\text{AlGe}$ family of compounds (R = rare earth). *Phys. Rev. B*, 97(4):041104, 2018.
- [3] T. Machon and G. P. Alexander. Knots and nonorientable surfaces in chiral nematics. *Proc. Natl. Acad. Sci.*, 110(35):14174–14179, 2013.
- [4] J. E. Moore. The birth of topological insulators. *Nature*, 464(7286):194–198, 2010.
- [5] F. Haldane and Duncan M. Model for a quantum Hall effect without landau levels- condensed-matter realization of the parity anomaly. *Phys. Rev. Lett.*, 61(18):2015, 1988.
- [6] M. Z. Hasan and C. L. Kane. Colloquium: topological insulators. *Rev. Mod. Phys.*, 82(4):3045, 2010.
- [7] X.-L. Qi and S.-C. Zhang. Topological insulators and superconductors. *Rev. Mod. Phys.*, 83(4):1057, 2011.
- [8] B. Yan and C. Felser. Topological materials: Weyl semimetals. *Annu. Rev. Condens. Matter Phys.*, 8:337–354, 2017.
- [9] G. Sharma, P. Goswami, and S. Tewari. Chiral anomaly and longitudinal magnetotransport in type-II Weyl semimetals. *Phys. Rev. B*, 96(4):045112, 2017.

- [10] M. König, S. Wiedmann, C. Brune, A. Roth, H. Buhmann, Laurens W. M., X.-L. Qi, and S.-C. Zhang. Quantum spin Hall insulator state in HgTe quantum wells. *Science*, 318(5851):766–770, 2007.
- [11] Z. Wang, X.-L. Qi, and S.-C. Zhang. Equivalent topological invariants of topological insulators. *New J. Phys.*, 12(6):065007, 2010.
- [12] H. Zhang, C.-X. Liu, X.-L. Qi, X. Dai, Z. Fang, and S.-C. Zhang. Topological insulators in Bi₂Se₃, Bi₂Te₃ and Sb₂Te₃ with a single Dirac cone on the surface. *Nat. Phys.*, 5(6):438–442, 2009.
- [13] B. A. Bernevig, T. L. Hughes, and S.-C. Zhang. Quantum spin Hall effect and topological phase transition in HgTe quantum wells. *Science*, 314(5806):1757–1761, 2006.
- [14] L. Fu and C. L. Kane. Topological insulators with inversion symmetry. *Phys. Rev. B*, 76(4):045302, 2007.
- [15] M. Z. Hasan and J. E. Moore. Three-dimensional topological insulators. *Annu. Rev. Condens. Matter Phys.*, 2(1):55–78, 2011.
- [16] S.-Y. Yang, H. Yang, E. Derunova, S. S. P. Parkin, B. Yan, and M. N. Ali. Symmetry demanded topological nodal-line materials. *Advances in Physics: X*, 3(1):1414631, 2018.
- [17] A. A. Burkov, M. D. Hook, and L. Balents. Topological nodal semimetals. *Phys. Rev. B*, 84(23):235126, 2011.
- [18] J. Hu, S.-Y. Xu, N. Ni, and Z. Mao. Transport of topological semimetals. *Annu. Rev. Mater. Res.*, 49:207–252, 2019.
- [19] L. S. Xie, L. M. Schoop, E. M. Seibel, Q. D. Gibson, W. Xie, and R. J. Cava. A new form of Ca₃P₂ with a ring of Dirac nodes. *APL Mater.*, 3(8):083602, 2015.
- [20] L. M. Schoop, M. N. Ali, C. Straßer, A. Topp, A. Varykhalov, D. Marchenko, V. Duppel, S. S. P. Parkin, B. V. Lotsch, and C. R. Ast. Dirac cone protected by non-symmorphic symmetry and three-dimensional Dirac line node in ZrSiS. *Nat. Commun.*, 7(1):1–7, 2016.

-
- [21] Z. K. Liu, B. Zhou, Y. Zhang, Z. J. Wang, H. M. Weng, D. Prabhakaran, S.-K. Mo, Z. X. Shen, Z. Fang, X. Dai, et al. Discovery of a three-dimensional topological Dirac semimetal, Na_3Bi . *Science*, 343(6173):864–867, 2014.
- [22] S.-Y. Xu, Y. Xia, L. A. Wray, S. Jia, F. Meier, J. H. Dil, J. Osterwalder, B. Slomski, A. Bansil, H. Lin, et al. Topological phase transition and texture inversion in a tunable topological insulator. *Science*, 332(6029):560–564, 2011.
- [23] N. P. Armitage, E. J. Mele, and A. Vishwanath. Weyl and Dirac semimetals in three-dimensional solids. *Rev. Mod. Phys.*, 90(1):015001, 2018.
- [24] K.-Y. Yang, Y.-M. Lu, and Y. Ran. Quantum Hall effects in a Weyl semimetal: Possible application in pyrochlore iridates. *Phys. Rev. B*, 84(7):075129, 2011.
- [25] A. A. Burkov. Topological semimetals. *Nat. Mater.*, 15(11):1145–1148, 2016.
- [26] T. M. McCormick. *Electronic and Transport Properties of Weyl Semimetals*. PhD thesis, The Ohio State University, 2018.
- [27] A. A. Zyuzin, S. Wu, and A. A. Burkov. Weyl semimetal with broken time reversal and inversion symmetries. *Phys. Rev. B*, 85(16):165110, 2012.
- [28] S.-M. Huang, S.-Y. Xu, I. Belopolski, C.-C. Lee, G. Chang, B. Wang, N. Alidoust, G. Bian, M. Neupane, C. Zhang, et al. A Weyl fermion semimetal with surface Fermi arcs in the transition metal monpnictide TaAs class. *Nat. Commun.*, 6(1):1–6, 2015.
- [29] S.-Y. Xu, I. Belopolski, N. Alidoust, M. Neupane, G. Bian, C. Zhang, R. Sankar, G. Chang, Z. Yuan, C.-C. Lee, et al. Discovery of a Weyl Fermion semimetal and topological Fermi arcs. *Science*, 349(6248):613–617, 2015.
- [30] D. J. Griffiths and D. F. Schroeter. *Introduction to quantum mechanics*. Cambridge university press, 2018.
- [31] M. V. Berry. Quantal phase factors accompanying adiabatic changes. *Proc. R. Soc. A: Math. Phys. Eng. Sci.*, 392(1802):45–57, 1984.
- [32] L. Šmejkal, Y. Mokrousov, B. Yan, and A. H. MacDonald. Topological antiferromagnetic spintronics. *Nat. Phys.*, 14(3):242–251, 2018.

- [33] H. Li, H. He, H.-Z. Lu, H. Zhang, H. Liu, R. Ma, Z. Fan, S.-Q. Shen, and J. Wang. Negative magnetoresistance in Dirac semimetal Cd_3As_2 . *Nat. Commun.*, 7(1):1–7, 2016.
- [34] N. Nagaosa, J. Sinova, S. Onoda, A. H. MacDonald, and N. P. Ong. Anomalous Hall effect. *Rev. Mod. Phys.*, 82(2):1539, 2010.
- [35] L. Šmejkal, T. Jungwirth, and J. Sinova. Route towards Dirac and Weyl antiferromagnetic spintronics. *Phys. Status Solidi Rapid Res. Lett.*, 11(4):1700044, 2017.
- [36] A. A. Burkov. Anomalous Hall effect in Weyl metals. *Phys. Rev. Lett.*, 113(18):187202, 2014.
- [37] N. Kiyohara, T. Tomita, and S. Nakatsuji. Giant anomalous Hall effect in the chiral antiferromagnet Mn_3Ge . *Phys. Rev. Appl.*, 5(6):064009, 2016.
- [38] H. B. Nielsen and M. Ninomiya. The Adler-Bell-Jackiw anomaly and Weyl fermions in a crystal. *Phys. Lett. B*, 130(6):389–396, 1983.
- [39] J. Xiong, S. K. Kushwaha, T. Liang, J. W. Krizan, M. Hirschberger, W. Wang, R. J. Cava, and N. P. Ong. Evidence for the chiral anomaly in the Dirac semimetal Na_3Bi . *Science*, 350(6259):413–416, 2015.
- [40] S. Liang, J. Lin, S. Kushwaha, J. Xing, N. Ni, R. J. Cava, and N. P. Ong. Experimental tests of the chiral anomaly magnetoresistance in the Dirac-Weyl semimetals Na_3Bi and GdPtBi . *Phys. Rev. X*, 8(3):031002, 2018.
- [41] S. Wang, B.-C. Lin, A.-Q. Wang, D.-P. Yu, and Z.-M. Liao. Quantum transport in Dirac and Weyl semimetals: a review. *Adv. Phys.: X*, 2(3):518–544, 2017.
- [42] P. Hosur and X. Qi. Recent developments in transport phenomena in Weyl semimetals. *C. R. Phys.*, 14(9-10):857–870, 2013.
- [43] A. A. Burkov. Giant planar Hall effect in topological metals. *Phys. Rev. B*, 96(4):041110, 2017.
- [44] D. T. Son and B. Z. Spivak. Chiral anomaly and classical negative magnetoresistance of Weyl metals. *Phys. Rev. B*, 88(10):104412, 2013.

-
- [45] A. A. Burkov. Chiral anomaly and diffusive magnetotransport in Weyl metals. *Phys. Rev. Lett.*, 113(24):247203, 2014.
- [46] S. Nandy, G. Sharma, A. Taraphder, and S. Tewari. Chiral anomaly as the origin of the planar Hall effect in Weyl semimetals. *Phys. Rev. Lett.*, 119(17):176804, 2017.
- [47] N. Kumar, S. N. Guin, C. Felser, and C. Shekhar. Planar Hall effect in the Weyl semimetal GdPtBi. *Phys. Rev. B*, 98(4):041103, 2018.
- [48] M.-X. Deng, J.-Y. Ba, R. Ma, W. Luo, R.-Q. Wang, L. Sheng, and D. Y. Xing. Chiral-anomaly-induced angular narrowing of the positive longitudinal magnetoconductivity in Weyl semimetals. *Phys. Rev. Res.*, 2(3):033346, 2020.
- [49] F. J. Yang, Y. Sakuraba, S. Kokado, Y. Kota, A. Sakuma, and K. Takanashi. Anisotropic magnetoresistance in $\text{Co}_2(\text{Fe}, \text{Mn})\text{Si}$ heusler epitaxial films: A fingerprint of half-metallicity. *Phys. Rev. B*, 86(2):020409, 2012.
- [50] C.-L. Zhang, S.-Y. Xu, I. Belopolski, Z. Yuan, Z. Lin, B. Tong, G. Bian, N. Alidoust, C.-C. Lee, S.-M. Huang, et al. Signatures of the Adler–Bell–Jackiw chiral anomaly in a Weyl Fermion semimetal. *Nat. Commun.*, 7(1):1–9, 2016.
- [51] H. Yang, Y. Sun, Y. Zhang, W.-J. Shi, S. S. P. Parkin, and B. Yan. Topological Weyl semimetals in the chiral antiferromagnetic materials Mn_3Ge and Mn_3Sn . *New J. Phys.*, 19(1):015008, 2017.
- [52] J.-R. Soh, F. de Juan, N. Qureshi, H. Jacobsen, H.-Y. Wang, Y.-F. Guo, and A. T. Boothroyd. Ground-state magnetic structure of Mn_3Ge . *Phys. Rev. B*, 101(14):140411, 2020.
- [53] P. J. Brown, V. Nunez, F. Tasset, J. B. Forsyth, and P. Radhakrishna. Determination of the magnetic structure of Mn_3Sn using generalized neutron polarization analysis. *J. Phys. Condens. Matter.*, 2(47):9409, 1990.
- [54] G. Chaudhary, A. A. Burkov, and O. G. Heinonen. Magnetism and magnetotransport in the kagome antiferromagnet Mn_3Ge . *Phys. Rev. B*, 105(8):085108, 2022.
- [55] A. K. Nayak, J. E. Fischer, Y. Sun, B. Yan, J. Karel, Alexander C. K., C. Shekhar, N. Kumar, W. Schnelle, J. Kübler, et al. Large anomalous Hall

- effect driven by a nonvanishing berry curvature in the noncolinear antiferromagnet Mn_3Ge . *Sci. Adv.*, 2(4):e1501870, 2016.
- [56] C. Wuttke, F. Caglieris, S. Sykora, F. Scaravaggi, A. U. B. Wolter, K. Manna, V. Süß, C. Shekhar, C. Felser, B. Büchner, et al. Berry curvature unravelled by the anomalous Nernst effect in Mn_3Ge . *Phys. Rev. B*, 100(8):085111, 2019.
- [57] M. Wu, H. Isshiki, T. Chen, T. Higo, S. Nakatsuji, and Y. Otani. Magneto-optical Kerr effect in a non-collinear antiferromagnet Mn_3Ge . *Appl. Phys. Lett.*, 116(13):132408, 2020.
- [58] Th. Brückel. Atomic and magnetic structures in crystalline materials: Neutron and X-ray scattering. *ChemInform*, 39(32), 2008.
- [59] M. Angst, Th. Brückel, D. Richter, and R. Zorn. *Scattering methods for condensed matter research*. Number PreJuSER-136382. Streumethoden, 2012.
- [60] C. Cohen-Tannoudji, B. Diu, and F. Laloe. Quantum mechanics, volume 2. *Quantum Mechanics*, 2:626, 1986.
- [61] P. Edlund. *Structural Features of Bacteriophytochromes. Photoactivated Proteins studied by Serial Femtosecond Crystallography*. PhD thesis, University of Gothenburg, 2018.
- [62] P. J. Brown. Polarised neutrons and complex antiferromagnets: an overview. *Physica B Condens. Matter.*, 297(1-4):198–203, 2001.
- [63] Th. Brückel and W. Schweika. *Polarized neutron scattering: lectures of the 1st summer school held at the Forschungszentrum Jülich from 10 to 14 September 2002*. Number PreJuSER-5925. Streumethoden, 2002.
- [64] M. Blume. Polarization effects in the magnetic elastic scattering of slow neutrons. *Phys. Rev.*, 130(5):1670, 1963.
- [65] H. Zong. *Magnetic Characterization of Powder Samples from the Magnetocaloric compound Series $\text{Mn}_{5-x}\text{Fe}_x\text{Si}$* . Forschungszentrum Jülich GmbH, Zentralbibliothek, 2016.
- [66] V. Q. Nguyen, J. Kim, and S. Cho. A review of SnSe : Growth and thermoelectric properties. *J. Korean Phys. Soc.*, 72(8):841–857, 2018.

-
- [67] <https://www.alineason.com/en/knowhow/crystal-growth/>.
- [68] F. Caruso, S. Mantellato, M. Palacios, and R. J. Flatt. ICP-OES method for the characterization of cement pore solutions and their modification by polycarboxylate-based superplasticizers. *Cem. Concr. Res.*, 91:52–60, 2017.
- [69] S. Adiga. *Crystal growth and scattering studies on two ferrites*. Forschungszentrum Jülich GmbH, Zentralbibliothek, 2016.
- [70] <https://qdusa.com/products/versalab.html>.
- [71] S. Zherlitsyn, B. Wustmann, T. Herrmannsdorfer, and J. Wosnitza. Status of the pulsed-magnet-development program at the dresden high magnetic field laboratory. *IEEE Trans. Appl. Supercond.*, 22(3):4300603–4300603, 2012.
- [72] M. Ghorbani-Zavareh. *Direct Measurements of the Magnetocaloric Effect in Pulsed Magnetic Fields*. PhD thesis, Technischen Universität Dresden, 2016.
- [73] <https://www.ill.eu/users/instruments/instruments-list/d23/description/instrument-layout>.
- [74] <https://mlz-garching.de/englisch/news-und-press/news-articles/georg-roth-honored-for-his-outstanding-contributions-to-mlz.html>.
- [75] F. Tasset, P. J. Brown, and J. B. Forsyth. Determination of the absolute magnetic moment direction in Cr_2O_3 using generalized polarization analysis. *J. Appl. Phys.*, 63(8):3606–3608, 1988.
- [76] <https://www.ill.eu/users/instruments/instruments-list/d3/how-it-works/spherical-polarimetry-with-cryopad>.
- [77] J.-R. Soh. *Magnetism in topological materials*. PhD thesis, University of Oxford, 2019.
- [78] N. Qureshi. Mag2pol: A program for the analysis of spherical neutron polarimetry, flipping ratio and integrated intensity data. *J. Appl. Crystallogr.*, 52(1):175–185, 2019.
- [79] A. B. Gokhale and R. Abbaschian. The Ge-Mn (Germanium-Manganese) system. *J. Ph. Equilibria Diffus.*, 11(5):460–468, 1990.

- [80] Y. Chen, J. Gaudet, S. Dasgupta, G. G. Marcus, J. Lin, T. Chen, T. Tomita, M. Ikhlas, Y. Zhao, W. C. Chen, et al. Antichiral spin order, its soft modes, and their hybridization with phonons in the topological semimetal Mn_3Ge . *Phys. Rev. B*, 102(5):054403, 2020.
- [81] H. Okamoto. Fe-Ge (Iron-Germanium). *J. Phase Equilibria Diffus.*, 29(3):292, 2008.
- [82] K. Kuroda, T. Tomita, M.-T. Suzuki, C. Bareille, A. A. Nugroho, P. Goswami, M. Ochi, M. Ikhlas, M. Nakayama, S. Akebi, et al. Evidence for magnetic Weyl Fermions in a correlated metal. *Nat. Mater.*, 16(11):1090–1095, 2017.
- [83] E. Liu, Y. Sun, N. Kumar, L. Muechler, A. Sun, L. Jiao, S.-Y. Yang, D. Liu, A. Liang, Q. Xu, et al. Giant anomalous Hall effect in a ferromagnetic kagome-lattice semimetal. *Nat. Phys.*, 14(11):1125–1131, 2018.
- [84] C. Shekhar, N. Kumar, V. Grinenko, S. Singh, R. Sarkar, H. Luetkens, S.-C. Wu, Y. Zhang, A. C. Komarek, E. Kampert, et al. Anomalous Hall effect in Weyl semimetal half-heusler compounds RPtBi ($\text{R} = \text{Gd}$ and Nd). *Proc. Natl. Acad. Sci. USA*, 115(37):9140–9144, 2018.
- [85] E. Krén and G. Kádár. Neutron diffraction study of Mn_3Ga . *Solid State Commun.*, 8(20):1653–1655, 1970.
- [86] S. Tomiyoshi and Y. Yamaguchi. Magnetic structure and weak ferromagnetism of Mn_3Sn studied by polarized neutron diffraction. *J. Phys. Soc. Jpn.*, 51(8):2478–2486, 1982.
- [87] S. Tomiyoshi, Y. Yamaguchi, and T. Nagamiya. Triangular spin configuration and weak ferromagnetism of Mn_3Ge . *J. Magn. Magn. Mater.*, 31:629–630, 1983.
- [88] T. Nagamiya, S. Tomiyoshi, and Y. Yamaguchi. Triangular spin configuration and weak ferromagnetism of Mn_3Sn and Mn_3Ge . *Solid State Commun.*, 42(5):385–388, 1982.
- [89] L. Xu, X. Li, X. Lu, C. Collignon, H. Fu, J. Koo, B. Fauqué, B. Yan, Z. Zhu, and K. Behnia. Finite-temperature violation of the anomalous transverse wiedemann-franz law. *Sci. Adv.*, 6(17):eaaz3522, 2020.

-
- [90] T. Chen, T. Tomita, S. Minami, M. Fu, T. Koretsune, M. Kitatani, I. Muhammad, D. Nishio-Hamane, R. Ishii, F. Ishii, et al. Anomalous transport due to Weyl Fermions in the chiral antiferromagnets Mn_3X , $\text{X} = \text{Sn}, \text{Ge}$. *Nat. Commun.*, 12(1):1–14, 2021.
 - [91] A. A. Burkov and Y. B. Kim. \mathbb{Z}_2 and chiral anomalies in topological Dirac semimetals. *Phys. Rev. Lett.*, 117(13):136602, 2016.
 - [92] F. L. Zeng, Z. Y. Ren, Y. Li, J. Y. Zeng, M. W. Jia, J. Miao, A. Hoffmann, W. Zhang, Y. Z. Wu, and Z. Yuan. Intrinsic mechanism for anisotropic magnetoresistance and experimental confirmation in $\text{Co}_x\text{Fe}_{1-x}$ single-crystal films. *Phys. Rev. Lett.*, 125(9):097201, 2020.
 - [93] B. J. Ramshaw, K. A. Modic, A. Shekhter, Y. Zhang, E.-A. Kim, P. J. W. Moll, M. D. Bachmann, M. K. Chan, J. B. Betts, F. Balakirev, et al. Quantum limit transport and destruction of the Weyl nodes in TaAs. *Nat. Commun.*, 9(1):1–9, 2018.
 - [94] H. Roth, W. D. Straub, W. Bernard, and J. E. Mulhern Jr. Empirical characterization of low-temperature magnetoresistance effects in heavily doped Ge and Si. *Phys. Rev. Lett.*, 11(7):328, 1963.
 - [95] Y. Furukawa. Magnetoresistance in heavily doped n-type Germanium. *J. Phys. Soc. Jpn.*, 17(4):630–638, 1962.
 - [96] A. Kawabata. Theory of negative magnetoresistance I. application to heavily doped semiconductors. *J. Phys. Soc. Jpn.*, 49(2):628–637, 1980.
 - [97] A. B. Pippard. *Magnetoresistance in metals*, volume 2. Cambridge university press, 1989.
 - [98] T. Endo, H. Kubota, and T. Miyazaki. Magnetoresistance of $\text{Co}_2\text{MnAl}_{1-x}\text{Si}_x$ heusler alloys. *J. Magn. Soc. Jpn.*, 23:1129–1132, 1999.
 - [99] S. Kokado, M. Tsunoda, K. Harigaya, and A. Sakuma. Anisotropic magnetoresistance effects in Fe, Co, Ni, Fe_4N , and half-metallic ferromagnet: A systematic analysis. *J. Phys. Soc. Jpn.*, 81(2):024705, 2012.

- [100] X. Sun, W. Li, X. Wang, Q. Sui, T. Zhang, Z. Wang, L. Liu, D. Li, S. Feng, S. Zhong, et al. Room temperature ferromagnetism in ultra-thin van der waals crystals of 1T-CrTe₂. *Nano Res.*, 13(12):3358–3363, 2020.
- [101] R. Singha, S. Roy, A. Pariari, B. Satpati, and P. Mandal. Planar Hall effect in the type-II Dirac semimetal VAl₃. *Phys. Rev. B*, 98(8):081103, 2018.
- [102] T. McGuire and R. L. Potter. Anisotropic magnetoresistance in ferromagnetic 3d alloys. *IEEE Trans. Magn.*, 11(4):1018–1038, 1975.
- [103] B. C. Sales, R. Jin, D. Mandrus, and P. Khalifah. Anomalous Hall effect in three ferromagnetic compounds: EuFe₄Sb₁₂, Yb₁₄MnSb₁₁, and Eu₈Ga₁₆Ge₃₀. *Phys. Rev. B*, 73(22):224435, 2006.
- [104] X. Wang, D. Pan, Q. Zeng, X. Chen, H. Wang, D. Zhao, Z. Xu, Q. Yang, J. Deng, T. Zhai, et al. Robust anomalous Hall effect and temperature-driven lifshitz transition in Weyl semimetal Mn₃Ge. *Nanoscale*, 13(4):2601–2608, 2021.
- [105] V. Petříček, M. Dušek, and Palatinus. L. Crystallographic Computing System JANA2006: General features. *Z. Krist.*, 229(5):345–352, 2014.
- [106] A. S. Sukhanov, S. Singh, L. Caron, Th. Hansen, A. Hoser, V. Kumar, H. Borrmann, A. Fitch, P. Devi, K. Manna, et al. Gradual pressure-induced change in the magnetic structure of the noncollinear antiferromagnet Mn₃Ge. *Phys. Rev. B*, 97(21):214402, 2018.
- [107] Y. Song, Y. Qiao, Q. Huang, C. Wang, X. Liu, Q. Li, J. Chen, and X. Xing. Opposite thermal expansion in isostructural noncollinear antiferromagnetic compounds of Mn₃A (A= Ge and Sn). *Chem. Mater.*, 30(18):6236–6241, 2018.
- [108] B. Meng, H. Wu, Y. Qiu, C. Wang, Y. Liu, Z. Xia, S. Yuan, H. Chang, and Z. Tian. Large anomalous Hall effect in ferromagnetic Weyl semimetal candidate PrAlGe. *APL Mater.*, 7(5):051110, 2019.
- [109] K.-R. Jeon, B. K. Hazra, K. Cho, A. Chakraborty, J.-C. Jeon, H. Han, H. L. Meyerheim, T. Kontos, and S. S. P. Parkin. Long-range supercurrents through a chiral non-collinear antiferromagnet in lateral josephson junctions. *Nat. Mater.*, 20(10):1358–1363, 2021.

-
- [110] M. P. Ghimire, J. I. Facio, J.-S. You, L. Ye, J. G. Checkelsky, S. Fang, E. Kaxiras, M. Richter, and J. V. D. Brink. Creating Weyl nodes and controlling their energy by magnetization rotation. *Phys. Rev. Res.*, 1(3):032044, 2019.
- [111] R. D. Dos Reis, M. G. Zavareh, M. O. Ajeesh, L. O. Kutelak, A. S. Sukhanov, S. Singh, J. Noky, Y. Sun, J. E. Fischer, K. Manna, et al. Pressure tuning of the anomalous Hall effect in the chiral antiferromagnet Mn_3Ge . *Phys. Rev. Mater.*, 4(5):051401, 2020.
- [112] Z. H. Liu, Q. Q. Zhang, Y. J. Zhang, H. G. Zhang, X. Q. Ma, and E. K. Liu. Evolution of diverse Hall effects during the successive magnetic phase transitions in $\text{Mn}_{2.5}\text{Fe}_{0.6}\text{Sn}_{0.9}$ kagome-lattice alloy. *J. Phys. Condens. Matter.*, 33(11):115803, 2020.
- [113] J. Corps, P. Vaqueiro, A. Aziz, R. Grau-Crespo, W. Kockelmann, J.-C. Jumas, and A. V. Powell. Interplay of metal-atom ordering, fermi level tuning, and thermoelectric properties in cobalt shandites $\text{Co}_3\text{M}_2\text{S}_2$ ($\text{M} = \text{Sn}, \text{In}$). *Chem. Mater.*, 27(11):3946–3956, 2015.
- [114] Y. Yanagi, J. Ikeda, K. Fujiwara, K. Nomura, A. Tsukazaki, and M.-T. Suzuki. First-principles investigation of magnetic and transport properties in hole-doped shandite compounds $\text{Co}_3\text{In}_x\text{Sn}_{2-x}\text{S}_2$. *Phys. Rev. B*, 103(20):205112, 2021.
- [115] T. Hori, Y. Yamaguchi, and Y. Nakagawa. Antiferromagnetic to ferromagnetic transition of hexagonal $(\text{Mn}_{1-x}\text{Fe}_x)_3\text{Ge}$. *J. Magn. Magn.*, 104:2045–2046, 1992.
- [116] H. Niida, T. Hori, and Y. Nakagawa. Magnetic properties of $(\text{Mn}_{1-x}\text{Fe}_x)_{3+\delta}\text{Ge}$ alloys. *J. Magn. Magn. Mater.*, 140:129–130, 1995.
- [117] T. Hori, H. Niida, H. Kato, Y. Yamaguchi, and Y. Nakagawa. Magnetic phase transition in $\epsilon\text{-(Mn}_{1-x}\text{Fe}_x)_{3+\delta}\text{Ge}$. *Physica B Condens. Matter.*, 211(1-4):93–95, 1995.
- [118] K. Kanematsu. Magnetic properties of manganese, iron, and germanium, tin compounds with D_{019} type of structure. *Propriétés Thermodynamiques Physiques et Structurales des Dérivés Semi-Metalliques (CNRS, Paris)*, page 135, 1967.

- [119] Y. Lecocq, P. Locecq, and A. Michel. Influence du manganèse sur les propriétés magétiques et structurales du Germaniure de fer Fe_3Ge . *Compt. Rend.*, 256:4913, 1963.
- [120] W. J. Feng, D. Li, W. J. Ren, Y. B. Li, W. F. Li, J. Li, Y. Q. Zhang, and Z. D. Zhang. Glassy ferromagnetism in Ni_3Sn -type $\text{Mn}_{3.1}\text{Sn}_{0.9}$. *Phys. Rev. B*, 73(20):205105, 2006.
- [121] J. Kübler and C. Felser. Non-collinear antiferromagnets and the anomalous Hall effect. *Europhys. Lett.*, 108(6):67001, 2014.
- [122] H. Chen, Q. Niu, and A. H. MacDonald. Anomalous Hall effect arising from noncollinear antiferromagnetism. *Phys. Rev. Lett.*, 112(1):017205, 2014.
- [123] L. Šmejkal, R. González-Hernández, T. Jungwirth, and J. Sinova. Crystal time-reversal symmetry breaking and spontaneous Hall effect in collinear antiferromagnets. *Sci. Adv.*, 6(23):eaaz8809, 2020.
- [124] L. Šmejkal, A. H. MacDonald, J. Sinova, S. Nakatsuji, and T. Jungwirth. Anomalous Hall antiferromagnets. *Nat. Rev. Mater.*, 7(6):482–496, 2022.
- [125] Z. Feng, X. Zhou, L. Šmejkal, L. Wu, Z. Zhu, H. Guo, R. González-Hernández, X. Wang, H. Yan, P. Qin, et al. Observation of the anomalous Hall effect in a collinear antiferromagnet. *arXiv preprint arXiv:2002.08712*, 2020.
- [126] A. S. Wills. A new protocol for the determination of magnetic structures using simulated annealing and representational analysis (SARAh). *Phys. B: Condens. Matter.*, 276:680–681, 2000.
- [127] S. Hikami, A. I. Larkin, and Y. Nagaoka. Spin-orbit interaction and magnetoresistance in the two dimensional random system. *Prog. Theor. Phys.*, 63(2):707–710, 1980.
- [128] H.-Z. Lu and S.-Q. Shen. Weak localization and weak anti-localization in topological insulators. *Spintronics Vii*, 9167:263–273, 2014.
- [129] L. Ritchie, G. Xiao, Y. Ji, T. Y. Chen, C. L. Chien, M. Zhang, J. Chen, Z. Liu, G. Wu, and X. X. Zhang. Magnetic, structural, and transport properties of the heusler alloys Co_2MnSi and NiMnSb . *Phys. Rev. B*, 68(10):104430, 2003.

Band / Volume 257

**High-Performance Computing Approach to Hybrid Functionals
in the All-Electron DFT Code FLEUR**

M. Redies (2022), xi, 109 pp

ISBN: 978-3-95806-639-7

Band / Volume 258

**Establishing regulatable expression systems in the acetic acid bacterium
Gluconobacter oxydans 621H**

P. M. Fricke (2022), VIII, 187 pp

ISBN: 978-3-95806-642-7

Band / Volume 259

**Density-Functional Perturbation Theory within the All-Electron Full-
Potential Linearized Augmented Plane-Wave Method: Application to
Phonons**

C.-R. Gerhorst (2022), xvi, 317 pp

ISBN: 978-3-95806-649-6

Band / Volume 260

Crystal and Magnetic Structure of CrAs under Extreme Conditions

A. Eich (2022), viii, 235 pp

ISBN: 978-3-95806-655-7

Band / Volume 261

**Applications of transcription factor-based biosensors for strain
development and evolutionary engineering**

R. G. Stella (2022), x, 128 pp

ISBN: 978-3-95806-657-1

Band / Volume 262

**Strömungsmechanische Simulation und experimentelle Validierung
des kryogenen Wasserstoff-Moderators für die Europäische
Spallationsneutronenquelle ESS**

Y. Beßler (2022), XXIV, 154, xxxiii pp

ISBN: 978-3-95806-660-1

Band / Volume 263

**9th Georgian-German School and Workshop in Basic Science
September 12 – 16, 2022 | Kutaisi, Tbilisi | Georgia**

A. Kacharava, E. Portius, N. J. Shah, H. Ströher (2022)

ISBN: 978-3-95806-664-9

Band / Volume 264

Self-assembly of Au-Fe₃O₄ dumbbell nanoparticles

N. Nandakumaran (2022), xiv, 234 pp

ISBN: 978-3-95806-666-3

Band / Volume 265

Time-resolved and three-dimensional characterisation of magnetic states in nanoscale materials in the transmission electron microscope

T. Weßels (2023), xx, 211 pp

ISBN: 978-3-95806-685-4

Band / Volume 266

Dissecting iron and heme regulatory networks and adaptation to heme stress in *Corynebacterium glutamicum*

A. Krüger (2023), IV, 274 pp

ISBN: 978-3-95806-686-1

Band / Volume 267

Morphological and functional characterization of layer 5 neurons in rat medial prefrontal cortex, their synaptic microcircuitry and serotonin modulation

R. Rama (2023), 116 pp

ISBN: 978-3-95806-688-5

Band / Volume 268

Magnetic and transport studies of the parent and Fe doped Hexagonal-Mn₃Ge Weyl semimetal

V. Rai (2023), xviii, 156 pp

ISBN: 978-3-95806-695-3

Weitere **Schriften des Verlags im Forschungszentrum Jülich** unter
<http://wwwzb1.fz-juelich.de/verlagextern1/index.asp>

Schlüsseltechnologien / Key Technologies
Band / Volume 268
ISBN 978-3-95806-695-3